The Room Temperature CH-DTL and its application for the FAIR Proton Injector

Dissertation
zur Erlangung des Doktorgrades
der Naturwissenschaften

vorgelegt beim Fachbereich Physik
der Johann Goethe Universität
in Frankfurt am Main von

Gianluigi Clemente
geboren in Benevento, Italien

Frankfurt am Main, 2007

Von Fachbereich Physik der
Johannes Goethe Universität als Dissertationen angennonen

Dekan:	Dr. Prof. Wolf Aßmus
Erster Gutachter:	Dr. Prof. Ulrich Ratzinger
Zweiter Gutachter:	Dr.Prof. Alwin Schemmp
Datum der Disputation:	2007

LA PRATICA VAL PIU' DELLA GRAMMATICA!
Proverbio popolare italiano
DIE PRAXIS WIEGT MEHR ALS DIE GRAMMATIK,
Volkstümliches italienisches Sprichwort

Zusammenfassung

Bei der Gesellschaft für Schwerionenforschung (GSI) wird momentan der Aufbau eines neuen, internationalen Zentrums für die Forschung mit Antiprotonen- und Schwerionenstrahlen (FAIR) vorbereitet. Die Beschleunigeranlage von FAIR basiert auf zwei supraleitenden Synchrotrons, welche mehrere Speicherringe und Experimentaufbauten mit hochenergetischen Strahlen bei bisher unerreichten Intensitäten versorgen werden. Wesentlich dabei ist, dass bei FAIR mehrere Experimente mit unterschiedlichen Anforderungen hinsichtlich Ionen-Sorte und Strahleigenschaften parallel versorgt werden können, d.h. de facto simultan durchgefhrt werden können.

Die Primärintensitäten fr das Schwerionenprogramm von FAIR sollen vom gegenwärtig schon betriebenen Beschleunigerkomplex (UNILAC, SIS18) geliefert werden. Fr die für die Antiprotonenerzeugung erforderlichen primären Protonenstrme hingegen ist dies nicht möglich. Es muss ein für den Hochstrombetrieb ausgelegter, neuer Protoneninjektor konzipiert und aufgebaut werden.

Bei der konzeptionellen Auslegung eines Linac kommt der effizienten Beschleunigung herausragende Bedeutung zu. Diese bestimmt über die Länge des Linacs als auch über die Kosten der Energie-Versorgung wesentlich die Anschaffungs- und die Betriebskosten. Im Rahmen des JPARC Projektes wurden gepulste 3 MW-Klystren sowie die entsprechende niederleistungs-HF-Anlage bei 325 MHz entwickelt. Auf die ausgereiften Technologien wird bei der Auslegung des FAIR Protonenlinacs zurückgegriffen. Die vorliegende Arbeit beschreibt die einzelnen Schritte der Auslegung des Driftröhrenbeschleunigers des FAIR Protonenlinacs. Der Driftröhrenbeschleuniger (engl. Drift Tube Linac DTL) basiert auf der Verwendung neuartiger Crossbar (CH) Strukturen zur Strahlbeschleunigung. Diese bisher noch nicht gebauten Strukturen versprechen signifikant hhere Beschleunigungseffizienzen als herkömmliche Strukturen.

Nach einem kurzen Abriss der Entwicklung der Protonenbeschleunigung der vergangenen Jahre werden im ersten Kapitel die wesentlichen Parameter einer RF-Strukturen vorgestellt. Ebenso wird auf die Strahldynamik in einem Linaerbeschleuniger eingegangen. Im Speziellen werden die Bedingungen stabile longitudinale und transversale Strahlfokussierung behandelt. Abschlieend folgt eine Beschreibung moderner Protonenlinacs an anderen Forschungszentren wie z.b.

- The SNS at Oak Ridge, USA;
- The CERN LINAC4 at Cern, Switzerland;
- The JPARC in Japan;
- FAIR at Darmstadt, Germany.

Die Konzepte werden verglichen bzw. kommentiert.

Das zweite Kapitel beschreibt die Auslegung des CH-DTL. Zu Beginn werden das Prinzip einer H-Moden-Struktur sowie der aktuelle Stand der Entwicklung solcher Strukturen erläutert. Dabei wird konkret auf die kürzlich aufgebaute IH-Struktur für das Heidelberger Schwerionen-Therapie-Zentrum eingegangen. Bei dieser Struktur konnte eine hervorragende Übereinstimmung der simulierten RF-Eigenschaften mit den Messwerten gefunden werden. Im Folgenden wird dargelegt, dass die CH-Struktur die logische Erweiterung des IH-Konzeptes hin zu Frequenzen oberhalb von 250 MHz, entsprechend Protonenenergien von 3 bis 150 MeV, darstellt. Ferner wird gezeigt, dass CH-Strukturen deutlich höhere Beschleunigungs-Effizienzen aufweisen als herkömmliche Stukturen aufweisen. Diese Eigenschaft empfiehlt die CH-Struktur nicht nur für FAIR, sondern auch fr andere Protonen-Injektoren. Neben dem FAIR-Linac wird, zur Zeit, auch der Linac des Protonen-Booster-Komplexes am FermiLab auf CH-Strukturen basierend ausgelegt. Der mechanisch stabile Aufbau der CH-Struktur macht auch Dauerstrich- bzw. supraleitende Anwendungen möglich. Somit wird diese neue Struktur zu einer Alternative zu klassischen Alvarez-Strukturen bei Projekten, auch die supraleitenden Betrieb schon bei niedrigen relativen Geschwindigkeiten v/c erfordern, wie IFMIF und EUROTRANS.

Die Ergebnisse theoretischer Untersuchungen der RF-Eigenschaften von CH- Strukturen sind sehr vielversprechend, jedoch fehlen experimentelle Erfahrungen bei der Konstruktion eines solchen Resonators. Daher wurde am IAP zunächst ein acht-zelliges Modell mit Periodenlänge $\beta\lambda/2$ 45 mm ausgelegt und aufgebaut. Die einzelnen Schritte der Konstruktion, Herstellung und Verkupferung sollten erstmalig erprobt, sowie die fertige Struktur im Hinblick auf mechanische Stabilität und insbesondere bzgl. der Kühleigenschaften untersucht werden. Der Aufbau jeder Komponente und die Schritte der Fertigung der Struktur wurden protokolliert. Besonderes Gewicht wurde dabei auf das Vorgehen zur Feinabstimmung der RF-Eigenschaften gelegt, welches stark IH-Strukturen abweicht.

So werden z.B. bei IH-Strukturen an den Girdern Holmen angebracht: sind diese ausreichend lang wird die kurzschließende Wirkung der Enddeckel bzgl. der H-Mode unterdrückt. In CH-Strukturen hingegen können keine Holme integriert werden und es müssen andere Methoden zur Absenkung der Frequenz im Endbereich des Resonators angewendet werden. Eine einfache Möglichkeit besteht in der Verlängerung der Halbdriftröhren an den Enden des Resonators, welche das Volumen der Endzellen erhöht. Ferner kann der Radius dieser Endzellen vergrößert werden: Durch diese Verringerung des Abstandes zum nächsten Stem wird die Kapazität der Endzelle erhöht. Durch beide Maßnahmen können die Halbdriftröhren hinreichend groß dimensioniert werden, um magnetische Linsen zur transversalen Strahlfokussierung aufzunehmen. Somit kann eine sehr kompakte DTL-Sektion realisiert werden. Der verringerte Abstand aufeinanderfolgender RF-Strukturen verbessert zudem die longitudinale Strahlfokussierung, was besonders bei hohen Strahlströmen relevant ist.

Zur lokalen HF-Feinabstimmung der Struktur sollte zunächst das Verfahren mit Presspassungen in den Driftröhren angewendet werden: Dabei werden zwei mit flüssigem Stickstoff gekühlte Halbdriftröhren aus massivem Kupfer in den betreffenden Stem eingebracht. Die anschließende Thermalisierung sorgt für einen hinreichend guten elektrischen Kontakt zwischen Driftröhre und Stem. Trotz guter Ergebnisse mit dem Simulationsprogramm ANSYS zeigte sich bei der Herstellung des Modells, dass das Einschweißen der Stems in den Resonatormantel eine solche Deformation des Stems am

Ort der Driftröhre bewirkt, dass kein hinreichender HF-Kontakt mehr besteht. Diese Presspassungen werden daher verworfen. Stattdessen sollen nun die Driftröhren direkt in den Stem eingeschweißt werden. Das entsprechende Endstück des Stem ist hinreichend dick auszuführen, so dass Deformationen hinreichend unterdrückt werden. Zum Test der Kühlung wurde die fertige Struktur mit einer Dauerstrich-HF-Quelle betrieben. Zunächst wurde die Leistung auf 1 kW begrenzt, entsprechend einer Gesamtspannung von 220 kV entlang der Struktur. Diese Spannung konnte innerhalb von nur 20 Minuten ohne signifikantes Auftreten von Multipacting erreicht werden. Die Temperatur des äußeren Zylinders blieb sehr stabil. Abschließend wurde die Eingangsleistung auf 2 kW verdoppelt (304 kV Gesamtspannung) ohne dass ein weiteres RF-Konditionieren erforderlich war. Die beobachtete Stabilität der Resonanzfrequenz bestätigte die Effizienz des Kühlsystems.

Die mit diesem Model gemachten Erfahrungen wurden genutzt, um in einem zweiten Schritt eine Prototyp-Struktur fr den FAIR Protonenlinac zu entwickeln, welcher dann am Linac im Strahlbetrieb eingesetzt werden soll. Die Verfgbarkeit von Klystrons mit bis zu 3 MW RF-Leistung lste die Entwicklung HF-gekoppelter CH-Strukturen aus, um das Potential dieser Klystren bei Vermeidung von Magic-Tees nutzen zu können.

Das Konzept zur Kopplung zweier CH-Strukturen knüpft an die Variation der Länge der Halbdriftröhren am Resonatorende zur RF-Feinabstimmung an. Diese Halbdriftröhren werden gänzlich von magnetischen Feldlinien umschlossen, analog zum E_{010}-Mode. Fügt man nun zwei benachbarte CH-Strukturen zusammen, wobei der gemeinsame Endboden zusätzlich durch einen Stem ersetzt wird, vereinen sich die beiden Halbdriftröhren zu einer zentralen, verlängerten Driftröhre des neuen Resonators. Diese zentrale Driftröhre wird nun wie bei einer klassischen Alvarez-Struktur im E_{010}-Mode schwingen. Die Abstimmung der Resonanzfrequenz erfolgt über die Wahl des Radius dieser Driftröhre.

Man erhält so eine kompakte Struktur bestehend aus zwei H_{211}-Resonatoren, die über eine Zwischentank-Sektion im E_{010}-Mode magnetisch gekoppelt sind. Nutzt man die Zwischentank-Sektion zur magnetischen Einkopplung, so wird das die zentrale Driftröhre umschließende magnetische Feld die jeweils angrenzenden CH-Resonatoren im TE Mode anregen.

Die Güte dieser Kopplung wurde zunächst mit der 3D HF-Software Microwave Studio geprüft. Dabei wurde die Kopplung zweier identischer CH-Modelle angenommen, die jeweils dem zuvor am IAP gebauten Modell entsprachen. Zur phasengerechten Beschleunigung muss der Abstand der beiden äußeren Beschleunigungsspalte ein gerades Vielfaches von $\beta\lambda$ betragen; im vorliegenden Fall wurde n=5 gewählt. Die Relevanz des Radius der zentralen Driftröhre wurde untersucht. Mehrere Beispiele dazu werden präsentiert, und abschließend erfolgt eine Illustration der Effekte von Fertigungstoleranzen bzw. -fehlern.

Motiviert durch die guten Ergebnisse dieser Simulationen wurde entschieden, dieses innovative Konzept zur Grundlage der Auslegung des Protonenlinac und somit der ersten Prototyp-Struktur zu machen. Vor dem Bau des Prototyps sollte zunächst die vorgeschlagene RF-Kopplung mit einem weiteren Modell experimentell überprft werden. Das Modell ist eine Abbildung im Maßstab 2:1 der dritten und vierten CH-Struktur des FAIR Protonenlinacs, entsprechend dem Energiebereich von 11.7 bis 24 MeV. Die ersten beiden Strukturen wurden bewusst nicht gewählt, da die Auslegung der vorangehenden RFQ-Struktur noch nicht abgeschlossen ist. Das Programm LORASR diente

zur Bestimmung der wesentlichen Parameter der Struktur bzw. des Modells, d.h. der Anzahl der Beschleunigungsspalte, der Spaltspannungen, der Drifttröhrenlängen und des Transit-Time-Faktors. Mit Microwave Studio erfolgte die Optimierung der Geometrie zur Abstimmung der RF-Eigenschaften.

Die drei Meter lange Strukture hat insgesamt 29 Beschleunigungsspalte, 13 im ersten bzw. 14 im zweiten CH-Resonator. Die berechnete Shunt-Impedanz von 60 $M\Omega/m$ passt gut zu den vorhergehenden Rechnungen ohne Tank-Kopplung. Der nächste parasitäre Mode bei 326.5 MHz liegt 1.3 MHz oberhalb der Betriebsfrequenz. Dieser Abstand ist hinreichend groß im Vergleich zur Bandbreite des Klystrons von 0.75 MHz. Ferner stellt dieser Mode eine schwache Anregung der Koppelzelle dar. Da die Einkopplung naturgemäß direkt in die Koppelzelle erfolgt, ist von einem sehr schwachen Überlapp der beiden Moden auszugehen.

Das letzte Kapitel widmet sich der Auslegung der Strahlfokussierung in der DTL-Sektion des FAIR Protonenlinacs. Zu Beginn wird die Wahl der wesentlichen DTL-Parameter wie Frequenz, Strahlstrom, Energiebereich und Eingangsemittanz motiviert.

Der Protonenstrahl mit einem Strom von 100 mA wird in einer EZR-Quelle erzeugt und mit einer Energie von 95 keV extrahiert. Die anschließende Niederenergie-Strahlführung (LEBT) basierend auf zwei Solenoid-Magneten separiert die Protonen von anderen Ionen wie H_3^+ und H_2^+. Der Anteil der Protonen am Gesamtstrom betrgt mindestens 70 mA. Die LEBT endet mit dem Einschuss in die RFQ-Struktur, in welcher der Strahl longitudinal gebündelt (gebuncht) und simultan auf 3 MeV beschleunigt wird. Nach der RFQ-Struktur wird der Strahl in den CH-DTL injiziert.

Momentan werden zwei Auslegungen für die RFQ-Struktur entwickelt. Ein Typ basierend auf dem 4-rod-Prinzip wird derzeit am IAP untersucht; ein weiterer Typ ausgehend vom 4-vane-Aufbau wird durch ITEP/Moskau vorgeschlagen. Im relevanten Frequenzbereich wurden bisher 4-vane RFQs verwendet. Diese sind im Vergleich zu 4-rod Typen jedoch erheblich teurer. Ein 4-rod Typ ist einfacher im Aufbau wurde aber bisher nur bei Frequenzen unterhalb von 250 MHz eingesetzt. Erfahrungen oberhalb von 300 MHz liegen daher noch nicht vor. Deshalb wurde am IAP ein Modell aufgebaut, und die Tauglichkeit einer 4-rod RFQ für den FAIR Protonenlinac konnte demonstriert werden. Die Strahldynamische Auslegung des DTL basiert auf Strahleigenschaften, wie sie am Ausgang einer 4-rod-RFQ-Struktur simuliert wurden.

Im Anschluss an die RFQ-Struktur wird der Strahl in der MEBT (Medium Energy Beam Transport) Sektion für den Einschuss in die DTL-Sektion angepasst. Die MEBT besteht aus einer einzelnen Quadrupollinse, einer Buncher-Struktur sowie einem Quadrupoltriplett.

Die DTL-Sektion umfasst zwölf CH-Strukturen, die zu sechs Paaren von je zwei HF-gekoppelten Strukturen zusammengefasst sind. Nach Beschleunigung in drei solcher Paare, d.h. bei einer Strahlenergie von 35 MeV, ist eine etwa 60 cm lange Diagnose-Sektion integriert, um Strahlemittanzen zu messen und ggf. Haloteilchen aus dem Strahl zu entfernen. Nach vollständiger Beschleunigung auf 70 MeV wird der Strahl in den Transferkanal, der heute zur Injektion des UNILAC-Strahls in das SIS18 dient, eingelenkt. Kurz vor Injektion in das SIS18 wird in einer Re-Buncher-Struktur die Energie-Unschrfe des Strahls unter den vom Synchrotron geforderten Wert von $\pm 0.1‰$ gebracht.

Für die Vielteilchensimulationen zur Auslegung der Strahlfokussierung wurde die errechnete Teilchenverteilung am RFQ-Ausgang vollständig übernommen, d.h. es wurden keine rms-äquivalenten, vereinfachten Verteilungen, wie z.B. Gauss- oder K-V-Typen,

benutzt. Die Ergebnisse dieser Simulationen bestätigten, dass ein CH-DTL mit longitudinaler KONUS-Fokussierung Protonenstrahlen verlustfrei und mit hoher Effizienz beschleunigen kann. Insbesondere das moderate Anwachsen der Strahlemittanzen auch bei Verwendung realistischer Eingangsverteilungen zeigt, dass CH-DTL's für Protonen bis 100 MeV Endenergie eingesetzt werden können.

Der abschlieende Teil der Arbeit befasst sich mit Untersuchungen zu Strahlverlusten bei Annahme realistischer Toleranzen bzgl. der HF-Felder und Justierungen strahlfhrender Komponenten. Simulationen mit unterschiedlicher Teilchenzahl dienten zur Bestimmung der erforderlichen Statistik. In diesem Zusammenhang wird die Methode des "Teilchenbrtens" zur knstlichen Vervielfachung der Teilchenzahl gegebener Verteilungen beschrieben. Sie kam zur Anwendung bei der Generierung einer 100000 Teilchen umfassenden Verteilung aus der lediglich 5000 Teilchen umfassenden Verteilung einer RFQ-Simulation mit dem PARMTEQ-Programm. Die oben genannten Toleranzen wurden durch bewusst integrierte Fehler in folgenden Klassen von Eingangsgrößen modelliert:

- Position Δx, Δy der einzelnen magnetischen Quadrupolachsen relativ zur Soll-Strahlachse. Rms-Wert des Fehlers 0.05, 0.1 und 0.2 mm.
- Spannungsamplitude in den einzelnen Beschleunigungsspalten einer Struktur. Rms-Wert des relativen Fehlers 1
- Summe der Spannungsamplituden aller Spalte einer Struktur. Rms-Wert des relativen Fehlers $\pm 1\%$.
- Phase der HF-Felder einer Struktur. Rms-Wert des Fehlers $\pm 1^\circ$.

In ersten Analysen der Strahlverluste wurde jeweils nur eine Klasse von Eingangsgren mit statistischen Fehlern mit o.g. rms-Breiten belegt. Im späteren Verlauf wurden alle Eingangsgrößen mit Fehlern behaftet. Dabei zeigte sich, dass auftretende Verluste durch die Fehljustierungen der Quadrupole dominiert werden und dass die Verluste vor allem in der Diagnose-Sektion in der Mitte des DTL auftreten. Fehler bei den anderen Eingangsgrößen spielen innerhalb der gewählten Bandbreite praktisch keine Rolle für das Strahlverlust-Szenario. Liegen die Justierfehler der Quadrupole unterhalb von ± 0.1 mm, sind Strahlverluste von weniger als 10 % zu erwarten. In Anbetracht der vorliegenden Erfahrung mit der Justage interner und externer Linsen bei existierenden IH-Strukturen erscheint die o.g. Toleranzgrenze beherrschbar.

Contents

Chapter 1

Introduction: RF Linacs And The New Generation of Proton Injectors

Despite the enormous progress performed in the XX century, particles and nuclear physics present still many questions to be answered: just as examples, the standard model foresees the existence of a particle, the Higg's boson, never observed so far, while most of the matter present in the universe is still of unknown nature. A fundamental role in solving those challenging puzzles is played by the new technologies offered by accelerator physics.

The physical and technological progresses in particle acceleration can in fact provide scientists with the highest energies ever available together with beams of qualities and intensities never reached so far. On one side, the Large Hadron Collider (LHC) at CERN represents the most powerful synchrotron and storage ring ever built, on the other hand linacs promise to make available extremely high intensity beams which makes those machines attractive both as standing alone devices as well as for injectors into higher energy rings. This justifies the intensive R&D activities which have been performed all around the world in the last years resulting in new facilities based on high intensity proton linacs. This is the case, for instance, of FAIR, the facility for antiprotons and ions research under development at GSI which requires a new dedicated proton injector for the $\bar{p}$ physics program.

This thesis describes the research activity performed on such a proton injector based on a completely new structure, the CH-DTL, never built so far and showing a significant higher potential for ion acceleration when compared with conventional RF Structures.

In this introductory chapter, after an historycal overview on the proton accelerators, the main parameters of the RF cavities are illustrated together with a description of beam dynamics in linear accelerators.

Afterwards, the most recent projects based on a high intensity proton injector are described, compared and commented with particular attention put on the FAIR facility.

The thesis continues with a detailed description of the state of the art of H mode linacs to focuse then on the R&D performed on the CH-DTL. Finally, the FAIR Proton injector is described throughout all the design steps, both in terms of beam dynamics as well as in terms of structure development and engineering design.

1.1 A Brief History of Proton Acceleration

The concept to use a particle beam to investigate the structure of matter was developed for the first time at the end of the XIX century when discharge tubes were employed by Lenard to perform electron scattering on gases, and by Franck and Hertz to produce excited atomic electron shells by electron bombardment; the first use of an ion beam was performed by Rutherford in his famous scattering experiments where a beam of α particles was employed to study the size of the atom. Following the line of research based on the use of natural α particles, Rutherford performed in 1919 the first nuclear reaction.

The progression from atomic to nuclear physics required higher energies and intensities than those provided by natural radioactive sources, but the availabe electrostatic devices were far away from reaching the necessary voltage and, for a few years, no advance was performed. Suddenly, in 1928 Gamow and Gurney predicted the tunnel effect [1] and it appeared that an energy of 500 keV might be sufficient to split the atom. This pushed Cockroft and Walton to develop a 600 kV proton accelerator [2]. Figure 1.1 shows the original apparatus: the top electrode contains the proton source and was held at 400 kV, the intermediate drift tube at 200 kV and final drift tube and target at earth potential. The voltage generator was able to generate a maximum DC voltage of 700 kV above which discharge occurred. The Cockcroft Walton generator, as it became known, was widely used for many years after as the input stage (up to 800 kV) for larger accelerators, since it could deliver a high current.

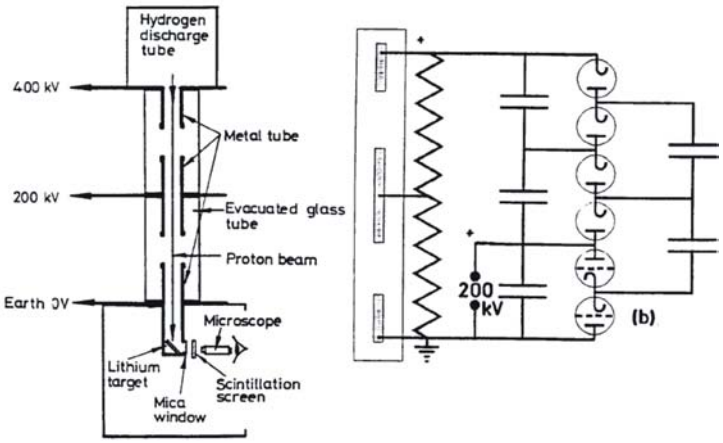

Figure 1.1: On the left the Cockcroft and Walton's first proton accelerator and, on the right, the DC generator used to creat the high voltage on the charged electrodes.

At about the same time Van de Graaff invented an electrostatic generator for nuclear physics research and he built his first machine in Princeton, which reached a potential of 1.5 MV [3]; the principle of this type of generator is shown in Fig.1.2.

In later versions the Van de Graaff generator was modified in order to reach higher potential: firstly, the sparking threshold was raised by putting the electrode system and accelerating tube in a high-pressure tank containing dry nitrogen, or Freon, at 9-10 atmospheres, which enables operation typically up to 10 MV. The second was a later development, which has the special name of Tandem accelerator (see Fig.1.3).

The new feature of the Tandem accelerator was to use the accelerating voltage twice

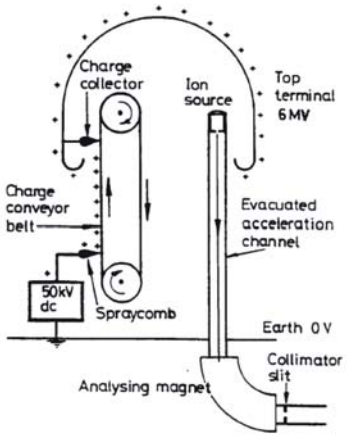

Figure 1.2: Van der Graff electrostatic generator.

over. First an extra electron is attached to the neutral atoms to create a negative ion beam. This negative ion beam is then injected into the Tandem at earth potential and accelerated up to the high-voltage terminal where it passes through a thin foil. This foil strips at least two electrons from each negative ions converting them to positive ones. The positive ion beam is finally accelerated a second time back to earth potential.

The Van de Graaff generator and the Tandem provide beams of stable energy and small momentum spread, but they are unable to provide as high currents as the Cockcroft-Walton generator: the highest energy Tandem is at Oak Ridge National Laboratory and routinely operates with 24.5 MV on the central terminal.

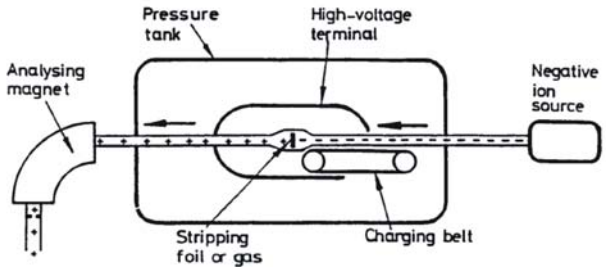

Figure 1.3: The Tandem accelerator based on a two stage acceleration.

The DC accelerators were limited to the maximum voltage that could be generated in the system: this limitation was too restrictive for the requirements of high-energy physics and an alternative was needed. The alternative had already been proposed in 1924 in Sweden by Ising [4] who planned to repeatedly apply the same voltage to the particles using alternating fields.

Ising suggested to accelerate particles with a linear series of conducting drift tubes: alternate drift tubes are connected to the same terminal of an RF generator whose frequency is adjusted so that a particle traversing a gap sees an electric field in the direction of its motion and, while the particle is inside the drift tube, the field reverses so that it is again in the direction of motion at the next gap. As the particle gains energy and speed the structure periods must be made longer to maintain synchronism. In 1928 Wideröe built a 'proof-of-principle' linear accelerator [5] made by a single drift

tube at 25 kV resonating at 1 MHz, which provided a 50 KeV Potassium beam. This was also the first accelerator which had ground potential at both the entrance and exit ends, but was still able to deliver a net energy gain to the beam: thus, differently from electrostatic devices, the voltage gain of an RF accelerator could exceed the maximum applied voltage.

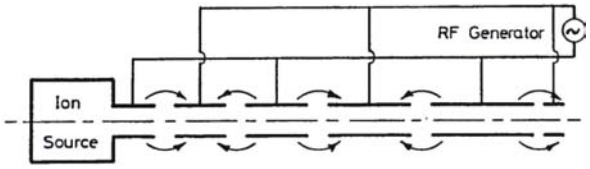

Figure 1.4: The Ising design of the first RF Linac.

Unfortunately, if on one side there was no doubt that by increasing the number of drift tubes one could reach unlimited higher energies, on the other hand it was also clear that the method could not be applied to protons and light ions whose application in nuclear physics was higly demanded: for those particles, as the velocity increases, the drift tubes become inconveniently long unless the frequency can be increased at least up to the MHz range, which was far away from the technical capabilities of that time. For this reason linacs development was pushed into the background by a simpler idea conceived by Ernest Lawrence in 1929 [6], the fixed-frequency cyclotron (see Fig.1.5). In 1931 Livingston demonstrated the principle of cyclotron by accelerating hydrogen ions to 80 keV and, a year later, Lawrence built his first cyclotron. It was less than 28 cm in diameter and could accelerate protons to 1.25 MeV. In 1939 the University of California built a 1.5 meter diameter cyclotron delivering 20 MeV protons, twice the energy of the most energetic alpha particles emitted from radioactive sources. The cyclotron, however, presented two main limitations: it was limited in energy by relativistic effects and the stability of the beam during the acceleration was extremely weak.

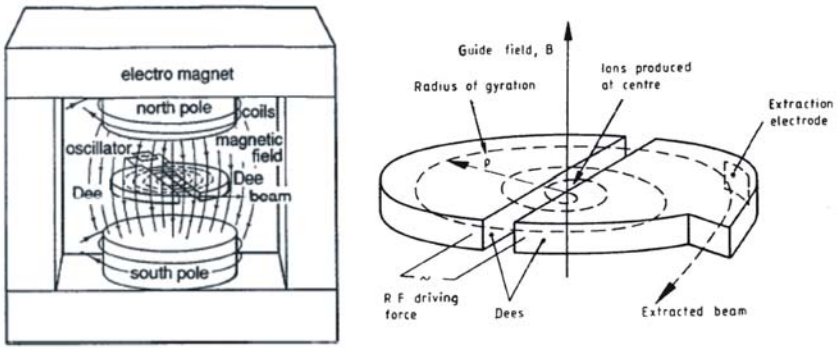

Figure 1.5: The concept design of the cyclotron.

In the early cyclotrons, for example, the field was made as uniform as possible only to find that the beam was unstable. The magnets were modified for each small step in energy to keep the beam stable, thus ending up with a field shape for transverse stability that decreased with radius. Theory has later shown that this decrease should be an inverse power law of the radius between zero and unity.

The relativistic effects, which cause the particles to slow down and loose synchronism with the RF field couldn't be solved only by reducing the frequency, as proposed in the synchro-cyclotron, since the spread in revolution frequency with energy would quickly exploit the natural energy spread in the beam and disperse the particles away from the peak of the RF voltage: in this case a longitudinal focusing mechanism is needed.

This problem was overcome by E. McMillan [7] and independently by V. Veksler [8] who discovered the principle of phase stability in 1944 and invented the synchrotron. Phase stability is general to all RF accelerators except the fixed-frequency cyclotron. The effect is that a bunch of particles, with an energy spread, can be kept bunched throughout the acceleration cycle by simply injecting them at a suitable phase of the RF cycle. This focusing effect was strong enough that the frequency modulation in the synchro-cyclotron was simply sinusoidal. Synchro-cyclotrons can accelerate protons to about 1 GeV, a great improvement on the simple cyclotron, but they accelerate in pulsed mode at low duty factor, which reduces drastically the availabe intensity of the beam.

The highest intensity reached so far belongs to the 590 MeV PSI II (Switzerland) which delivers up to 3 mA proton beam. Cyclotrons are easy to built, compact and require a simplified RF equipment compared to linacs and synchrotons: for those reasons they found many applications as industrial devices, especially in the production of radioisotopes and in the field of hadrotherapy. Unfortunately, still nowadays injection and extraction of the beam remain problematic resulting in a bad quality of the beam which represents the major constraints of such a device.

In the synchrotron [9], the guide magnetic field increases with particle energy to keep the orbit stationary and the acceleration is applied by an RF voltage via a gap or a cavity. In 1946 F. Goward and D. Barnes [10] were the first to make a synchrotron work, and already in 1952 a 3 GeV synchroton was built at Brookhaven National Laboratory in USA.

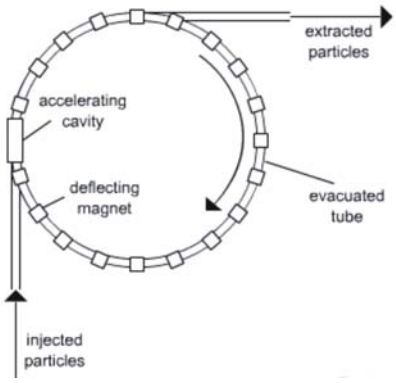

Figure 1.6: The concept design of the synchrotron: the particles follow a circular path guided by an array of bending magnets and the dedicated cavity are used to accelerate the beam. To keep the particles on the same trajectoty in each run the megnetic field has to be modulated according to their speed.

After the development in the same year of strong alternative focusing (AGF), the syncrotron has become the standard structure for high energy physics: moreover, the development of the proton-antiproton storage rings collider has allowed to reach energies in the center of mass up to 2 TeV at Fermilab and 62 GeV at CERN. The largest storage

ring of ever, the LHC at CERN, is at present under construction at CERN and will deliver a 14 TeV in the center of mass proton-antiproton beam.

The CERN proton-antiproton storage ring was also the source of a Nobel Prize for C. Rubbia and S. van der Meer in 1984, following the discovery of the W and Z particles. It is importanto to remark that the proton-antiproton colliders were only made possible by the invention of stochastic cooling by S. van der Meer for the accumulation of the antiprotons [11].

As mentioned, linear accelerators were eclipsed during the thirties by circular machines. However, the advances in ultra-high frequency technology during World War II (radar) opened up new possibilities and renewed interest in linac structures. L. Alvarez proposed to enclose the linear array of drift tubes inside a high-Q value cylindrical structure exited in the transverse magnetic mode [12]: in this way a uniform electric field would be present in the gaps while the particle would be shielded inside the drift tubes when the field was reversed. At Berkeley the first RF proton linear accelerator was built 1946 delivering a 32 MeV proton beam [13].

The Alvarez accelerator has become very popular as an injector for large proton and heavy-ion synchrotrons all over the world with energies in the range of 500-600 MeV, that is essentially non-relativistic particles. The largest fully operational proton linear accelerator to date is the 800 MeV 'pion factory' (LANSCE) at Los Alamos.

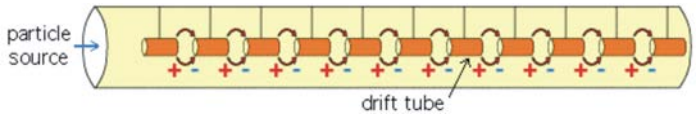

Figure 1.7: The RF linac as developed by L.Alvarez.

Finally, the last structure developed for proton is the radio-frequency quadrupole (RFQ) suggested in 1970 by I. Kapchinski and V. Telyakov [14]. The RFQ uses a transversal electric field with a longitudinal component to accelerate and focuse in the same RF field. The structure can be used up to 5 MeV and has rapidly replaced the Cockcroft-Walton generator.

Nowadays the interest in proton linac is grown up: these machines can in fact provide beam of higher energy with reduced momentum spread and size when compared to circular accelerators. Moreover linacs presents other advantages:

- Strong focusing can be easily provided to confine high intensity beams;
- Due to the linear path, repetive error conditions causing destructive beam resonances are avoided;
- Injection and extraction are extremely easy and no special technique is requested;
- Linacs can be operated at any duty factor resulting in a high average current.

In the next section, after a short introduction to the beam dynamics and to the main RF parameters of linear accelerators, some of the most recent facilities based on a high intensity proton linac are described, commented and compared.

1.2 General Parameters of RF Linacs

RF linacs used for proton and ion acceleration consist in a series of drift tubes and gaps enclosed in a resonating cavity.[1] The edges of each couple of adiacent drift tubes are at different potential so that a longitudinal electric field E is generated. On axis the value of the field can be expessed as

$$E_z = E(0,z)cos[\omega t(z) + \phi] \tag{1.1}$$

where $t(z) = \int_0^z dz/v$ is the time when a particle with velocity v is at the posizion z.

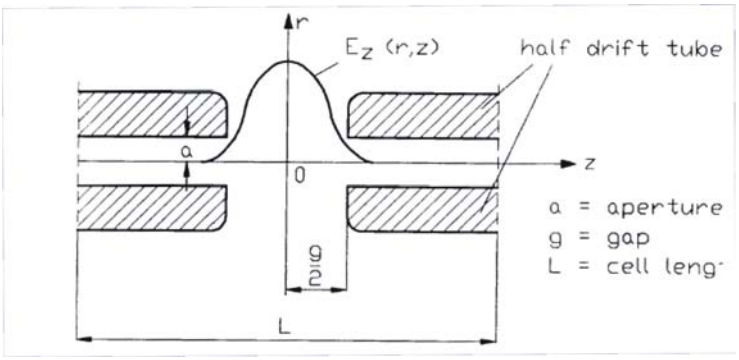

Figure 1.8: The accelerating gap.

Assuming that for $t = 0$ the particle is at the gap center then ϕ is simply the phase of the particle with respect to the field crest. Crossing the gap the particle gain a quantity of energy

$$\Delta W = q \int_{-l/2}^{l/2} E(0,z)cos[\omega t(z) + \phi]dz \tag{1.2}$$

which is normally reported in literature as

$$\Delta W = qV_0 T cos(\phi) \tag{1.3}$$

where $V_0 = \int_{-l/2}^{l/2} E(0,z)dz$ is the RF axial voltage and T is the *Transit Time Factor* .

The transit time represents then the reduction in energy gain caused by the sinusoidal variation of the electric field with respect to a DC voltage of amplitude V_0: typically it is an encreasing function of the particle energy ranging from 0.7 to 0.9.

Multicells cavisties consist in a series of accelating gaps which can oscillate in phase, like in the classical Alvarez structure (2π mode or $\beta\lambda$ structure), or in opposite phase like in H-mode cavities (π mode or $\beta\lambda/2$ structure).

The quality of the resonator which includes the drift tubes is determinated by the bandwidth of the resonance occuring at the resonance frequency: this amplitude is measured at -3dB from the maximum value defining the Q-value as

$$Q = \frac{f_0}{\Delta f}\,(-3dB). \tag{1.4}$$

[1] this definition doesn't apply to RFQ.

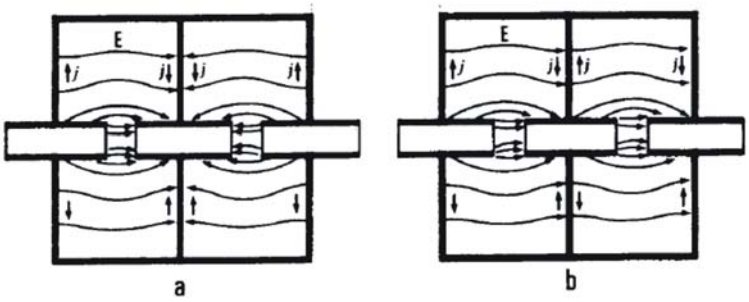

Figure 1.9: Adjacent single-gap cavities: a) π mode or $\beta\lambda/2$ structures, b) 2π mode or $\beta\lambda$ structure.

This parameter can be expressed as well as the ratio between the stored and the dissipated energy at the resonance frequency, i.e.

$$Q = \frac{\omega W}{P} \tag{1.5}$$

where W is the stored energy and P is the dissipated RF power.

This definition refers to the $Unloaded\,Q - value$, Q_0, since it doesn't include the power which is reflected back to the generator. For this reason one defines a $Loaded\,Q - value$, Q_l, as

$$\frac{1}{Q_l} = \frac{1}{Q_0} + \frac{1}{Q_{ext}} \tag{1.6}$$

$$Q_{ext} = \frac{\omega W}{P_g} \tag{1.7}$$

where Q_{ext} is the extrenal Q-value and P_g is the power flowing back to the generator.

While the unloaded Q-value is an intrinsic parameter of the cavity ,the loaded Q-value depends from the coupling between the cavity and the power supply. For this reason it is necessary to have a weak coupling to measure the Q_0 value. One has to mention that, if the power needed to feed the beam and the outcoupling pick-up is considered, the corresponding additional terms have to be added to Eq.1.6.

Besides the Q-value, the main parameter of a room temperature structure is the *Shunt Impedance per unit length*, a figure of merit that is independent from the excitation level of the cavity and measures the capability of producing an axial voltage for a given dissipation power. It is expressed in MΩ/m as

$$Z = \frac{\left(\int_0^l |E(0,z)|dz\right)^2}{P \cdot l} \tag{1.8}$$

where l is the length of the cavity.

In reality, what is important in the design of an accelerating cavity is to maximize the energy gain for a given loss power: for this reason the efficiency of a linac is measured by the *Effective Shunt Impedance per unit length*, which relates the shunt impedance to the Transit Time Factor T according to

$$Z_{eff} = ZT^2 \cdot cos^2(\bar{\phi}). \tag{1.9}$$

where $\bar{\phi}$ is the averaged accelerating RF phase inside the cavity.

Another useful parameter is the r/Q ratio, which measures the capability to concentrate the electric field in the acceleration region,

$$\frac{r}{Q} = \frac{(\int_0^l |E(0,z)|dz \cdot T)^2}{\omega W}. \tag{1.10}$$

This parameter depends only from the cavity geometry and is indipendent from the losses due to the ohmic dissipation.

The operating frequency is together with the energy range the most important parameter of every accelerator: for this reason it is important to show the dependency of the RF parameters on the operating frequency. It is not difficult to demonstrate that for a non superconducting structure we have the following relations:

$$P \propto f^{-\frac{1}{2}} \tag{1.11}$$

$$Q_0 \propto f^{-\frac{1}{2}} \tag{1.12}$$

$$ZT^2 \propto f^{\frac{1}{2}} \tag{1.13}$$

$$\frac{ZT^2}{Q} \propto f \tag{1.14}$$

1.3 Beam Dynamics in Linear Accelerators

1.3.1 Longitudinal Stability

The design of linear accelerators is commonly based on the concept of *sinchronous particle*, a particle which has always the desired phase with respect to the electric field along the drift tubes structure. The beam motion occurs through a series of gap and drift tubes as shown in Fig.1.10. It is assumed that passing from gap n-1 to gap n the particles velocity β_{n-1} remains constant, or equivalently, the energy gain through a single gap is small compared to the particle energy.

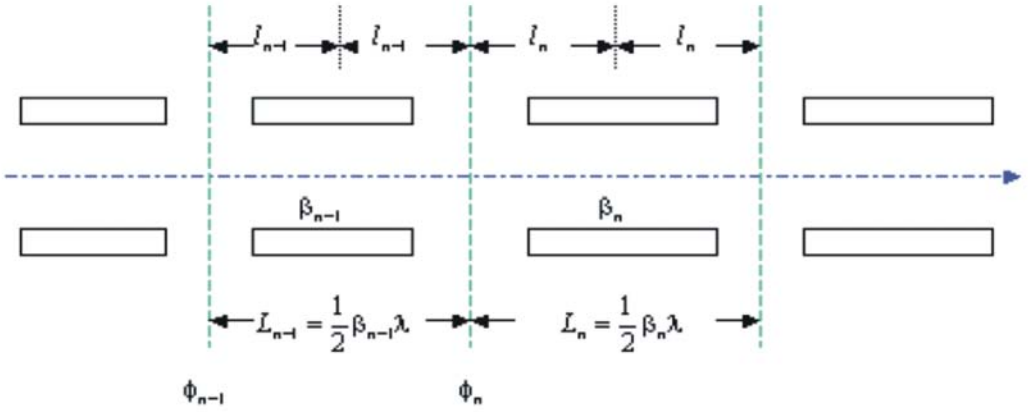

Figure 1.10: A series of accelerating gaps to describe the longitudinal motion.

In a $\beta\lambda/2$ structure the relation between the RF phase from gap n-1 to gap n can be approximately expressed as

$$\phi_n = \phi_{n-1} + \omega\frac{2l_{n-1}}{\beta_{n-1}c} + \pi \tag{1.15}$$

where the half cell length is $l_{n-1} = \frac{\beta_{s,n-1}\lambda}{4}$ and the distance between the centers of two gaps is

$$L_n = l_{n-1} + l_n = \frac{(\beta_{s,n-1} + \beta_{s,n})\lambda}{4}. \tag{1.16}$$

The phase change relative to the synchronous particle is then

$$\Delta(\phi - \phi_s)_n = \pi\beta_{s,n-1}(\frac{1}{\beta_{n-1}} - \frac{1}{\beta_{s,n-1}}) \tag{1.17}$$

Assuming $\delta\beta \ll 1$ with $\delta\beta = \delta W/mc^2\gamma_s^3\beta_s$ we find the equations relating the change in phase and energy for an arbitraly particle of the beam, i.e.

$$\Delta(\phi - \phi_s)_n = -\pi\frac{W_{n-1} - W_{s,n-1}}{mc^2\gamma_{s,n-1}^3\beta_{s,n-1}^2} \tag{1.18}$$

$$\Delta(W - W_s)_n = qE_0TL_n(cos\phi_n - cos\phi_{s,n}) \tag{1.19}$$

Those equations can be solved numerically to determine the behaviour of any arbitraly particle with respect to the synchronous one: in particular, it is important to define under which conditions $\Delta(\phi - \phi_s)$ and $\Delta(W - W_s)$ remain a finite quantity, that is, the motion of the beam is stable.

To determine the stability condition it is convenient to convert the difference equations to differential ones by treating n as a a continuous variable related to the axial distance s by the simple relation $n = 2s/\beta_s\lambda$.

$$\Delta(\phi - \phi_s) \rightarrow \frac{d(\phi - \phi_s)}{dn} \text{ and } \Delta(W - W_s) \rightarrow \frac{d(W - W_s)}{dn} \tag{1.20}$$

where n is a continuous variable.

We get then the coupled equations

$$\gamma_s^3\beta_s^3\frac{d(\phi - \phi_s)}{ds} = -2\pi\frac{W - W_s}{mc^2\lambda} \tag{1.21}$$

$$\frac{d(W - W_s)}{ds} = qE_0T(cos\phi - cos\phi_s). \tag{1.22}$$

By differentiating the first equation and then using the second, we determine the equation of the longitudinal motion:

$$\gamma_s^3\beta_s^3\frac{d^2(\phi - \phi_s)}{ds^2} + 3\gamma_s^3\beta_s^3\frac{d(\gamma_s\beta_s)}{ds}\frac{d\Delta\phi}{ds} = -\frac{2\pi qE_0T}{mc^2\lambda}(\cos\phi - \cos\phi_s) \tag{1.23}$$

which, assuming a slow acceleration rate reduces to

$$\gamma_s^3\beta_s^3\frac{d^2(\phi-\phi_s)}{ds^2} = -\frac{2\pi qE_0T}{mc^2\lambda}(\cos\phi - \cos\phi_s) \tag{1.24}$$

or equivalently to

$$d\frac{d\Delta\phi}{ds} = -\Omega^2(\cos\phi - \cos\phi_s)ds \Leftrightarrow \tag{1.25}$$

$$d\frac{d\phi}{ds} = -\Omega^2(\cos\phi - \cos\phi_s)ds \Leftrightarrow \tag{1.26}$$

$$d\phi' = -\Omega^2(\cos\phi - \cos\phi_s)ds \tag{1.27}$$

where

$$\Omega^2 = \frac{2\pi qE_0T}{mc^2\lambda\beta_s^3\gamma_s^3}. \tag{1.28}$$

This equation is extremely useful since it determines the stable region in the $\Delta W - \Delta\phi$ phase space: using the relation $ds = d\phi/\phi'$ and multypling for ϕ' we get

$$\phi' d\phi' = -\Omega^2\phi'(cos\phi - cos\phi_s)d\phi \tag{1.29}$$

which after integration and by use of Eq.1.21 becomes

$$\frac{1}{2}\frac{2\pi}{\lambda\gamma_s^3\beta_s^3}\frac{(\Delta W)^2}{(mc^2)^2} + \frac{qE_0T}{mc^2}(sin\phi - \phi cos\phi_s) = Const = H_\phi. \tag{1.30}$$

This equation can be interpretated as an Hamiltonian with potential

$$V_\phi = \frac{qE_0T}{mc^2}(sin\phi - \phi cos\phi_s). \tag{1.31}$$

Such a potential is well defined if $-\pi \leq \phi_s \leq 0$ and, recalling that an acceleration happens for $-\pi/2 \leq \phi_s \leq \pi/2$, we conclude that a stable motions occurs for $-\pi/2 \leq \phi_s \leq 0$.

The stable region extends from $\phi_2 < \phi < -\phi_s$ where ϕ_2 has to be numerically solved. It is possible to demonstrate that, in good approximation, $\phi_2 \sim 2\phi_s$.

In this way we can determine the motion in the phase space defining the stability region, the Separatrix, as explained in Fig.1.11.

To summerize, we can conlude that in a linear accelerator:

- the synchronous phase has to be chosen between 0 and -$\pi/2$ with respect to the electric field;
- any arbitrary particle with phase ϕ will have stable motion only if $-2|\phi_s| \leq \phi \leq |\phi_s$;
- the maximum allowed energy spread from the synchronous energy is

$$\Delta W_{max} = \sqrt{\frac{2qTmc^2\lambda{\beta_s}^3{\gamma_s}^3}{\pi}}; \tag{1.32}$$

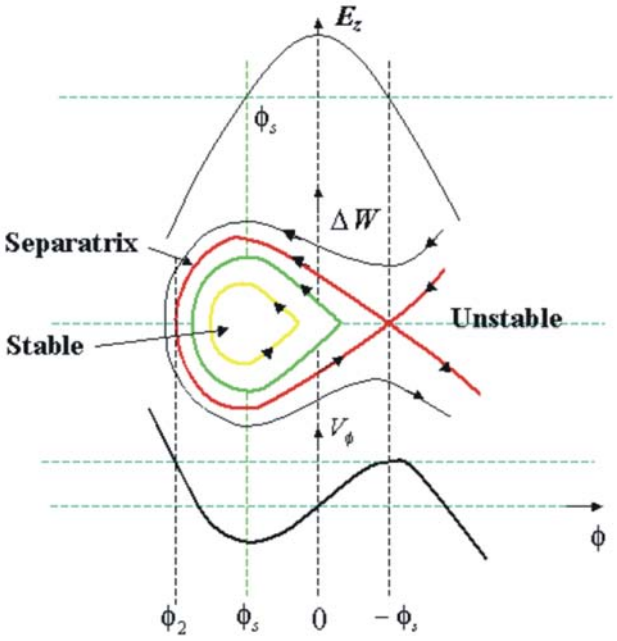

Figure 1.11: On top the accelerating field as a cosine function of the phase. In the middle, some trajectories in the phase space are shown including the Separatrix, the limit trajectory for stable motion. Finally the potential function is shown illustating the meaning of the synchnous phase in the phase space.

1.3.2 Transversal stability

In the gap not only an axial electric field component is present, but also a radial component which will influence all the off-axis particle: since the energy of those particles is higher in the second half gap than in the first part, the net result is a defocusing effect which can eventually result in the loss of the beam. Like for longitudinal motion, we must analyze under which condition this effect can be avoided.

The Maxwell equations in cylindrical coordinates with rotational symmetry can be expressed as

$$\vec{\nabla} \cdot \vec{E} = 0 \quad \rightarrow \quad \frac{1}{r}\frac{\partial (rE_r)}{\partial r} + \frac{\partial E_z}{\partial z} = 0 \tag{1.33}$$

$$(\vec{\nabla} \times \vec{E})_z = \frac{1}{c^2}\frac{\partial \vec{E_z}}{\partial t} \quad \rightarrow \quad \frac{1}{r}\frac{\partial (rB_\theta)}{\partial r} = \frac{1}{c^2}\frac{\partial E_z}{\partial t} \tag{1.34}$$

$$(\vec{\nabla} \times \vec{E})_r = \frac{1}{c^2}\frac{\partial \vec{E_r}}{\partial t} \quad \rightarrow \quad -\frac{\partial B_\theta}{\partial z} = \frac{1}{c^2}\frac{\partial E_r}{\partial t} \tag{1.35}$$

$$(\vec{\nabla} \times \vec{E})_\theta = -\frac{\partial \vec{B_\theta}}{\partial t} \quad \rightarrow \quad \frac{\partial E_r}{\partial z} - \frac{\partial E_z}{\partial r} = -\frac{\partial B_\theta}{\partial t} \tag{1.36}$$

Assuming near the axis E_z indipendent from r, the integration of those equations leads to

$$E_r = -\frac{r}{2}\frac{\partial E_z}{\partial z} \tag{1.37}$$

$$B_\vartheta = \frac{1}{c^2}\frac{r}{2}\frac{\partial E_z}{\partial t}. \tag{1.38}$$

Using the Newton law we have $F_r = q(E_r - \beta c B_\vartheta)$, resulting in a momentum variation

$$\Delta p_r = -\frac{q}{2}\int_{-l/2}^{l/2} r\left(\frac{\partial E_z}{\partial z} + \frac{\beta}{c}\frac{\partial E_z}{\partial t}\right)\frac{dz}{\beta c}. \tag{1.39}$$

It is useful to use the relation

$$\frac{dE_z}{dz} = \frac{\partial E_z}{\partial z} + \frac{1}{\beta c}\frac{\partial E_z}{\partial t} \tag{1.40}$$

and recalling that $E_z = E_0 cos(\omega t + \phi)$ and by use of the definition of T we get, after integration,

$$\Delta p_r = -\frac{q\pi E_0 T L \sin\phi}{\gamma^2\beta^2\lambda c} \tag{1.41}$$

Finally, assuming $\phi = \phi_s$ we get

$$\Delta p_r = -\frac{q\pi E_0 T L \sin\phi_s}{\gamma^2\beta^2\lambda c}. \tag{1.42}$$

From this equation it results that for $-\pi/2 \leq \phi_s \leq 0$ the synchronous particle will increase its transversal velocity, that is, a longitudinal stable motion implies a defocusing effect on the beam.

This is the reason why beam focusing devices, like magnetic quadrupoles, are needed all along a linear structure. In classical Alvarez structures they are mounted inside the drift tubes: unfortunately this results in dispersion of the electric field out of the axis which reduces the RF efficiency of the cavity. In order to reduce this effect, several alternative schemes have been proposed like the APF [15] (alternative phase focusing) which defines alternatevely a positive and negative synchronous phase so that both longitudinal and transversal stability is ensured.

An innovative scheme alternative to APF is the KONUS beam dynamics, which has been used as accelerating scheme for many existing H-type linacs and which will be used as well for the GSI proton injector. A complete description of the KONUS concept can be found in Sect.2.2.1

1.4 Actual Projects based on linacs

In order to give a general overview on the present worldwide activities in the field of proton-linacs, this chapter presents some of the most actual projects which are entirely or partially based on a high intensity proton injector, such as FAIR at GSI (Germany), SNS at ORNL (USA), CERN Linac4 (Switzerland), and JPARC (JAPAN).

1.4.1 FAIR: a Facility for Antiprotons and Ions Research

The FAIR Project [16] (Facility for Antiprotons and Ions Research), sketched in Fig.1.12, is the new international facility under development at GSI, Darmstadt, Germany. The heart of FAIR consists of a superconducting double-synchrotron, the SIS 100/300, with magnetic rigidities of 100 and 300 Tm, respectively. The existing GSI accelerators UNILAC and SIS18 will serve as injector chain after a consistent upgrade of their intensity capabilities: FAIR will in fact supply rare isotope (RIBs) and antiproton beams with

unprecedented intensity and quality, which requires a consistent update of the existing GSI accelerator complex. An important feature of FAIR is that, due to the intrinsic cycle times of the accelerators and storage-cooler rings, up to four research programs can be run in parallel. This allows a rich and multidisciplinary research program, covering the most important field of research in the frame of atomic and particle physics, such as QCD studies with cooled beams of antiprotons, nucleus-nucleus collisions at highest baryon density, nuclear structure and nuclear astrophysics investigations with nuclei far off stability, high density plasma physics, atomic and material science studies, radio-biological investigations and other application-oriented studies.

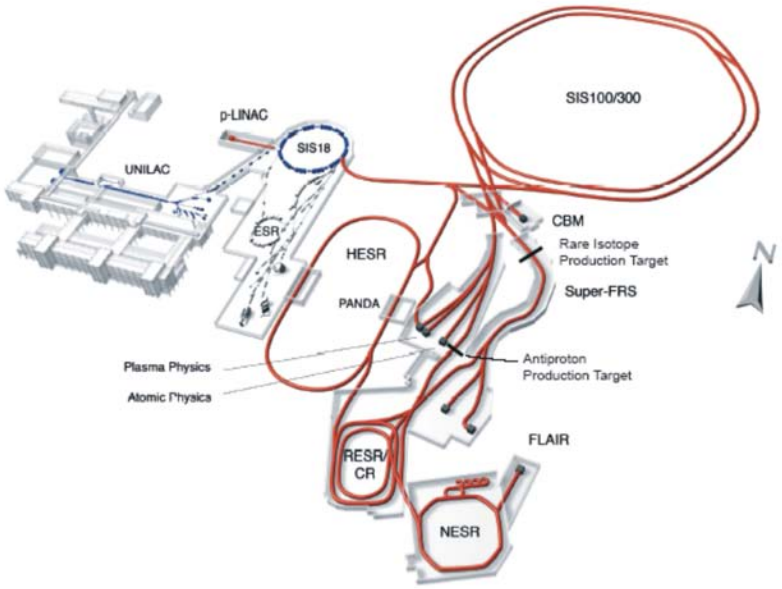

Figure 1.12: Layout of the existing GSI facility, $UNILAC, SIS18, ESR$ on the left and the planned FAIR facility on the right: the superconducting synchrotrons $SIS100$ and $SIS300$, the collector ring CR, the accumulator ring $RESR$, the new experimental storage ring $NESR$, the rare isotope production target, the superconducting fragment separator $Super-FRS$, the proton linac, the antiproton production target, and the high energy antiproton storage ring $HESR$. Also shown are the experimental stations for plasma physics, relativistic nuclear collisions (CBM), radioactive ion beams ($Super-FRS$), atomic physics, and low-energy antiproton and ion physics ($FLAIR$).

The antiproton physics program at FAIR demands a primary proton beam of $2 \cdot 10^{16}$ p/h, which is much beyond the capabilities of the existing UNILAC: for this reason a dedicated proton linac has to be used as injector into the SIS 18/100 synchrotrons.

The scheme of the 325 MHz, 70 MeV FAIR proton injector is schetched in Fig.1.14: an ECR source delivers up to 100 mA proton beam which is accelerated by an RFQ up to energy of 3 MeV. In a first step 35 mA will be accelerate within a 70 μs RF pulse into the main linac composed of 12 CH-type cavities grouped in 6 pairs of coupled structure. At the output energy of 70 MeV the beam is injected into the SIS18 and further into the SIS100 for the production of an intense secondary antiproton beam.

In a final update of the machine foresees an update of the current of to 70 mA which represents also the design current.

The CH-DTL is a new kind of cavity, under development at the Frankfurt University, which represents the extension of well established Interdigital H-cavities to higher

frequency. Such a structure, as shown in Fig.1.13, is characterised by the lack of internal focusing elements which allows the construction of extremely compact cavities characterized by a higher shunt impedance when compared to conventional RF structure. In Tab.1.1 the main parameters of the FAIR Proton injector are listed.

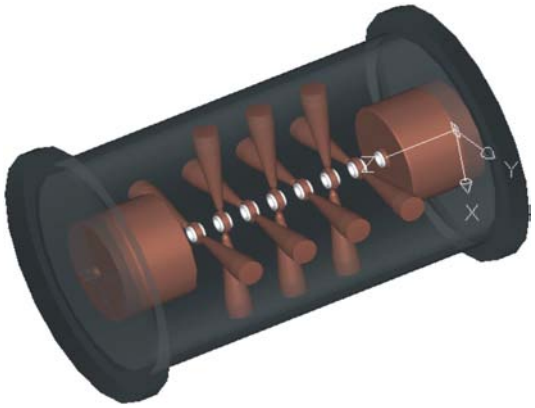

Figure 1.13: The CH-DTL.

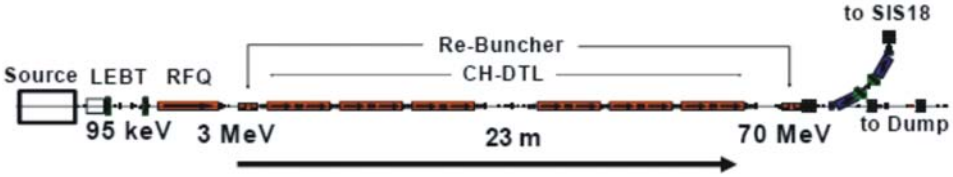

Figure 1.14: The layout of the GSI Proton Injector for FAIR

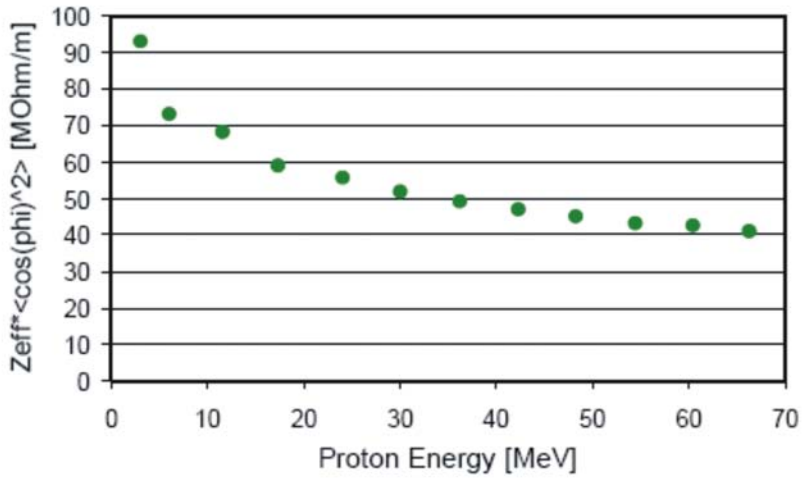

Figure 1.15: The expected effective shunt impedance for the FAIR proton injector.

A complete description of this machine will be found in the following chapters of this thesis where the physical motivations for the construction of this new linac are described

together with a deep explanation of all the conceptual steps both in terms of structure engineering as well as in terms of beam dynamics design.

Length [m]	30
Output Energy [MeV]	70
Average Beam Power [kW]	6.86 (13.72 design)
Frequency [MHz]	325.244
Repetition Rate [Hz]	4
Peack Current [mA]	35 (70 design)
Beam Pulse Length [ms]	0.36
Protons per Pulse $[10^{12}]$	7.8
Transverse norm emitt. $[\mu$**m**$]$	4.3
Longitudinal norm emitt. [keV $\cdot$ **ns]**	17

Table 1.1: The main parameters of the FAIR proton injector.

1.4.2 The Spallation Neutron Source: SNS

SNS (Spallation Neutron Source) is an accelerator-based neutrons source in Oak Ridge, Tennessee, USA [17]: it produces high intensity pulsed neutrons to perform materials and biological research. It consists of a linac, an accumulator ring and a high power target station (see Fig.1.16). SNS is the first spallation neutron source driven by a linac instead of a synchrotron like ISIS ar RAL, Great Britan, or by a cyclotron like at PSI, Switzerland.

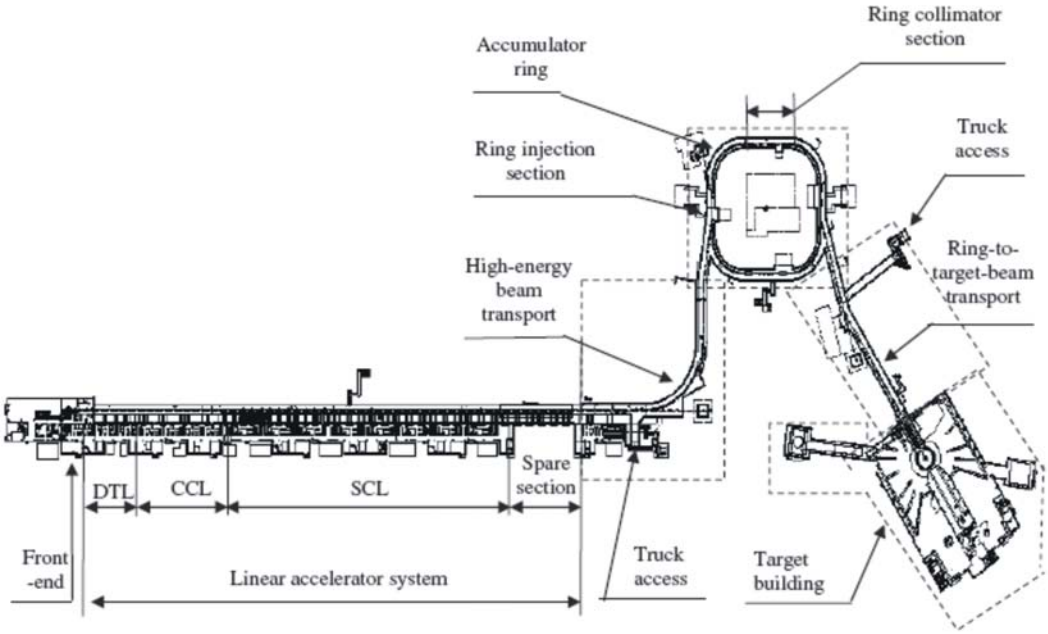

Figure 1.16: Layout of the SNS Facility.

The SNS front-end system includes the ion source delivering up to 47 mA H^- beam in a 1 ms long pulse with a repetition rate of 60 Hz; the standard operation foresees an

Parameters	DTL	CCL	SPL
Energy Range [MeV]	2.5 - 87	87 - 187	187-(394)- 1000
Length [m]	36	55	157
Accelerating gaps	216	384	486
Frequency [MHz]	402.5	805	805
No. of Klystrons	6	4	92
Power requirements [MW]	2.5	5	0.55

Table 1.2: The main parameters of each structure for the SNS linac.

average current of 1.4 mA accelerated up to 2.5 MeV by an RFQ and then delivered to a large linear accelerator which provides further a acceleration up to 1 GeV.

The linac consists of a 402.5 MHz Drift tube linac (DTL) of the Alvarez type, divided in 6 tanks for a total length of 36 meters, which brings the protons to 87 MeV where the beam passes into the 55 m long, 805 MHz coupled-cavity linac (CCL). By those cavities the beam is sped up to 187 MeV where the superconducting linac (SCL) begins. The 157 m long SCL consists of 11 medium-β cryomodules ($\beta = 0.61$) up to 378 MeV and 12 high-β cryomodules, ($\beta = 0.82$) which provide the full beam energy: at this point the beam is collected into the accumulator ring and then injected into the liquid mercury target station.

The SNS linac is a good example of the strategy needed to build a high power linac: it presents, in fact the fundamental steps to achieve the higher efficiency along the whole machine. The room temperature section is based on two different structures operating at different frequencies: it begins with a $\beta\lambda$ DTL and then it switches to a $\beta\lambda/2$ structure, the CCL, which is operated at double frequency. These solutions are common techniques used to increase the efficiency of a normal conducting linac since the shunt impedance decreases for higher energies and and increases with the operating frequency at reduced beam aperture, as shown in Fig.1.18 where the shunt impedance for the normal conducting section is shown.

Finally, for energies higher than 180 MeV, typically, the superconducting option becomes preferably because of the low efficiency of room temperature structure in the high energy range.

Similar strategies are adopted in the next examples, the CERN LINAC 4 and the new Proton Injector for JPARC.

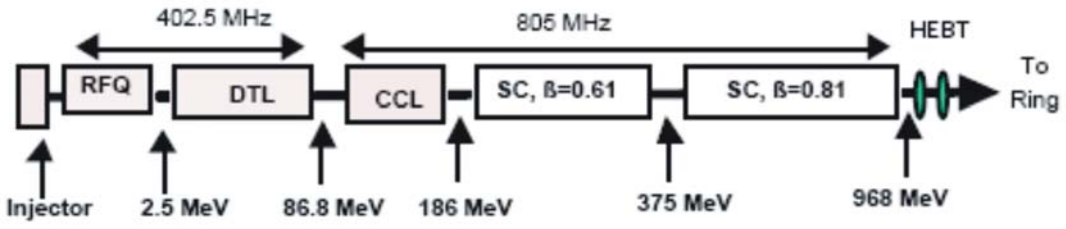

Figure 1.17: The SNS linac layout.

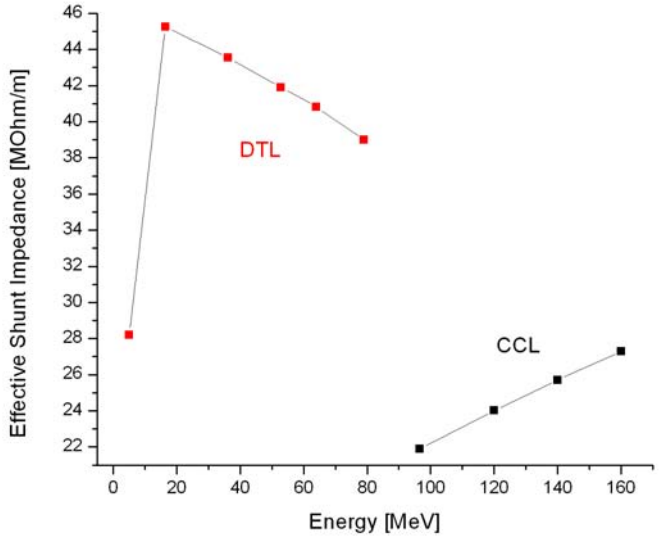

Figure 1.18: The shunt impedance for the normal conducting section of SNS.

Output Energy [MeV]	1000
Output Energy Stability [MeV]	± 1.5
Average Current [mA]	1.56
Beam Pulse Length [μs]	1000
Protons per pulse	$9.3 \cdot 10^{12}$
Repetition Rate [Hz]	60
Emittance (rms, norm, initial) [$\pi\mu$ rad]	0.27
Emittance(rms, norm, final) [$\pi\mu$ rad]	≤ 0.5
Beam Loss [W/m]	≤ 1
Beam Duty Factor [%]	6

Table 1.3: The beam parameters at the exit of the SNS linac.

1.4.3 CERN LINAC 4

The mid-term update program of CERN foresees for the period 2008-2011 the construction of a new 160 MeV, 40 mA H^- linac, called LINAC 4 [18], which will replace the old 50 MeV, 202 MHz LINAC 2 developed at the end of the seventies: the main goal of this new machine is to increase the brilliance of the PS-LHC complex by reducing the space charge effect of a factor 2 at the injection into the SPS, and to increase the number of protons available for the non-LHC physics programs like ISOLDE [19]. The whole project profits a lot from the avaibility of the old LEP RF equipment, especially the waveguides and the 352 MHz, 1.1 MW klystrons, which results in a considerable reduction of the needed budget.

Like the SNS linac also this machine will commit by a DTL and by a CCL while, after the jump in frequency from 352 to 704 MHz, the high energy section consists of a Side Coupled Linac.

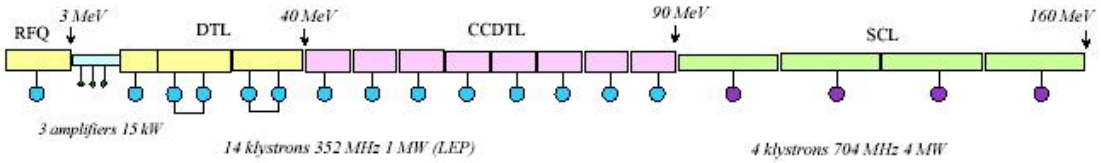

Figure 1.19: CERN Linac4 layout.

Fig.1.19 illustrates the general layout of this linac. The low energy section has the same scheme as for the GSI proton injector, the ions are extracted at 95 keV from the source and then accelerated by a 4-vane RFQ to 3 MeV where the beam enters the main linac. From 3 to 40 MeV the CERN design is based on 3 DTL tanks housing a single permanent magnetic quadrupole (PMQ): the first module is equipped by a single klystron while the other tanks require each 2 power amplifiers for a total RF power of 4 MW.

Length [m]	80
Output Energy [MeV]	160
Average Beam Power [kW]	5.1
Frequency [MHz]	352
Repetition Rate [Hz]	2
Current [mA]	40
Beam Pulse Length [ms]	0.4
Protons per Pulse	10^{14}
Transverse rms emitt. [mu **m**]	0.36
Longitudinal rms emitt. [MeV deg]	0.19

Table 1.4: The main parameters of Linac4.

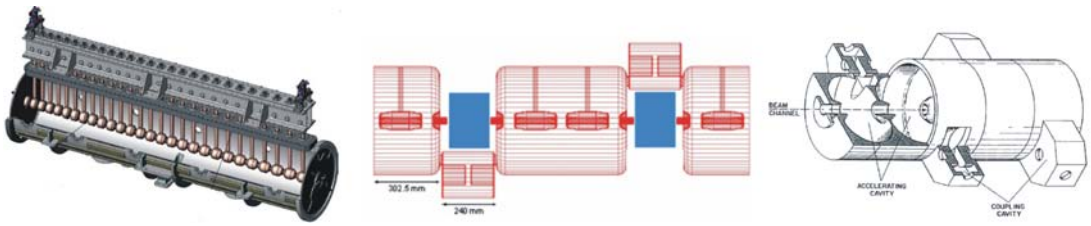

Figure 1.20: The proposed structures for LINAC 4: on the left, a prototype of the first DTL module, in the center the CCDTL and, on the right, an example of Side Coupled Linac.

After the DTL, the beam is accelerated up to 90 MeV by 8 CCDTL modules each consisting of a 3-gaps caviy fed by a single klystron, while triplet electromagnetic quadrupoles (EMQ) are placed between each tank. The beam then passes into the 704 MHz Side Coupled Linac for the final acceleration up to 160 MeV.

The Side Coupled Linac can be considered as the standard structure for high energy acceleration and, in the LINAC 4 design, it consists of 20 tanks grouped in 4 couples each powered by a single klystron: each tank contains 11 cells and it is operated at the constant gradient of 4 MV/m.

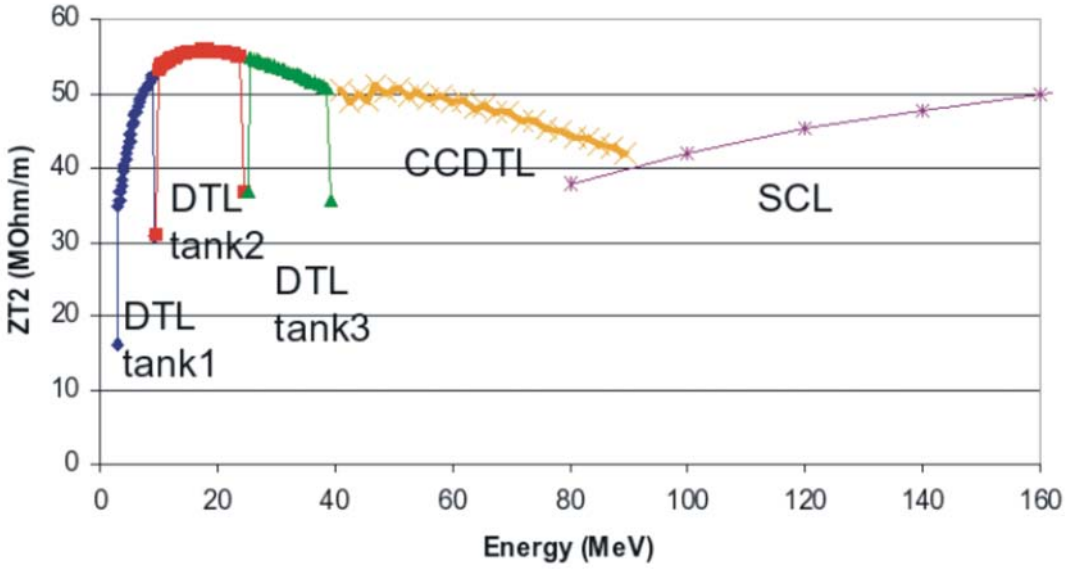

Figure 1.21: The expected effective shunt impedance for Linac4: those numbers represent a very ambitious design with respect to RF efficiency.

Parameter	**DTL**	**CCDTL**	SPL
Output Energy [MeV]	40	90	160
Frequency [MHz]	352	352	704
Gradient [MV/m]	3.3-3.5	2.8-3.9	4
No. Of Tanks	3	8	20
No. Of Klystrons	5	8	4
Length [m]	13.4	25.2	28
Synchr. Phase [deg]	-30/-20	-20	-20

Table 1.5: The structure parameters for the DTL,CCDTL and SPL of Linac4.

In Fig.1.21 the efficiency of each of these structure is presented: according to the particle velocity the most efficient RF structure will be used. It is very important to remark that the shunt impedance presented in this picture shows extraordinary numbers for the efficiency of a DTL which has been requiring an enormous R&D on the structure design. Moreover, the choice to use inner permanent magnets as focusing elements in the low energy side implies serious constraints on the mechanical tolerances since beam losses due to misalignments of the drift tubes could bring to irreparable damages the magnets: this implies a beam loss profile less than 1 W/m which is a real serious constraints in terms of mechanical tolerances.

Finally, a superconducting option is under discussion for a future update of the structure in terms of higher achievable energy. As shown in Fig.1.22, this option is based on two kinds of superconducting cavities, the first up to $\beta = 0.65$, and the second up to $\beta = 1$, for a final energy of 3.5 GeV.

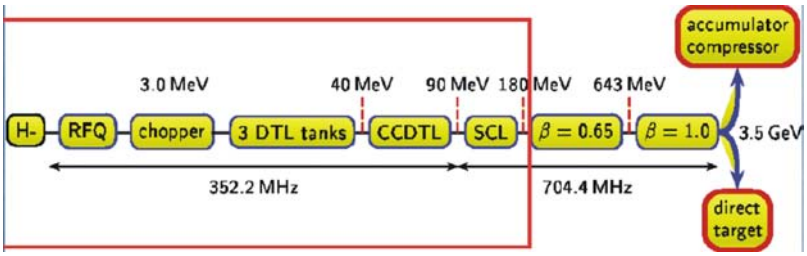

Figure 1.22: The proposed design for the upgrade of LINAC4 to the energy of 3.5 GeV.

1.4.4 JPARC

In Japan proton linac activities are related to the construction of the JPARC multi purposes facility. The accelerator complex consists of a linac, a 3 GeV rapid cycling synchroton and a 50 GeV synchrotron. Four experimental areas are foreseen, focused on nuclear waste transmutation, materials and life science, hadron beam physics and neutrino generation.

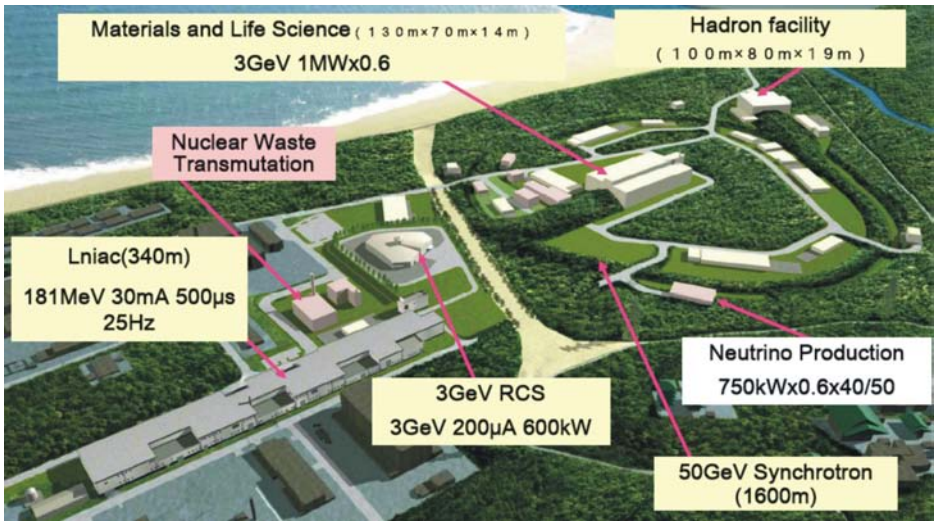

Figure 1.23: The JPARC Complex.

The 324 MHz linac [21] accelerates a 30 mA H^- beam to the final energy of 181 MeV; in a future upgrade a superconducting structure will increase the final energy up to 400 MeV for the injection into the RCS and up to 600 MeV for the nuclear waste transmutation program.

The ion source delivers 50 keV H^- which are further accelerated by a RFQ structure to energy of 3 MeV where the main linac starts. As for CERN and SNS, this linac is also based on traditional DTL's up to the energy of 50 MeV where a separated DTL (SDTL) begins. This kind of structure differs from DTL because the focusing elements are installed only between adjacent tanks and not in the drift tubes which increases significantly the shunt impedance. In a first step, the 30 mA beam is accelerated with a repetition rate of 25 Hz, while after an upgrade based on superconducting Anular Coupled Structure the current will be increased to 50 mA at 50 Hz repetition rate.

The JPARC linac is the first linac based on a 325 MHz resonance frequency and

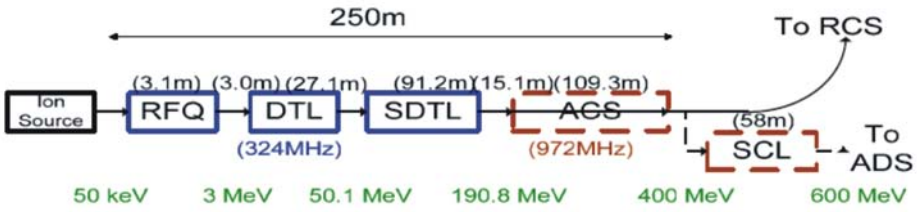

Figure 1.24: The JPARC linac scheme.

Frequency [MHz]	325
Output Energy [MeV]	180
Pulse Current [mA]	30
Protons per pulse	$9.4 \cdot 10^{13}$
No. Of Klystrons	20
Klystron Power [MW]	2.5
RF Pulse Length [ms]	0.650
Beam Pulse Length [ms]	0.500
Length [m]	250

Table 1.6: The parameters of the JPARC linac.

for this reason it pushed the industrial development of dedicated power supplies. The resulting avaibility on the market of these unexpensive, stable and high power level klystrons has played a key role in many other projects: GSI, Fermilab [20] and RAL [22] have decided to base their future projects on such a frequency mainly because of the avaibility of those RF sources.

Tab.1.7 summarizes and compares the main features of the described facilities: as one can see all of them are characterized by a high intensity of the beam, in the order of 10^{12} proton per pulse, which has been requiring an intensive investigation in terms of beam dynamics as well as in terms of structure design.

We notice, in particular, that the GSI proton injector is the only project based on a single structure: this is due not to lower output energy but as well to the higher efficiency of the chosen structure which, especially at low energy, is characterized by the highest shunt impedance ever reached in this region.

Parameter	GSI	CERN	SNS	JPARC
Output Energy [MeV]	70	160	968	181
Peak Current [mA]	70 (35)	40	38	30
Protons per pulse [10^{12}]	7.8	100	9.3	93
Frequency [MHz]	325	352-704	402.5-805	325-975
Length [m]	30	78	180	250
Klystrons Power [MW]	2.5	0.8-4	1.25-2.5	2.5
No. of Klystron [m]	6	17	3-56	20
Beam Pulse Length [μs]	36	160	1000	500

Table 1.7: A comparison between some of the most recent worldwide linac accelerator

The main features of the CH will be described in the next chapter where, above a deep technical description, the first experimental results from scaled models will be illustrated and commented.

Chapter 2

The CH-DTL

2.1 H-mode DTL's

H-type cavities are characterized by the direction of the RF magnetic field which is oriented parallel and antiparallel with respect to the beam axis. Closed field loops are provided by connecting field lines with opposite orientation at the cavity ends. At present DTL versions exist for the H_{110} (IH) mode as well as for the H_{210} mode (CH) (Fig.2.1).

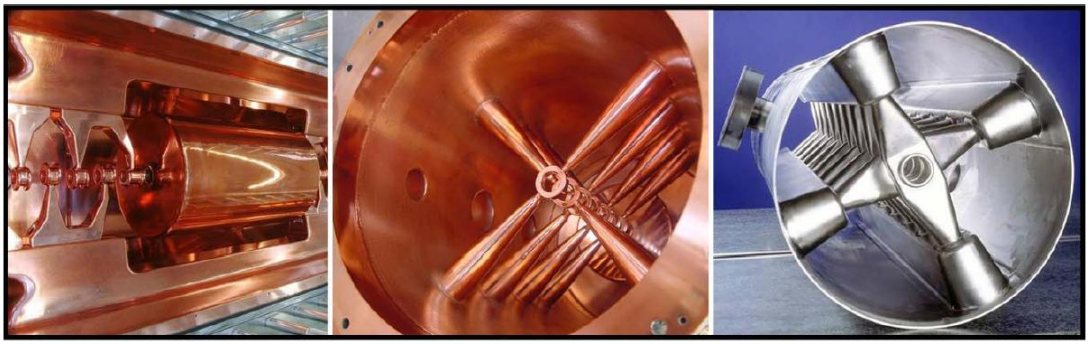

Figure 2.1: The Family of H-Mode DTL. On the left the IH, in the middle the cooper plated room temperature CH, and, on the right, the bulk niobium prototype for the superconducting CH.

H-type linacs presents the important capability to reduce the capacitance between the drift tube concentrating the accelerating field close to the beam axis which allows to increas the operating frequency resulting in a higher shunt impedance in the low-medium β range. Moreover, they are π-mode structures and it is well demonstrated that such a cavities can stand very high RF fields in routine operation since the small surface of the drift tubes allow a higher value of the Kilpatrich factor. H-cavities present many advantages against the classical Alvarez structure based on a FODO lattice. The shunt impedance can be in general significantly improved by use of long sections made by slim tubes without any internal focusing elements which allows to reach high effective field gradients (up to 10 MV/m [23]) and to use a higher resonance frequency already at lower beam energies. The transverse focusing is provided by quadruple lenses placed at the end of every drift tube section. In this way effective shunt impedances around 100 $M\Omega/m$ can be reached in the 3 MeV energy range.

Finally, thanks to its geometry which allows a very efficient cooling scheme together with a high mechanical robustness, the CH can be operated in superconducting and/or continuous wave.

These are major advantages with respect to conventional RF DTL which has made IH linacs the outstanding cavities concerning heavy ions acceleration in the low-medium energy range. The IH has been employed as ion accelerator at Munich University (SCHWEIN [24]), GSI (HLI [25], HSI [26]), CERN (LINAC3 [27], REX-ISOLDE [28]), at the cancer therapy facilities HIT (Germany [29]) and CNAO (Italy [30]), at Triumph (ISAC) and will be used in recent approved project like as for the gold injector at BNL (USA, [31]), as heavy ion injector at Lanzhou (China) and as proton driver at the Frankfurt neutron generator FRANZ (Germany [32]).

The CH is still a new concept which has been attracting a growing interest in the linac community: at the moment, besides GSI, this new cavity will be employed in the new proton booster at Fermilab and it's planned to be used in the IFMIF [33] and EUROTRANS [34] new facilities.

2.2 Interdigital Linac: The IH-DTL

The Interdigital H-type drift tube structure was mentioned as an attractive solution for proton acceleration up to 30 MeV already at the 1956 CERN Symposium by J.P. Blewett [35]. Important improvements and innovations were achieved during the design phase of many H-linac projects [36], including the RFQ development from the early beginnings. Nowadays it is considered as the standard structure for velocity profile below $\beta = 0.1$

Differently from Alvarez structures which are exited in the Transverse Magnetic Mode (TMM), empty H mode cavities are exited in the Transverse Electric Mode (TEM) which presents no longitudinal electric field component: the accelerating component is generated by the stems supporting the drift tube as explained in Fig.2.2.

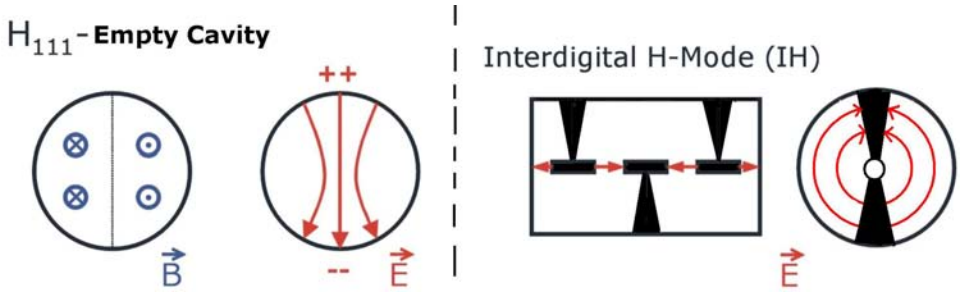

Figure 2.2: A comparison between an empty cylindrical cavity exited in the H_{111} mode and the corresponding IH linac: it is possible to note how the electric field distribution is changed by the capacity induced by the drift tubes.

The Maxwell equations applied to a cylindrical cavity of radius R and length L exited in the H_{111} mode lead to the following field distribution:

$$B_z = B_0 J_1\left(1.841\frac{r}{R}\right)\cos\vartheta\sin\left(\frac{\pi z}{l}\right)e^{i\omega t} \tag{2.1}$$

$$B_r = \frac{\pi}{l}\frac{R}{1.841}B_0 J_1\left(1.841\frac{r}{R}\right)\cos\vartheta\cos\left(\frac{\pi z}{l}\right)e^{i\omega t} \tag{2.2}$$

$$B_\vartheta = -\frac{\pi}{l}\frac{R^2}{3.389r}B_0 J_1\left(1.841\frac{r}{R}\right)\sin\vartheta\cos\left(\frac{\pi z}{l}\right)e^{i\omega t} \quad (2.3)$$

$$E_r = i\omega\frac{R^2}{3.389r}B_0 J_1\left(1.841\frac{r}{R}\right)\sin\vartheta\sin\left(\frac{\pi z}{l}\right)e^{i\omega t} \quad (2.4)$$

$$E_\vartheta = i\omega\frac{R}{1.841}B_0 J_1{}'\left(1.841\frac{r}{R}\right)\cos\vartheta\sin\left(\frac{\pi z}{l}\right)e^{i\omega t} \quad (2.5)$$

$$E_z = 0 \quad (2.6)$$

where the resonance frequency is given by

$$\omega = \frac{c}{\sqrt{(\frac{1.841}{R})^2 + (\frac{\pi}{l})^2}}. \quad (2.7)$$

The presence of the drift tube increases significantly the capacitance of the cavity reducing the resonance frequency as calculated from the previous equations. As an example, Fig.2.3 shows us the RF structure of CERN IH-DTL lead linac. The averaged cavity diameter is 335 mm and the length 1.42m. The H_{111} mode of the corresponding empty cylinder has a resonance frequency of 535.3 MHz compared to the measured one of 202.56MHz, less than 40 % of the corresponding value. The high efficency of the IH is due exactly to this extra capacitance which is localized between the drift tubes.

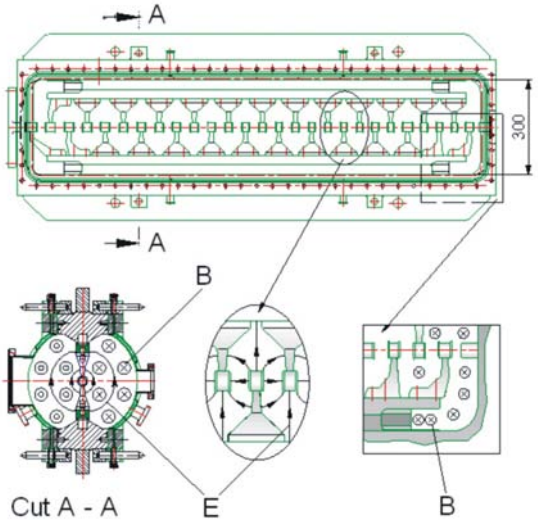

Figure 2.3: An example of IH-DTL: the CERN LINAC3 lead injector with details of the fields distribution inside the cavity.

Finally, particular shape of the end cells results in a flat voltage distribution of the electric field approximating the H_{110} mode which could not exist in an empty cylindrical cavity. This is well demonstrated in Sect.2.1.3 where the state of the art reached by this kind of cavity is illlustrated and commented.

2.2.1 The KONUS beam dynamics

In the first chapter we have seen how a major problem in the design of a linac consists in ensuring a stable motion of the beam: in particular, we have seen how the condition

for a longitudinal stable motion implies a defocusing effect on the beam. The standard solution to use big drift tubes containing a focusing element (typical of E-mode cavities) results in a dispersion of the electric field far from the beam axis which limits the achievable accelerating gradient, both because the shunt impedance is inversally proportional to the capacity, and because larger drift tubes can be easily subject to sparkling phenomena.

To overcome this problem an alternative focusing scheme has been proposed by U.Ratzinger at the end of the eighties, the KONUS (KOmbinierte NUll grad Structure) Beam Dynamics [37].

A KONUS period consists of:

- transverse focusing by a quadrupole triplet;
- longitudinal focusing and matching by a short negative synchronous phase structure;
- main acceleration with transversal defocusing along a 0° structure with asynchronous beam injection;

The heart of KONUS consists in the the main acceleration section defined on a a 0° synchronous phase: in a classical DTL this would correspond to the maximun energy gain with no RF transversal defocusing as well as with no RF longitudinal focusing. The key point is that the injection in this section occurs with asynchronous energy, that is, the synchronous particle which defines the lattice doesn't correspond any more with the bunch center, as shown in Fig.2.4.

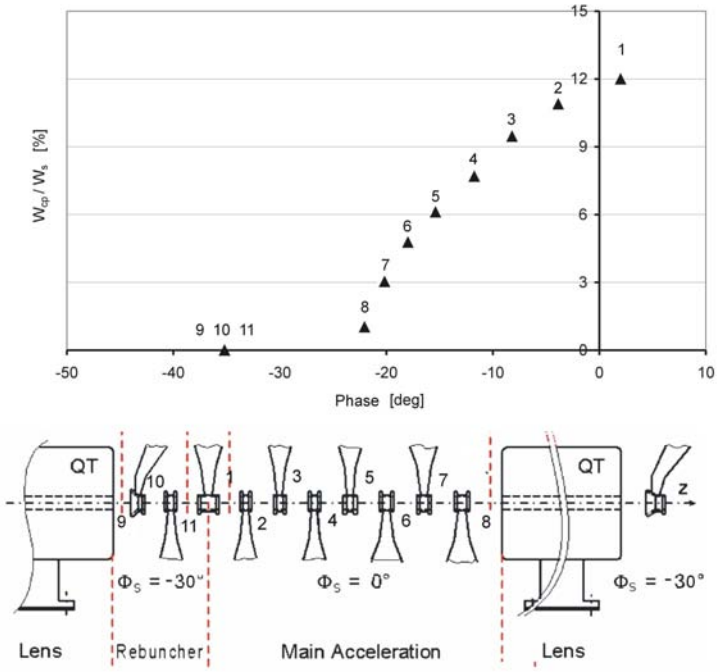

Figure 2.4: Schematic representation of the KONUS period: on top the buch behaviour in the phase space and, bottom, a typical IH structure operated with KONUS.

Let's analyze the motion in the longitudinal phase space centered on the 0° phase and on the synchronous phase. The bunch center starts its motion on the border between

the first and second quadrant with a higher energy: due this extra energy the bunch center will encounter the next gap when the field is not on the crest and with a more negative phase, thus reducing the energy spread with the synchrounous particle. This corresponds to a counterclockwise motion in the phase space

The particles close to the center of the bunch experience a longitudinal focusing effect since earlier particles see a lower electric field than the bunch center.

This stability would vanish as the bunch center would reache the third quadrant where earlier particles would encounter a higher accelerating field.

At this point, the accumulated radial defocusing effect is corrected by a quadrupole triplet which can be host inside as well as outside the cavity.

After the focusing element, in order to avoid longitudinal defocusing and to rebuch the beam, the synchrounous phase is reset to a negative value which corresponds now to the center of the bunch. It is numerically proved that in this way a stable motion occurs both transversally as well as longitudinally.

The long drift section without focusing elements results in very compact and cheaper structures which can stand extremely high accelerator gradient reducing sensibly the lenght of the machine.

2.2.2 The state of the art: The HIT IH

The IH employed as proton and heavy ion injector at the Heidelberg (HIT, Germany) and Pavia (CNAO, Italy) cancer therapy facilities represents very well the state of the art achieved in the development of interdigital linacs. Such a cavity can accelerate different ion species up to $^{12}C^{4+}$ from the injection energy of 400 AkeV to the extraction energy of 7 AMeV.

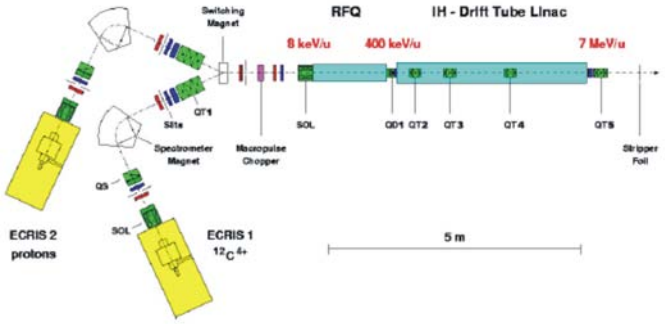

Figure 2.5: The injector scheme for the cancer therapy facility in Heidelberg (HIT).

The cavity contains four acceleration sections, 56 gaps in total, connected by three internal electromagnetic triplets needed for transverse beam focusing. The high shunt impedance allows to apply the effective voltage gain of 23.7 MV in only 3.7 meters, resulting in an extreme compact cavity which represents a major advantage concerning the operation in a clinical environment. A view of the cavity is shown in Fig.2.6: the top half shell, in the third and fourth section, two movable plungers can be moved inside the cavity in order to change the distribution of the electric field all along the machine and to control the resonance frequency.

The effect of those plungers is shown by Fig.2.7 where two measurements of the

Frequency [MHz]	216.816
Input Energy [AMeV]	0.4 AMeV
Output Energy [AMeV]	7
Transv. Acceptance (norm) [mm mrad]	1
Longit. Acceptance [AkeV ns]	2.0
No. Of gaps	56
Effective Shunt Impedance [MΩ/m]	150
Q-Value	15000
RF Power [kW]	775
Transv. Dimension [mm]	260 x 344
Length [m]	3.76

Table 2.1: The main parameters of the HIT Injector linac.

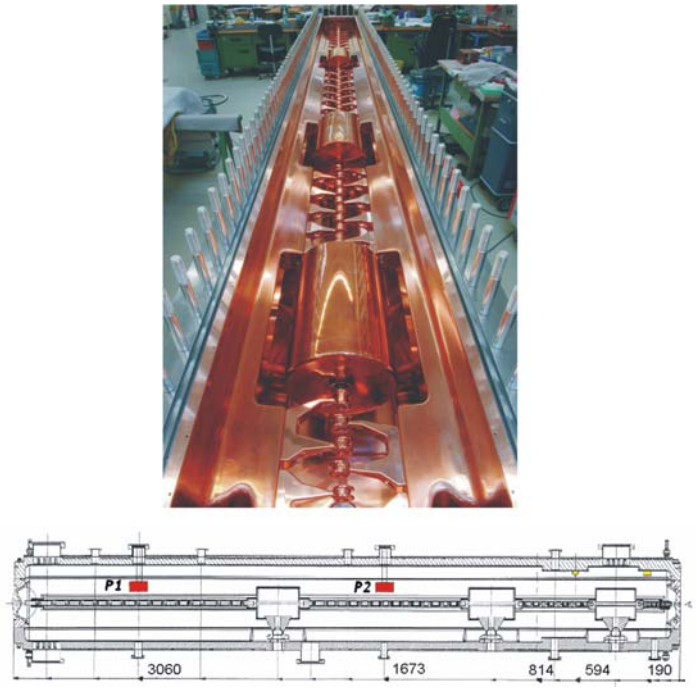

Figure 2.6: On top the IH for cancer therapy, and bottom the location of the movable plunger tuners.

phase signal (proportional to the square of the electric field, cfr Sect 2.5.1) with different plunger positions can be observed: on the left those mobile tuners were complete out, and on the right they were set on the optimum position for the field distribution. Finally, Fig.2.8 shows a comparison between the expected voltage along the cavity and the measured values: the agreement is within 1% in all sections which is well within the requirements of beam transport along the cavity [38].

This injector is the latest IH designed and built by the Frankfurt University and represents a major step in the development of such a cavity. The choice to use a single strucuture for such a wide energy range has represented a major challenge in terms of cavity design, development and final tuning. In a clinical enviroment, which requires an extremely reliable long-time operation and where all the possible sources of mistakes

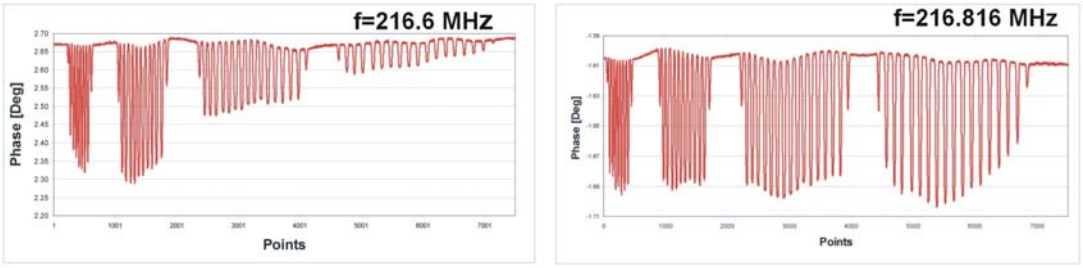

Figure 2.7: The effect of the mobile plungers on the field distribution: the signal shown is proportional to the square root of the axial electric field.

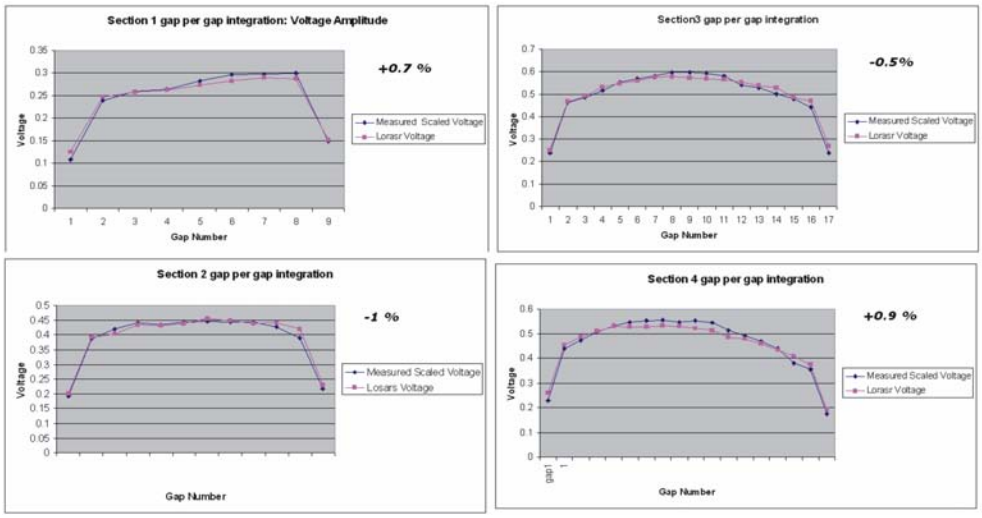

Figure 2.8: A comparison between the expected voltage distribution and the measured values.

must be minimized, the solution based on a single cavity presents many major advantages when compared to other solutions based on two or more modules. The RF equipment is simplified, any possible mismatch between the modules is avoided and, finally, there is only one cavity to be controlled. These are the reasons why such a solution has been chosen for the Heidelberg cancer therapy facility, adopted by the Centro Nazionale di Adroterapia in Italy and, at the moment, it is proposed in other planned facilities too.

2.3 Motivation for the CH-DTL

For frequencies higher than 250 MHz the dimensions of the IH are too small making a realistic design of such a cavity very difficult in terms of mechanical construction, maintenance and, for those reasons, the IH-DTL cannot be employed in that frequency range as a multicell structure. At the frequency of 325 MHz one should consider the higher H-modes, H_{n11} (with $n = 2, 3, 4$), which are exited by the structure followed in Fig.2.9.

According to the Faraday law, an increase of the number of stems results in a higher magnetic flux integral across the cavity which corresponds to a decrease of the shunt impedance; it is then natural to choose the H_{211} mode which with respect to the higher mode solutions is also much simpler to be built. The cross sectional geometry of the

Figure 2.9: The potential H-Mode structure. The number m of stems per drift is responsible for the resonant mode H_{m11}.

CH-DTL allows the design of multicell structure up to some GHz (as recently proposed in [39]) in the energy range from 3 to 150 AMeV while for lower energies the capacitive load between the stems drastically reduces the RF efficiency when compared with the IH-alternatives.

These reasons justify the choice to base the new FAIR proton injector on the CH-DTL and to propose it for other projects which require a highly efficient linac: at the moment, besides GSI, Fermilab will use such a structure as part of its new proton booster [20] and other international projects like IFMIF [40] and EUROTRANS [41] are considering it as a valid alternative to the Alvarez structure in the low-medium β range.

Even if theoretical results are extremely encouraging, room temperature CH-cavities have not been built so far and there was still a lack of experience in the construction technique: for this reason it was decided to build a first test model in order to test all fabrication steps and to find out technical solutions in terms of mechanical stability, tolerancies, coolong and copper plating. The experience gained in the construction of this first CH tank has been then transferred to the construction of the second resonator of the FAIR proton injector which is presented in the last section of this chapter.

2.4 Development of the CH-DTL

In order to improve the technical experience on such a new cavity, a model made of 8 gaps with a period $\beta\lambda/2$ of 45 mm was built [42]; this corresponds to a total inner length of 600 mm which is approximately the total length of the first tank of the GSI proton injector. To reduce the budget an existing stainless steel cylinder of 332 mm inner diameter was employed. Even if with this radius it was not possible to match exactly the resonance frequency of the proton injector the aim of this model was to test all the fabrication steps and to find out technical solutions in order to show the feasibility of cross-bar cavities with respect to mechanical construction, copper plating and cooling capabilities.

2.4.1 Early Design Phase

In a first step the geometry was optimized to get the highest shunt impedance: the shape of the stems was based on the existing IH cavities and adapted to the cross bar geometry. Two examples of those early geometries are shown in Fig.2.10 while in Fig.2.11 a technical design of the high energy side is presented.

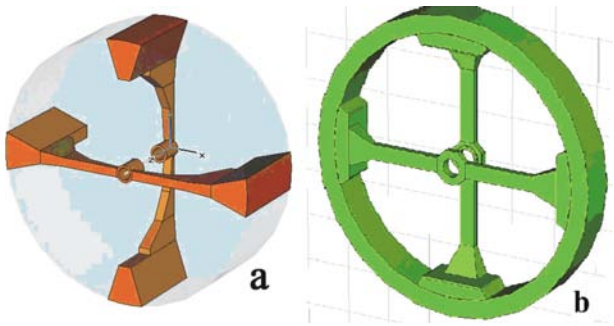

Figure 2.10: On the left side the first design of the proton injector: on the right, a version with simplified water cooled stem (note the central ring around the drift tube).

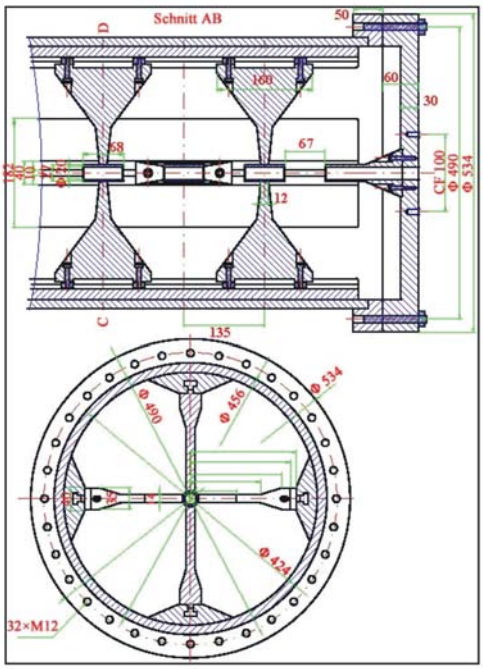

Figure 2.11: A technical drawing showing the early design of the high energy side of the Proton Linac.

Since the beginning it was decided to build the outer tank and the stems in stainless steel and then to copper plate the whole structure at the GSI galvanic workshop. There are several motivations for this choice with respect to a bulk copper model: at first, the mechanical stress on copper stems tends to become very fast unbearable as the tank's radius increases with energy and, on the other side the large and successfull experience in copper plating at GSI could be used resulting in a considerable materials cost saving.

With respect to this first proposed design, the geometry of the cavity has been modified in order to optimise the cooling capabilities of the stems and to reduce the potential misalignment of the drift tubes. Finally, optimised end half drif tubes have been developed to approximate the 'zero' mode. After several consultings with mechanical engineers the girder, which had to be used as cooling channel, was eliminated from the design: in fact, welding this long bar on the outer cylinder would have certainly distorted the external structure.

For this reason, completely new solutions have been adopted: the stems enter directly the outer cylinder and they are welded from inside. All stems are hollow and connected to an individual water source to ensure optimal cooling all across the cavity. Finally, the outer cylinder is cooled down by four independent external pipes. Already from this short description, it emerges clearly one of the main features of this design: the number of screws inside the cavity is strongly reduced and they are used only to fix the end flanges reducing the overall RF losses inside the cavity.

2.4.2 The Stems

In H-Mode structures currents flow across the stems to the drift tubes in order to create the axial electric field needed for the particles acceleration, as explained by Fig.2.12.

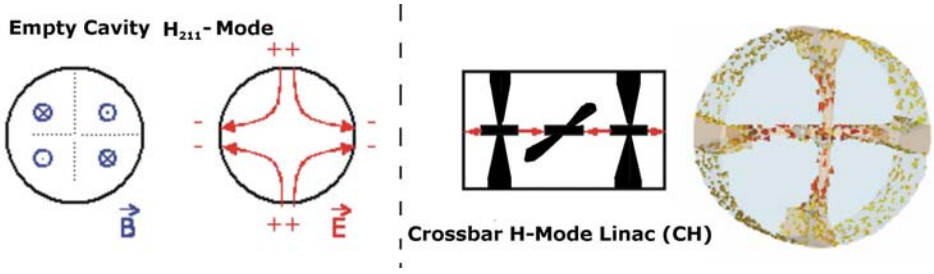

Figure 2.12: The $H_{21(0)}$ mode and its application on the CH-DTL. By orienting two neighboured stems at 90° one against the other the accelerating axial electric field is generated. The generated currents flow from one stem to the next across the outer cylinder.

From this picture it emerges clearly how the stems not only are responsible for the mechanical stability but they carry the highest current density of the whole structure: for this reason their design must be very robust and a water channel must be located inside them. On the other side, the stems should not be too large otherwise the shunt impedance would be reduced as a consequence of the higher capacitive load between each couple of stems. To take into account those necessities a conical geometry ending with 2 cylinders was adopted as shown in Fig.2.13.

There are several reasons which justify the choice of conical stems:

- A conical shape allows larger stem radius in the contact point with the outer cylinder, where the welding takes place: this ensure a higher mechanical stability.
- The contact line between the stems and the outer cylinder bears a strong current density and should be large enough to avoid overheating during RF operation.
- The reduction of the radius along the stems corresponds to a reduction in the mutual capacitance between each couple of stems avoiding a reduction in the efficiency of the machine.

Figure 2.13: Half stems geometry including the water cooling channel.

- The small neck on the contact point with the central ring is necessary to ensure good contacts and mechanical stability: this is especially true at low beta profile.
- With respect to any solutions involving profile steps, the copper plating becomes much easier for this design.

The production of the stems ended in spring 2005: after successful leak testing they were mounted in the cavity and welded into the outer stem, as shown from Fig.2.14 to Fig.2.16.

Figure 2.14: View of one stem together with the central rings: it is possible to see the aperture for the cooling water.

Unfortunately, the thickness of the central ring was not big enough and a small deformation was observed after the welding operations. This situation represents a

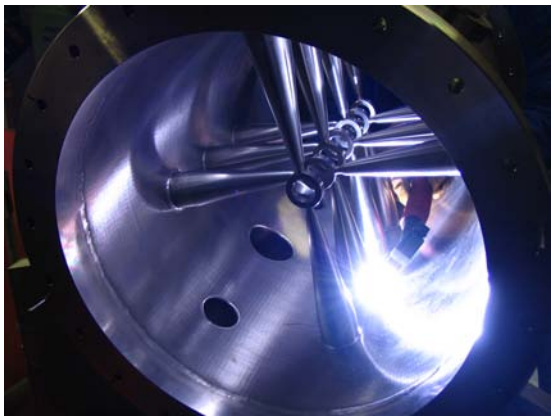

Figure 2.15: The welding of the stems into the outer cylinder.

Figure 2.16: The inner part of the cavity after welding.

serious problem with respect to the insertion of the drift tubes as explained in the next section.

2.4.3 The Drift Tubes

One of the main features of the H-structure is the possibility to locally tune the cavity: local gap voltage changes in the range ±20% can be achieved by varying the gap/period length ratio, as demonstrated in the tuning of the existing IH resonators. In order to apply this feature to the CH, the original idea was to use the so called 'Press Fit Technique': a bulk copper drift tube is cooled down inside liquid nitrogen and then inserted into the central ring of the stainless steel stem. The successive thermal extension would have created a strong contact between the drift tube and the stem: this idea was checked with the ANSYS code as shown in Fig.2.17.

Unfortunately, the stems deformation induced by the welding would result in a bad RF contact between the drift tubes and the stem. For this reason, it was decided to abort this idea and to test the cavity without the drift tubes. The effect of this choice on the RF parameters of the cavity will be explained later in this chapter. Nevertheless the aim of this model was to test all the fabrication steps: from this accident we learnt that the central ring of the stem must be very thick to bear the stress during the welding

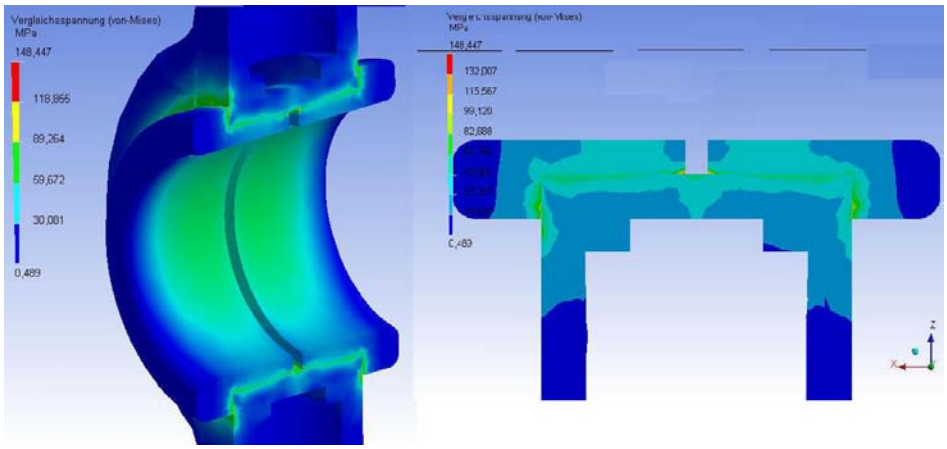

Figure 2.17: The drift tube mechanical stress resulting from press fitted half tubes as simulated with ANSYS.

operation. Anyway, in order to avoid such a situation, in future projects the drift tubes will be directly welded into the stems.

2.4.4 The Cooling System

If one one side the geometry of the CH is really suitable for an optimum cooling of the stems, on the other hand the high current flow on the surface of the enclosing walls makes necessary to the outer cylinder as well: since one cannot use and internal girder, a new solution has to be found. There are two feasible possibilities:

- 4 water pockets are mounted on the outer wall;
- a double walled outer cylinder is used.

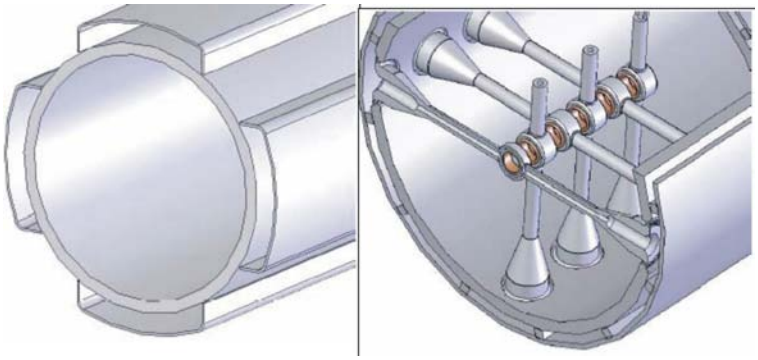

Figure 2.18: Two proposed solutions for the cooling system of the CH-DTL [43].

This last solution has the main advantage that the stems and the outer cylinder can be cooled by the same channel but, on the other side, it is much more complicated and expensive. The proposal to use external water pipes is very easy, cheap and doesn't require any further welding since the channel can be screwed on the top of the cavity. In this case each stem has its own water connection ensuring an optimal cooling system all

along the machine; for those reasons this solution was chosen and Fig.2.19 shows how the cooling system looks like in reality.

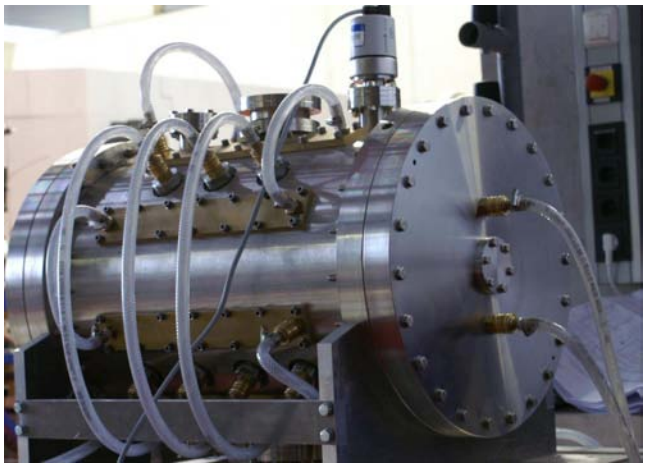

Figure 2.19: The CH-DTL and its cooling system.

Finally, to complete the design six flanges were located on the outer cylinder: we opted for 3 CF 63, one for the power incoupling, one for pumping and one as spare part, and 3 CF 35, two of them for the outcoupling loops and 1 to measure the vacuum pressure. The location of those flanches with respect to one row of stem is illustrated in Fig.2.20.

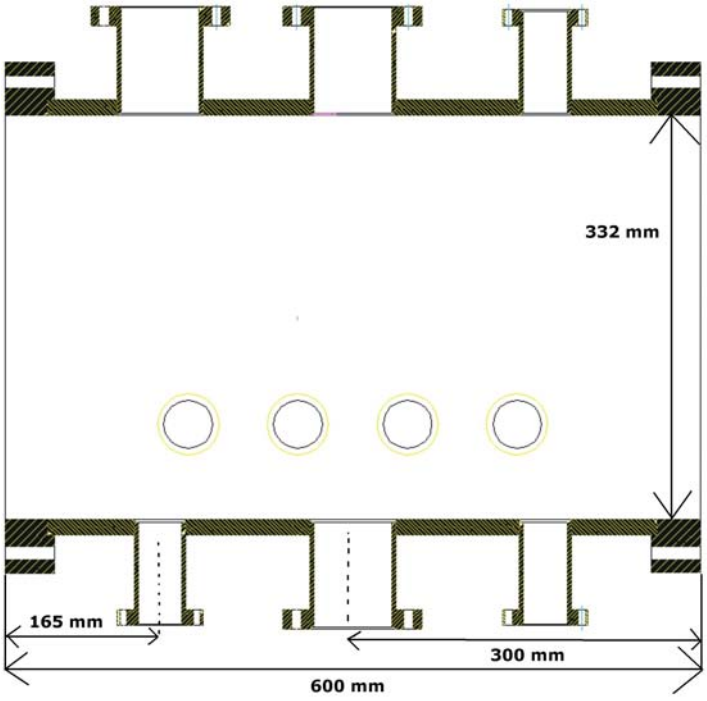

Figure 2.20: The flanges position.

2.4.5 The End Cells

Both IH and CH show naturally a cosine distribution of the electric field due their real resonant modes, respectively H_{111} and H_{211}: in order to approximate the 'zero mode' a tuning method has to be found.

In the IH, for instance, large undercuts are created in the girder at the cavity ends: the short circuit-action of the end walls with respect to H-modes is suppressed by that geometry if the undercuts are getting large enough.

In CH, as already explained in sect. 2.4.2, no girder can be located inside the cavity and the tuning should use a different strategy to decrease the resonant frequency at the cavity end. The most simple way is to lengthten the last half drift tube increasing in this way the volume of the end cell; besides this magnetic tuning, it is also possible to increase the radius of the last half drift tube inducing a strong capacitance with the closest stem: in this way, not only the end cells become resonant but, at the same time, they become large enough to host the magnetic element needed for beam focusing. In this way a very compact structure can be developed reducing the distance between adiacent tanks which helps the longitudinal beam dynamics since it profits a lot by a short distance between adiacent tanks. A scheme of the cavity is shown in Fig 2.21 where this concept becomes clear.

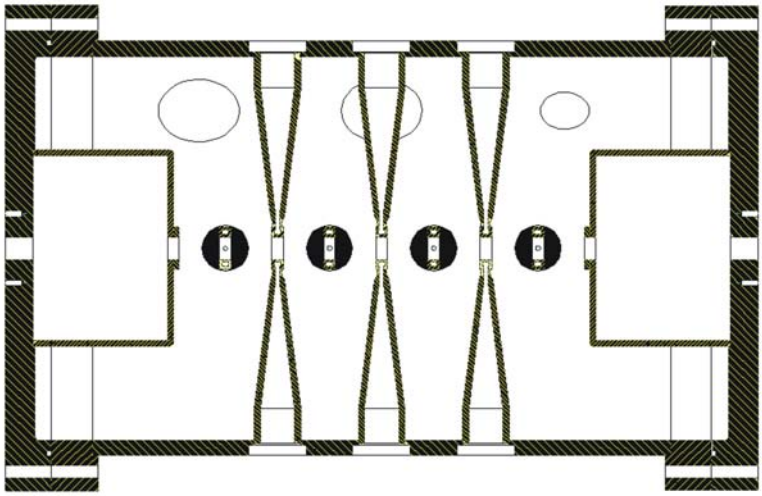

Figure 2.21: A cut of the cavity along the beam axis: the big end cells are used to approximate the 'zero mode' and, at the same time, they will host magnetic lenses and diagnostics devices.

In order to check the validity of this concept we studied the influence of the length of the half drift tubes on the RF parameters of the cavity. From Fig. 2.22 one can see how an increase of around 25 % in the electric field of the last cells can be achieved varying the length of the big drift tube approximating in such a way the 'zero mode'. In order not to exceed with the dimensions of the cavity it was decided to set the length at 120 mm. In Tab.2.2 one can see the dependency of the main RF parameters from this length. For all case a g/L of 0.5 was used and the copper conductivity was set to its ideal value

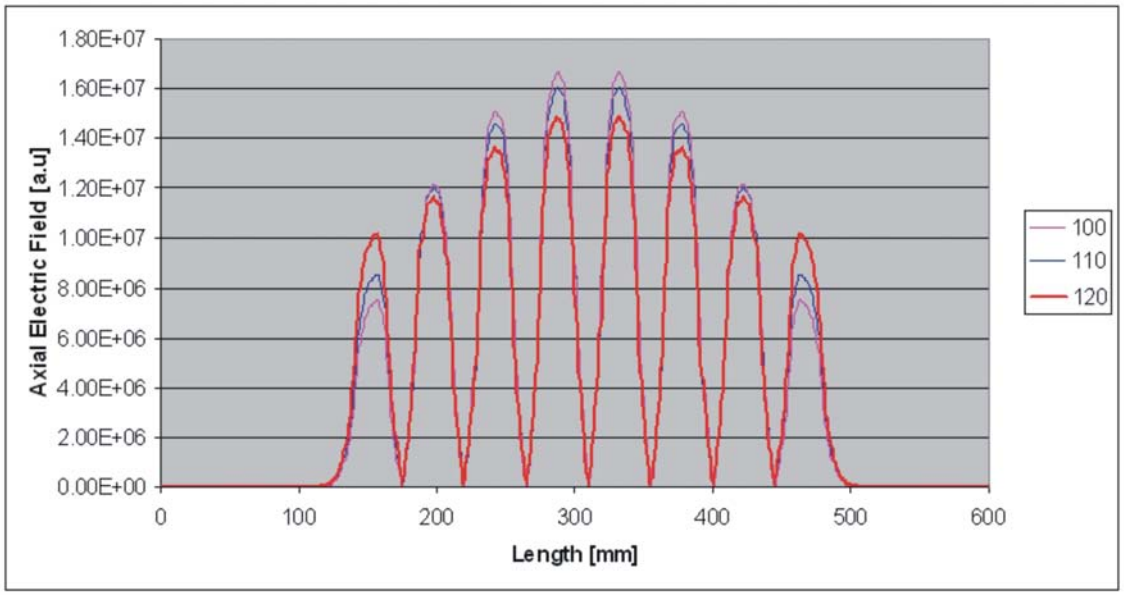

Figure 2.22: The axial electric field for different length of the big end drift tube: the g/L was set at 0.5 for all cases..

Length [mm]	Q_0	Frquency [MHz]	Loss [W]
80	12974	328.06	158900
100	13000	327.35	158200
110	13168	326.32	155700
120	13255	324.54	153845

Table 2.2: Dependency of the RF parameters from the length of the big end drift tube. A g/l ratio of 0.5 is assumed together with a stored energy inside the cavity of 1 J

2.4.6 RF Parameters

After fixing the geometry of the end cells the cavity was tuned changing the gap/length ratio all around the structure. The simulated frequency became 325.8 MHz with a Q_0-value of 13847. The axial field distribution is shown in Fig.2.23 and the effective shunt impedance is around $80M\Omega/m$, in good agreement with the simulation for the GSI Proton Injector. Finally, since it was decided to test the cavity without the drift tube inserts, this 'naked' version of the cavity was investigated: the main difference between the two versions is the capacitive load on the axis which is now strongly decreased: as a consequence the resulting frequency becames 338.7 MHz and Q-value decreased down to 13675. On the other side it is very interesting to observe the axial field distribution, shown in Fig. 2.24: the field distribution without any drift tube inserts is peacked at the cavity ends. This is due to the high capacitive load between the end cells and the last stems which concentrates the electric field at the ends of the cavity.

The decreas of shunt impedance can be easily understood since the absence of the drift tubes changes drastically the ratio between the cell length and the drift tube diameter from the designed value of 0.25 up to 0.31. This implies that the axial component of the electric field is much less strong than desidered leading to a reduction of the axial voltage and of the transit time factor.

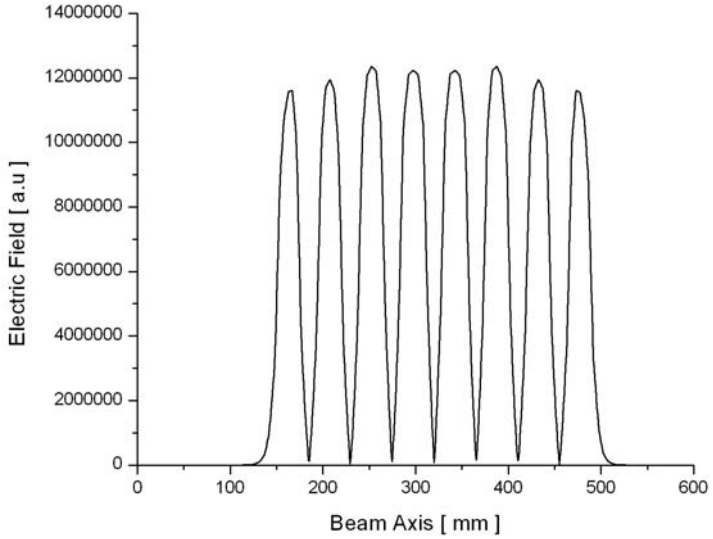

Figure 2.23: An example of tuned cavity.

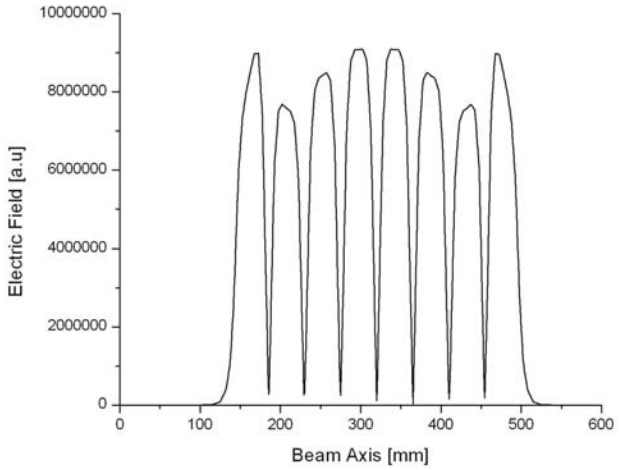

Figure 2.24: The field distribution without drift tubes inserts.

2.5 RF Measurements

2.5.1 The Resonant Perturbation Measurements Method

The most commom technique to measure the field distribution inside a linear accelerator is the perturbative method which consists in driving a perturbation body inside the cavity. The method, often referred as Bead Pull measurement method, is based on the McLean's theorem stating that, in case of adiabatic deformation, the product between the stored energy and the period time is a constant of motion, i.e.

$$W \cdot T = Const \tag{2.8}$$

Parameter	Model with D.T. inserts	Model without D.T. inserts
Frequency [MHz]	325.8	338.7
Q_0-Value	13847	13675
Shunt Impedance [MΩ/m]	144	128

Table 2.3: The effect of the drift tubes inserts on the RF parameters.

or, equivalently

$$\frac{dW}{W} = \frac{d\omega}{\omega} \tag{2.9}$$

If now one introduces into the cavity of volume v_2 a small perturbation body, (a ball of volume v_1 moving slowly along the axis of the cavity) this will result in a change of frequency and stored energy according to

$$\frac{dW}{W_0} = \frac{d\omega}{\omega} \tag{2.10}$$

where W_0 is the stored energy without the object and $\Delta W = W_0 - W$ is equal to

$$\Delta W = \int_0^{v_2} \frac{1}{2}\epsilon_0 E_u^2 dv - \int_{v_1}^{v_2} \epsilon_0 (E_u + E_{dip})^2 dv - \int_0^{v_1} \frac{1}{2}\epsilon_0 \epsilon_r E_i^2 dv \tag{2.11}$$

where E_u is the electric field without the perturbation body, E_{dip} is dipole field outside the polarised bead and E_i is the homogeneous field inside the bead. If the dimensions of the bead are much shorter than the wavelength of the resonance frequency we can assume the following relations:

$$E_i = \frac{3}{\epsilon_r + 2} E_u \tag{2.12}$$

$$E_{r,dip} = \frac{p \cos\theta}{2\pi\epsilon_0 r^3} \tag{2.13}$$

$$E_{\theta,dip} = \frac{p \sin\theta}{4\pi\epsilon_0 r^3} \tag{2.14}$$

$$p = dipole\ moment = 3v_1 \frac{\epsilon_r - 1}{\epsilon_r + 2} \epsilon_0 E_u \tag{2.15}$$

$$P = Polarisation = \epsilon_0 \frac{3(\epsilon_r - 1)}{\epsilon_r + 2} E_u \tag{2.16}$$

$$\tag{2.17}$$

Thanks to those relationships it is possible to demonstrate that the variation of energy inside the cavity can be written as

$$\Delta W \approx -\frac{1}{2} v_1 P E_u \tag{2.18}$$

which corresponds to the energy of a dipole into an homogeneous field E_u. Using the expression for the polarisation P and introducing the volume of the ball we get finally the variation of the electric energy inside the cavity:

$$\Delta W = -2\pi r^3 \epsilon_0 \frac{\epsilon_r - 1}{\epsilon_r + 2} E_u^2. \tag{2.19}$$

By the use of similar considerations for the variation of the stored magnetic energy one finally get the total variation of the electromagnetic energy inside the cavity:

$$\frac{\Delta W_{em}}{W_{em}} = \frac{\Delta\omega}{\omega} = -\frac{\pi r^3}{W_{em}}\left[\epsilon_0\frac{\epsilon_r - 1}{\epsilon_r + 2}E_u^2 + \mu_0\frac{\mu_r - 1}{\mu_r + 2}H_u^2\right]. \tag{2.20}$$

If the perturbation body is made by metal ($\epsilon_r \to \infty$, $\mu_r \to 0$) one gets

$$\frac{\Delta\omega}{\omega} = -\frac{\pi r^3}{U_{em}}\left[\epsilon_0 E_u^2 - \mu_0\frac{1}{2}H_u^2\right] \tag{2.21}$$

For H-mode linacs the contribution of the magnetic field can be neglected when measuring on the beam axis unless at the cavity ends where a small portion of the magnetic field can be presented in the gaps.

If our resonator is connected with a power generator we can rewrite $W = QP/\omega$ and then use the phase response

$$\Delta\phi = 2Q\frac{\Delta\omega}{\omega} = -\frac{\omega E^2}{P}2\pi r^3\epsilon_0 \tag{2.22}$$

from which we can easily evaluate the electric field scaled by the power:

$$\frac{E}{\sqrt{P}} = \sqrt{\frac{-\Delta\phi}{\omega 2\pi r^3\epsilon_0}} \tag{2.23}$$

2.5.2 Experimental Results

After copper plating the cavity was ready for the RF measurements which were aimed to experimentally verify the main RF parameters, such as the operating resonance frequency, the distance with other modes, the Q_0 value and the field distribution.

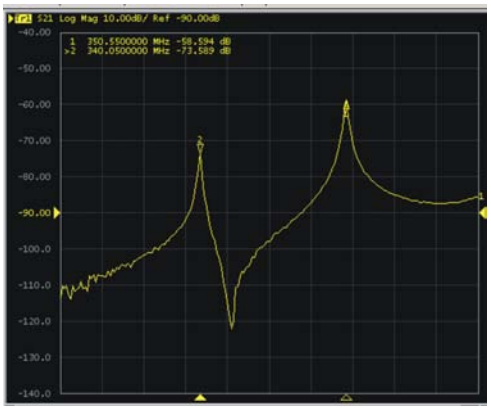

Figure 2.25: The frequency spectrum of the CH test model showing the frequency of the first two resonant modes.

Fig.2.25 shows the frequency spectrum of the first resonating modes, the operational one occuring at 340.03 MHz and the closest one at 350.51 MHz. This large distance ensures a robust operation especially when compared with Alvarez DTL. Tab.2.4 shows a comparison between the expected values, simulated with Microwave Studio, and the experimental results for the first four modes: as one can see the agreement is really

Mode	Expected Frequqncy [MHz]	Measured Frequency [MHz]	Relative error [%]
1	338.7	340.03	0.3
2	347.91	350.51	0.7
3	361.22	363	0.4
4	409.00	408.85	0.03

Table 2.4: The measured frequencies compared with the simulated values.

satisfactoty showing an error of 0.3 % in the determination of the operating resonance mode.

The agreement between simulations and measurements extens as well to the measure of the Q-value: the measured Q-value of 13000 is around 95 % of the expected value which was calculated assuming the ideal conductivity of copper. It is very important to remark such a goog agreement since MWS tends to overestimate this parameter by 10-20 %, typically. This is due to the presence of screws and contact in the cavities which results in a higher level of electrical losses. At this point the advantages of the construction concept used for this CH-model becomes obvious: welding the stems into the outer cylinder results in fact in a considerable reduction of screws which are used only to fix the end flanges to the cavity. In this way we get rid of a possible source of RF losses increasing the capabilities of the structure.

Concerning the voltage distribution the result is plotted in Fig.2.26 where the comparison between voltage and measurements is shown: as one can see from this picture the measurements reproduce rather well the behaviour of the voltage distribution. The small disagreement can be explained observing that the deformation induced by the welding makes it extremely difficult to perfom a precise measurement on the axial electric field.

Nevertheless the measurements reproduce very well the trend of the electric field which is peacked at the cavity ends due to the lack of the insert drift tubes.

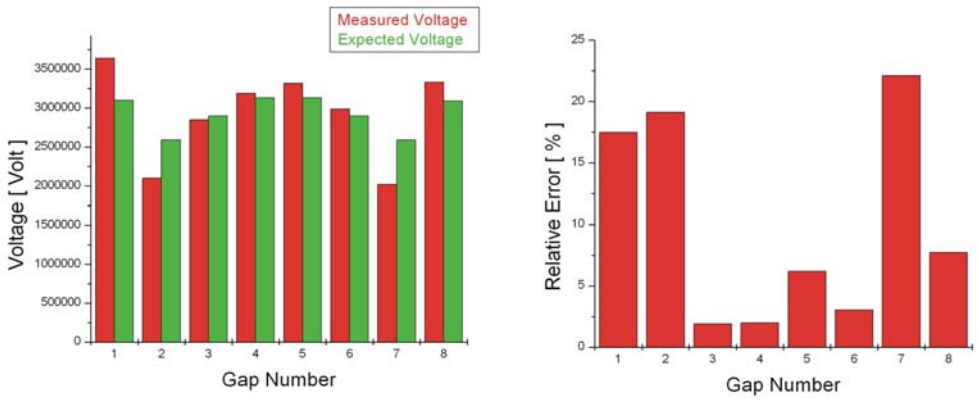

Figure 2.26: A comparison between the measured voltage along the cavity and the simulated one.

Finally, to test the capabilities of the cooling system, the cavity was connected to the 2 kW cw amplifier available at IAP: the experimental setup is shown in Fig.2.27

In a first step the cavity was tested up to 1 kW, corresponding to a total voltage inside the cavity of $\sim$ 220 kV: this level was achieved very fast, around 20 minutes, and

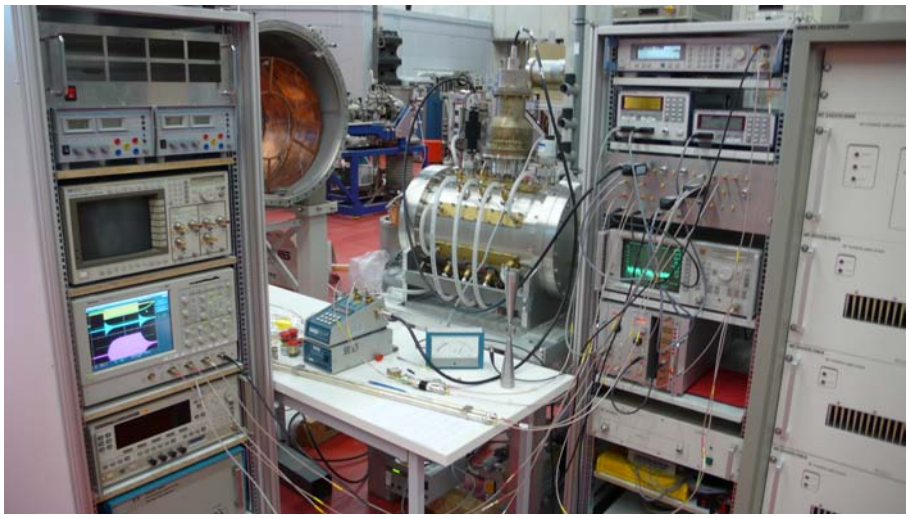

Figure 2.27: The experimental setup for the 2 kW cw test.

no significant multipacting was observed. This phenomenon happened only once and disappeared just after few seconds. The temperature on the outer cylinder was extremely stable showing the efficiency of the cooling system. Finally, the cavity was brought to 2 kW (corresponding to $\sim$ 304 kV inside the cavity) without any need of conditional time; again, no significant shift of the cavity frequency was observed confirming the capability of the designed cooling system.

Those results proof the capabilities of the room temperature CH-DTL both in terms of mechanical construction as well as in terms of copper plating and RF properties.

2.6 The Coupled CH: the CCH-DTL

As explained in the first chapter the GSI proton injector will be fed by 6 klystons at 2.5 MW: this large availability of power pushes in the direction of coupled structures in order to match the linac with such a high availability of power. This section, after a brief explanation of the coupling theory, describes in details the solutions and the strategy adopted to develop a linac based on coupled CH structure, the fist example of a coupled H-Mode linac.

2.6.1 The problem of three coupled oscillators

In order to get inside the physics of coupled accelerating structure one can investigate a simple case made by a central resonator with mutual inductance on both sides to couple with two end oscillators, as described in Fig.2.28: the end oscillators present the same inductance L_0 of the central one but twice the value of capacitance in order to have the same resonance frequency.

The Kirckhoff law applied to such a scheme leads to a system of three coupled equation

$$x_0 \left(1 - \frac{\omega_0^2}{\Omega^2}\right) + x_1 k \quad = \quad 0 \tag{2.24}$$

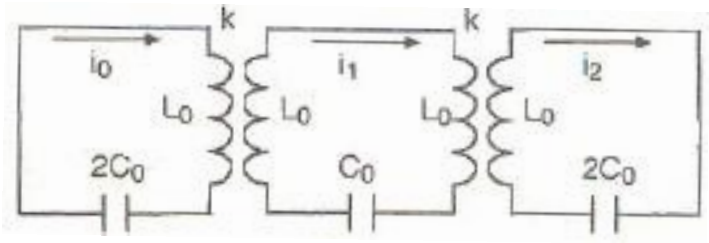

Figure 2.28: Three magnetically coupled oscillators [44].

$$x_1\left(1-\frac{\omega_0^2}{\Omega^2}\right)+(x_0+x_2)\frac{k}{2} = 0 \tag{2.25}$$

$$x_2\left(1-\frac{\omega_0^2}{\Omega^2}\right)+x_1 k = 0 \tag{2.26}$$

where $x_n = i_n\sqrt{2L_0}$ are the normalised currents, $k = M/L_0$ is the coupling constant, ω_0 is the resonant frequency of the uncoupled elements and Ω is the resonant frequency of a steady state oscillation, the so called normal mode.

By defining the matrix operator L, as

$$L = \begin{pmatrix} 1/\omega_0^2 & k/\omega_0^2 & 0 \\ k/2\omega_0^2 & 1/\omega_0^2 & k/2\omega_0^2 \\ 0 & k/\omega_0^2 & 1/\omega_0^2 \end{pmatrix} \tag{2.27}$$

the system can be put into a matix form

$$LX_q = \frac{1}{\Omega_q^2}X_q \tag{2.28}$$

where

$$X_q = \begin{pmatrix} x_0 \\ x_1 \\ x_2 \end{pmatrix} \tag{2.29}$$

is the eigenvector and Ω_q^2 is the relative eigenvalue frequency. There are three possible solutions

- The 'zero mode' where all the oscillators have zero relative phase difference

$$\Omega_0 = \frac{\omega_0}{\sqrt{1+k}} \quad X_0 = \begin{bmatrix} 1 \\ 1 \\ 1 \end{bmatrix} \tag{2.30}$$

- the $\pi/2$ mode with an unexited resonator,

$$\Omega_1 = \omega_0 \quad X_1 = \begin{bmatrix} 1 \\ 0 \\ -1 \end{bmatrix} \tag{2.31}$$

- the π mode with the highest resonant frequency

$$\Omega_2 = \frac{\omega_0}{\sqrt{1-k}} \quad X_2 = \begin{bmatrix} 1 \\ -1 \\ 1 \end{bmatrix} \tag{2.32}$$

The bandwidth is defined as the frequency difference between the highest and the lowest normal mode frequency, i.e $\delta\omega = \omega_0 k$

2.6.2 Coupling of CH-DTL's

The starting point to develope a coupling between two resonators of the CH type is the role of the electromagnetic lens which has to be placed between the resonators to ensure the beam focusing. A possible solution is to place the lens outside the tank and to add a coupling port to transfer the RF wave from one resonator to the other: this would lead to a scheme similar to the CCDTL explained in Sect.1.4.3 (cfr. Fig.1.19). The other possibility is to develop a concept based on a coupling section which includes the triplet: in this way the construction results to be much easier and efficent.

A possible application of this concept is shown in Fig.2.29 which illustrates the RF current flow that would create the desired coupling. The RF current on the lens outer cynder is oriented parallel along the beam axis while the closest stems of the CH resonators present opposite charge status resulting in a coupling cell of lens $N \cdot \beta\lambda$.

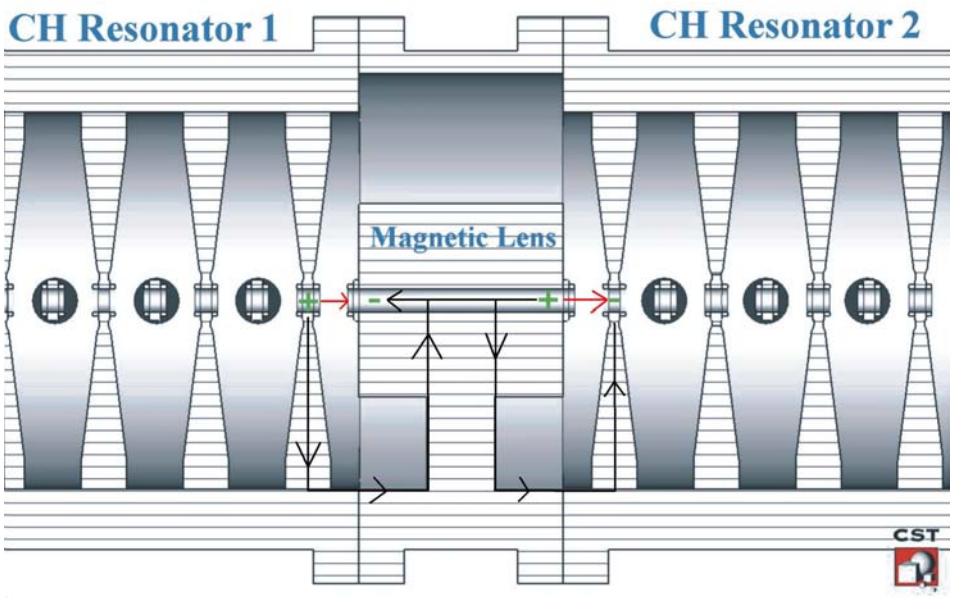

Figure 2.29: The coupled scheme between two CH resonators: the illustrated current flow creates a 0-Mode coupling.

To understand how to concretize this concept, one can start from the end cell geometry described in Sect.2.4.5; the analysis of the magnetic flux in the end cells shows how the magnetic field surrounds the last half drift tubes emulating the field distribution of a cavity exited in E_{010} mode (Fig.2.30).

If one suppose to put together two CH-DTL of that type and to replace the endwalls by a radial support for the lens, the result in terms of magnetic flux will be the one

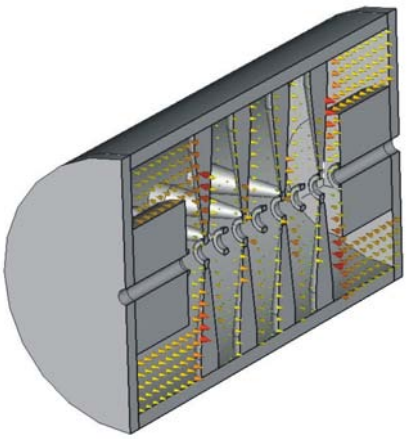

Figure 2.30: The magnetic field on the cavity's middle plane: one can see how the magnetic field surrounds the end half drift tubes.

desribed in Fig. 2.31, where the magnetic field runs parallel and antiparallalel to beam axis in the accelerator modules to then surrounds the focusing elements as it is in the classical DTL's exited by the E_{010} Mode: this corresponds exactly to an RF current on the outer cylinder of the lens which is oriented parallel to the beam axis.

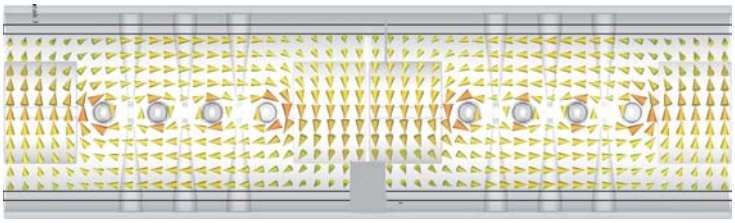

Figure 2.31: The magnetic field distribution at half radius of a system made by 2 CH resonators where the inner walls are replaced by a simple radial support for the lens place between the cavities.

Finally, the radius of the intertank section has to be adjust in order to matach the resonance frequency of the accelerating structure as shown in Fig.2.32.

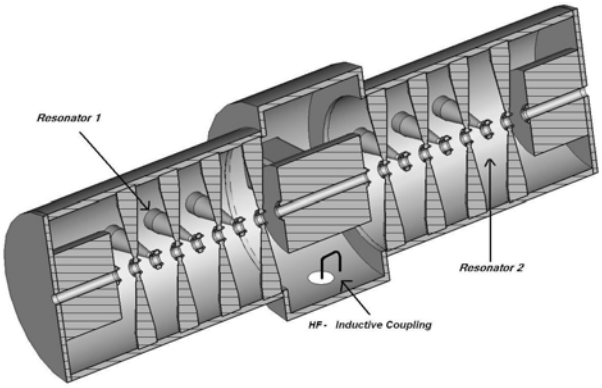

Figure 2.32: The coupled CH-DTL.

The result is a compact structutr where two H_{211} resonators are magnetically coupled

by an intertank section which oscillates in the E_{010} Mode: the magnetic field generated by the incoupling loop placed in the middle of the intertank section penetrates in both resonators exiting them in the TEM mode.

This solution presents many advantages with respect any solution based on slots and aperture which could have been adopted by the Side Coupled Linac: the construction is very simple, requiring only the insertion of the magnetic lens inside the coupling element and the module can be easily opened to perform any kind of maintenance. Moreover, there is a large experience with this kind of tube installation inside IH cavities [45].

The capabilities of such a solution in terms of RF properties were tested with Microwave Studio by simulating the coupling between two resonators which are identical to the test model described in the previuous section (including the drift tubes): the particles synchronisation between each module requires a distance of $n \cdot \beta\lambda$ between the centers of the last gaps with n integer and set to 5 for our partcular case. First, the effect of the radius of the intertank section was investigated and then an example of a tuned cavity is presented.

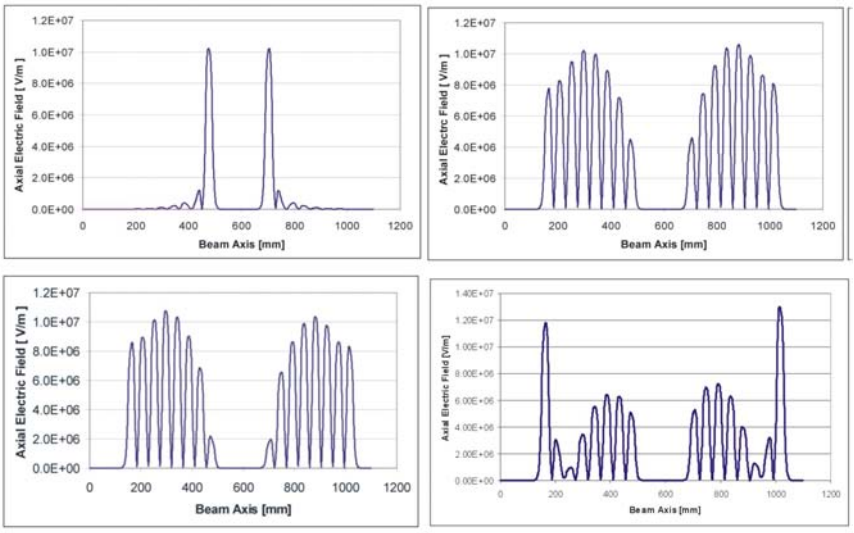

Figure 2.33: The field distribution of the first three resonating modes for the cavity used to test the coupling concept.

Fig.2.33 shows the field distribution of the first four resonating modes for an intertank cavity radius of 180 mm against 166 mm internal radius of the CH resonators: the resonance frequencies are 160.1, 327.5, 328.45 and 346.63 MHz, respectively. The first mode is the non coupled mode where only the intertank section is resonating while the fourth mode clearly belongs to the next harmonic, the H_{212}. For this reason attention must be focused only to the second and third modes which are the only coupled modes of this configuration.

The second mode, the 0 mode, is characterised by the oscillation in the E_{010} mode of the coupling cell: the current on the lens outer cylinder oscillates longitudinally since the lens ends are at different potential and the magnetic field is responsible for the coupling with the CH resonators as explained in the previous section: a detail of the magnetic field in the middle plane of the cavity is shown in Fig.2.34 while in Fig.2.35 the magnetic flux is shown at half of the radius of the CH resonators.

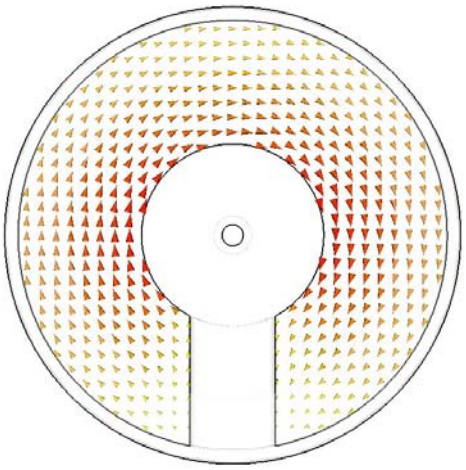

Figure 2.34: The magnetic field distribution on the middle plane of the cavity, showing how the intertank section resonates in the E_{010} mode.

The third mode is, according to the explanation of the previous section, the $\pi/2$ mode which can be considered as the longitudinal H_{211} mode where the magnetic field lines have the same orientation along the whole structure: under this resonance mode the cavity can be considered as a single CH resonator with an internal lens: it is interesting to note how the intertank section is not strongly resonating as one can see from the field distribution shown in Fig.2.32 showing a weak electric field in the coupling gaps. This is a very important feature of the coupling scheme since it gives a natural hint where the structure must be coupled with the power supply. If the incoupling is in fact placed in the intertanks section the parasite mode could be only weakly exited avoiding the risk of an overlapping between those two neibourgh modes.

In order to avoid such on overlap between the neighbour modes one can also modify the radius of the intertank section, assuming, like in our case, that the radius of the CH cavities in fixed. Fig.2.36 shows the dependency of the resonating frequency for different radii of the intertank section: we can observe how the $\pi/2$ mode is not influenced by such a parameter while the coupled mode shrinks in frequency as the radius increases, thus enhancing the coupling between the resonators since the coupling constant is basically determined by the frequency difference between those 2 modes. It is also important to observe how this result is in agreement with the theoretical description of the magnetic coupling presented in the previous section.

The radius of the coupling cell plays also a major role in the field and voltage distribution along the whole structure as shown in Fig.2.37: as the radius increases, the electric field becomes flatter along the axis since the electric field between the CH's and the coupling cell gets stronger. This is a very important feature of such a coupling scheme: just by changing the radius of the coupling cell one can increase the coupling factor without changing the relative height of the electric field in the accelerating modules. A final tuning can be performed by changing the gap/cell-length ratio as shown in Fig.2.38 where an example of a rather flat distribution with an intertank radius of 220 mm is shown.

Finally, the sensitivity to the radius of the accelerating modules was simulating by

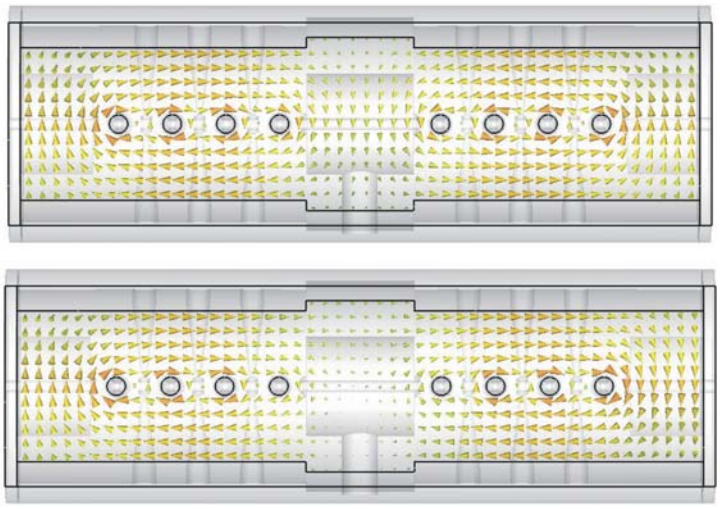

Figure 2.35: A comparison between the magnetic fluxes at half the CH's radius for the two neighbours modes. The $\pi/2$ mode (bottom), higher in frequency, is charachterised by a weak exitation of the intertank section. This allows to hinder the RF coupling with that mode during operation if the incoupling loop is placed in this section.

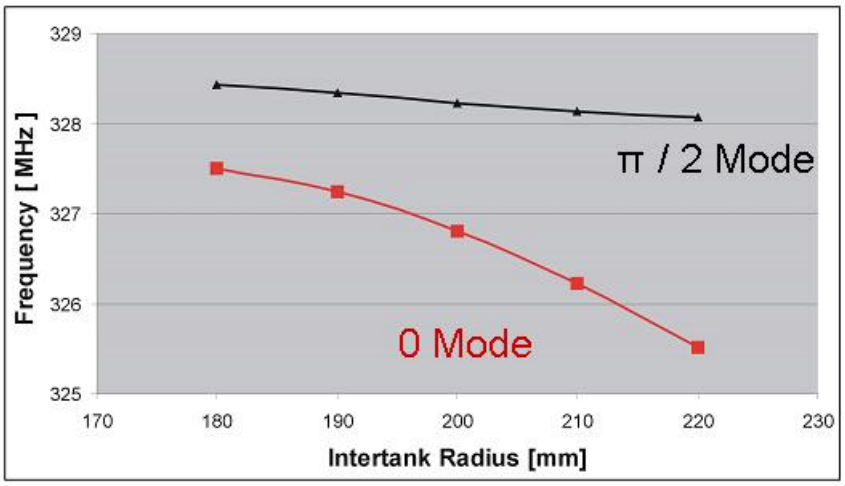

Figure 2.36: The frequency of the coupled modes as a function of the intertank radius.

increasing the diameter of the second cavity by 1 mm and then by increasing of $\pm$ 1 mm the radius of both cavities.

As one can see from Fig.2.39 the cavity is rather sensitive to the variation of the outer cylinder in a single cavity: the mistake of 1 mm results in a bad distribution of the electric field which was strongly reduced in the first cavity. The change of the radius influences the frequency as well which drops to 324 MHz against the tuned case of 325.4 MHz.

Finally, if both radii suffer from the same variation, the field tends to remain balanced and only in the gaps close the coupling cell it starts to drop down.

This situation suggests the idea to include in any real model a mobile tuner (of the

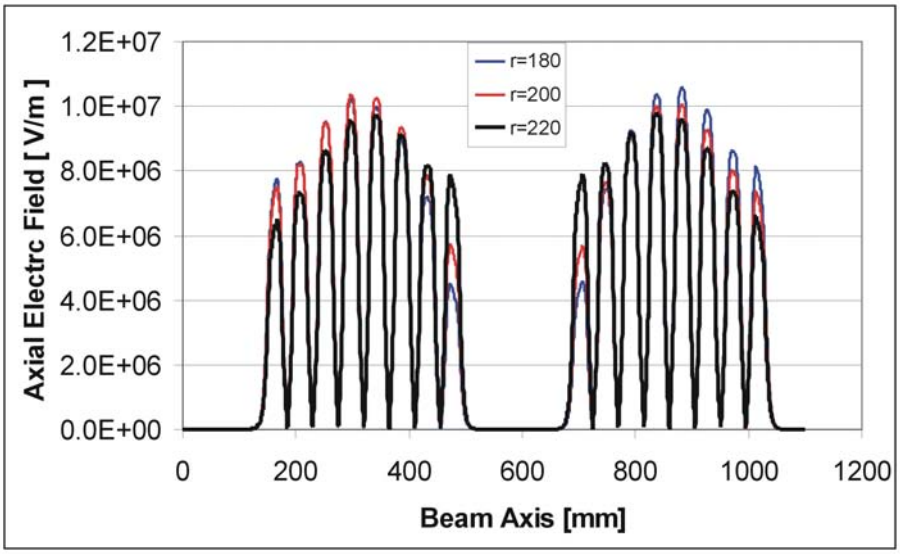

Figure 2.37: The field distribution of the operating mode as a function of the intertank section.

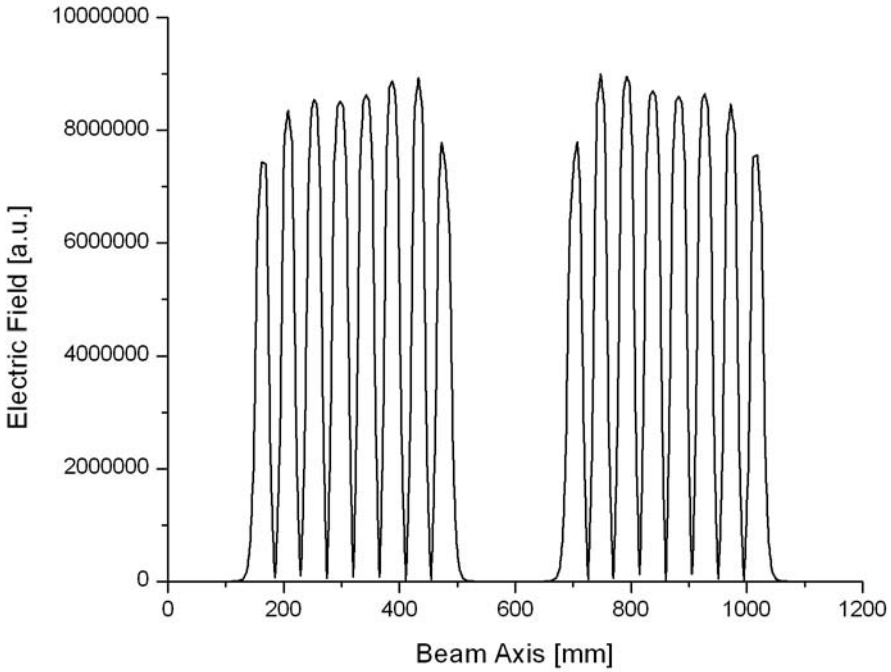

Figure 2.38: An example of rather flat field distribution for the test simulation model.

same type described in Section 2.1.3) which can be used to correct the field distribution and to control the resonance frequency.

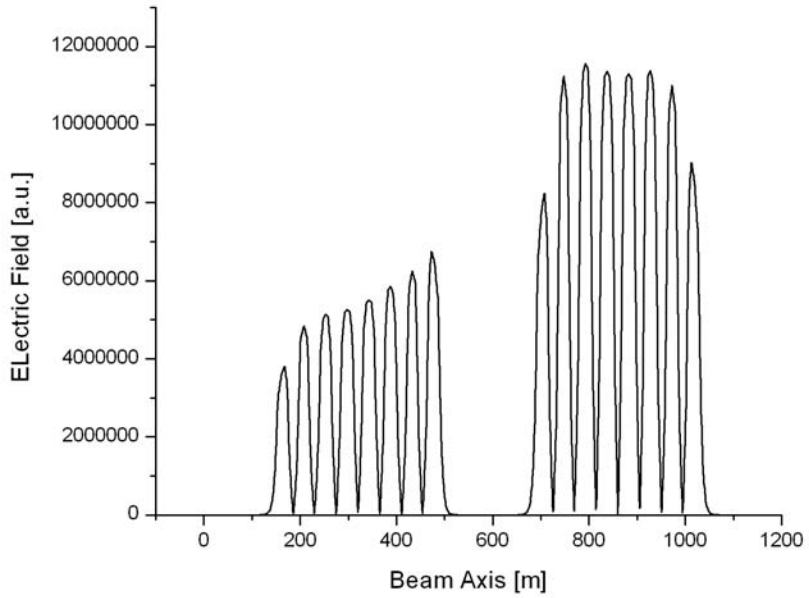

Figure 2.39: The field distribution when one cavity is increased by 1 mm in radius.

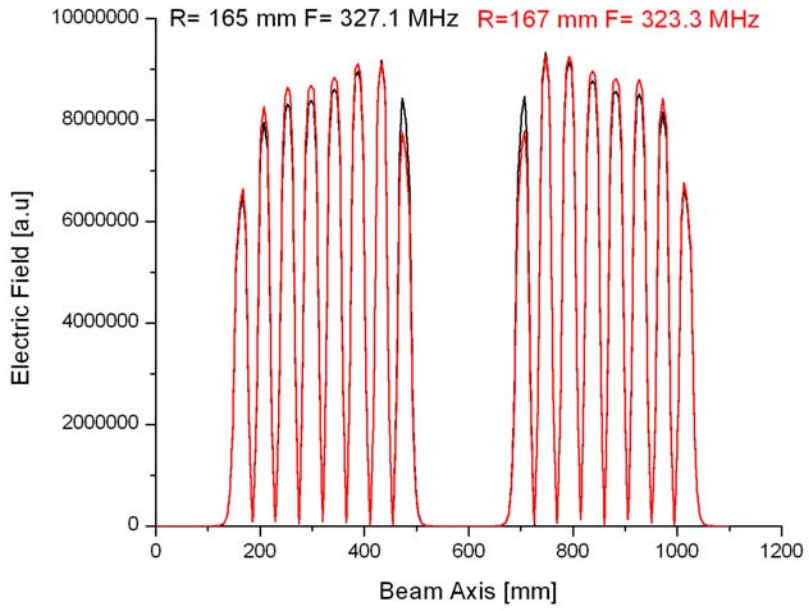

Figure 2.40: The field distribution when both cavities suffer from a mistake of ±1 mm in radius.

2.7 The Second Resonator of the Proton Injector

To definitely proof this innovative coupling concept, it was decided to investigate the second resonator of the GSI Proton Injector, i.e. the coupled third and fourth CH sections: the choice to analyze the second module, and not for example the first one, is dictated by the fact that the final design of the RFQ is, at the moment, still not fixed. In this way still some degrees of freedom are left in order to potentially change the first module whose only the initial and final energy are fixed at the moment.

In a first step, the LORASR code was employed to design the main parameters such as the number of gaps, the voltage, the tubes length and the transit time factor. Finally, Microwave Studio was employed to optimize the geometry and to tune the field distribution inside the cavity.

This three meter long cavity consists of 29 gaps in total, 13 in the first CH resonator and 14 in the second one: as explained in the previous section the coupling is ensured by an intertank section housing the magnetic triplet needed for the beam focusing.

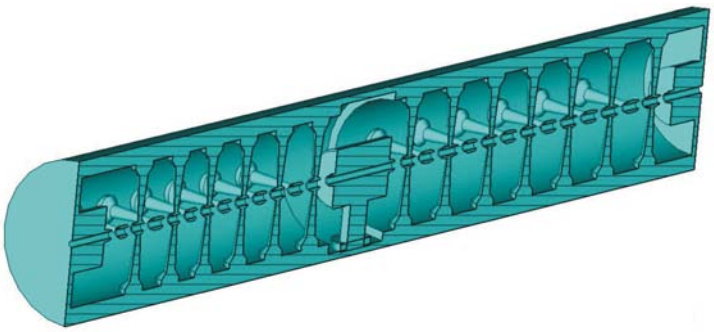

Figure 2.41: The second resonator of the GSI proton injector.

The first resonator has a length of 1.18 meters for an inner diameter of 184.5 mm: it holds a total voltage of 7.2 MV with an average effective gradient of 6.4 MV/m. The second resonator is longer, 1.45 meter with a larger inner diameter of 189 mm: the applied voltage of 7.2 MV corresponds to an average effective gradient of 5.8 MV/m. The coupling cell has a diameter of 214 mm and hosts the 24 cm long lens; the distance between the center of the last gap of the first CH and the centre of the first gap of the second one is 2 $\beta\lambda$ calculated at the transit energy of 17.4 MeV. The end cells are shaped with the large half drift tube presented in Sect.2.4.5. the length of this tube is 120 mm in the first tank and 180 mm in the last one. Fig.2.42 shows the dimension of all the components of this coupled module.

The applied effective voltage is shown in Fig.2.43 together with the transit time factors as calculated by LORASR: these parameters were employed to calculate the lenth of the drift tubes in order to obtain an homogeneous electric field on the axis which is expected to have a peack value on the axis around 12 MV/m. Tab.2.5 summerizes the cell geometries all along the coupled structure.

The geometry of the stem, shown in Fig.2.44 was optimized following the criteria presented in Section 2.4.3: a conical shape was chosen in order to reduce the capacitance between each couple of stems, between the stems and the drift tubes and to provide mechanical robustness. In order to keep the construction simpler the stem shape remains

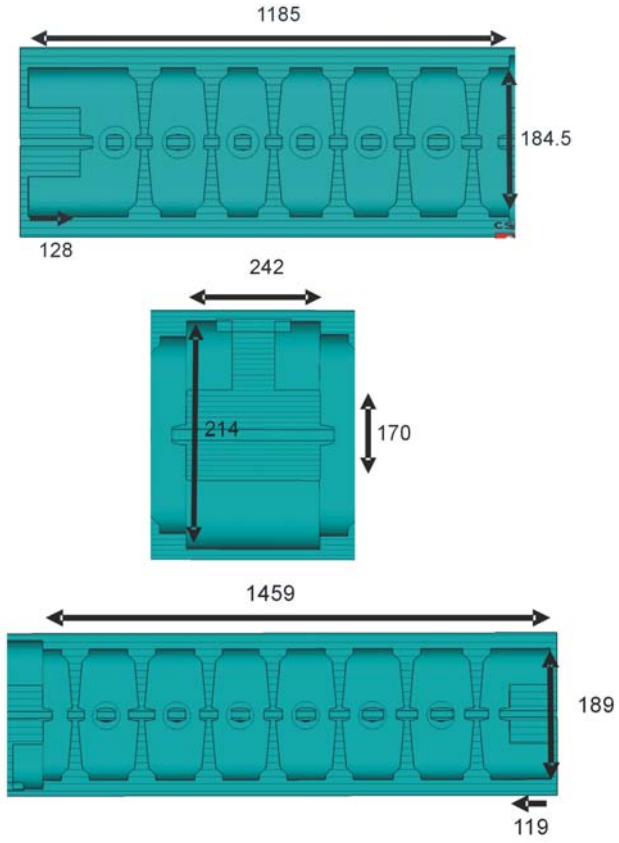

Figure 2.42: The dimensions of the second module of the GSI proton injector.

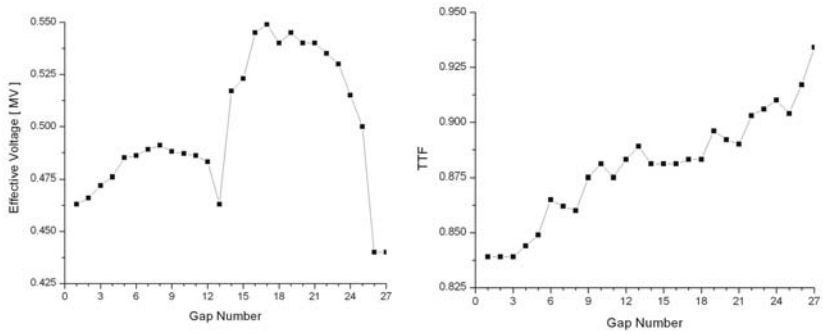

Figure 2.43: On the left the effective voltage and, on the right the transit time factors as calculated by LORASR.

unchanged in both modules as well as the ratio between the inner and the outer diameter of the drift tubes which is fixed at 1.3 all along the structure. Finally, a corona (18 mm in radius) surrounds the tubes in order to provide mechanical stability during the welding operations and to leave enough space for the water channel.

Fig.2.45 shows the electric field distribution in the cavity middle plane: as one can see from this picture, the electric field is strongly concentrated on the axis and the capacicy

Gap No.	Gap Length [mm]	Tube Length [mm]	Voltage [kV]	TTF
TANK 3				
1	35.6	37.3	552	0.839
2	36.2	37.8	555	0.839
3	35.7	55.1	563	0.839
4	36.3	39.0	564	0.883
5	34.9	40.8	571	0.844
6	35.7	42.5	562	0.849
7	36.5	43.0	567	0.865
8	34.9	44.8	571	0.862
9	34.6	47	558	0.860
10	36	47.7	553	0.875
11	35.1	48.7	555	0.881
12	34.6	50.6	547	0.875
13	37	308.1	521	0.883
TANK 4				
14	37.5	51.4	587	0.889
15	37.7	52	594	0.881
16	37.9	75.4	619	0.881
17	37.6	52.2	622	0.881
18	38.1	54.0	614	0.883
19	36.	55.4	608	0.883
20	37.8	55.7	605	0.896
21	38.5	57.6	607	0.892
22	36.3	60.1	592	0.89
23	35.8	61.8	585	0.903
24	35.3	62.5	565	0.906
25	36.7	64.2	555	0.91
26	34	68.4	480	0.904
27	30.3		471	0.917

Table 2.5: The cell structure of the second coupled module of the GSI Proton Injector.

between the stems and the drift tubes is strongly reduced by the chosen geometry.

The field distribution calculated with MWS is plotted in Fig.2.46, while Fig.2.47 shows the corresponding voltage distribution compared with the reference values as calculated by LORASR. As one can see from this picture the field distribution is rather balanced between each section and there is a satisfactory agreemtent with the voltage distributions.

Finally, the parasite mode which occurs at 326.5 MHZ, was investigated. The distance of 1.3 MHz from the operating mode ensures a safety margin in operation since the bandwith of the klystron is 750 kHz. As one can see from Fig.2.48 this mode presents a reduced exitation of the coupling cell resulting in a very weak oscillation of the coupling gaps. In this way, by feeding the structure in the middle of the intertank section, the

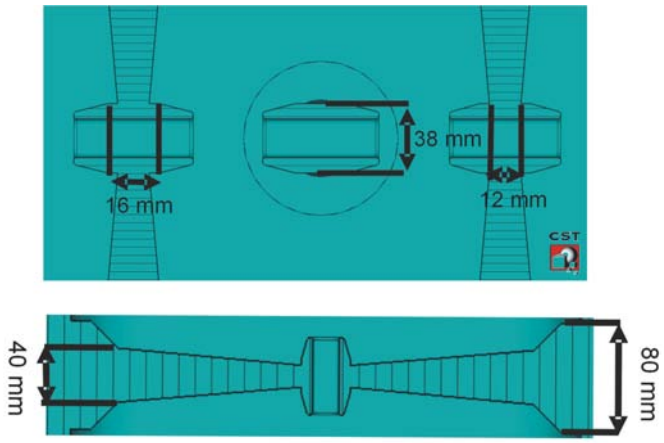

Figure 2.44: The stem geometry of the second resonator of the GSI proton injector.

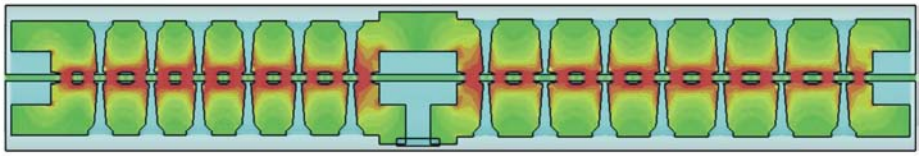

Figure 2.45: The electric field distribution on the cavity middle plane.

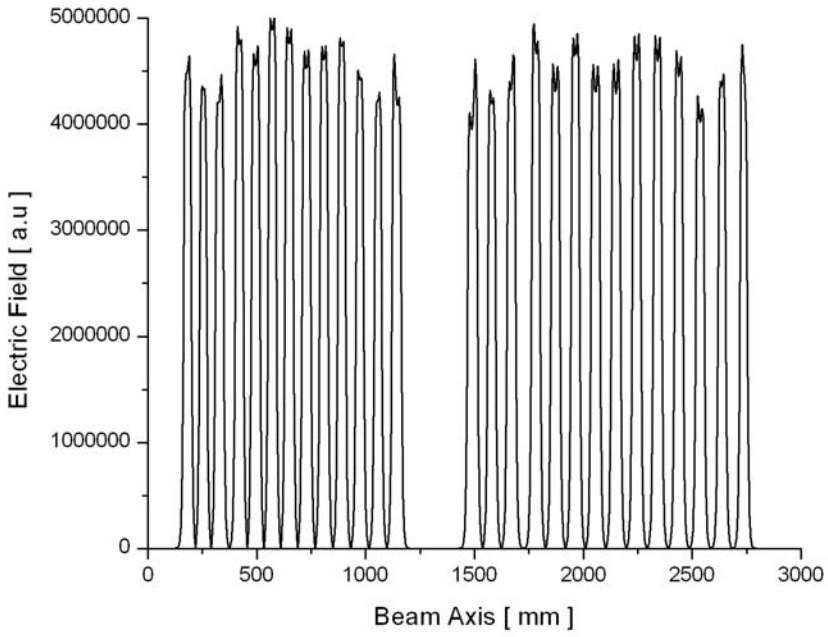

Figure 2.46: The electric field distribution as calculated by MWS.

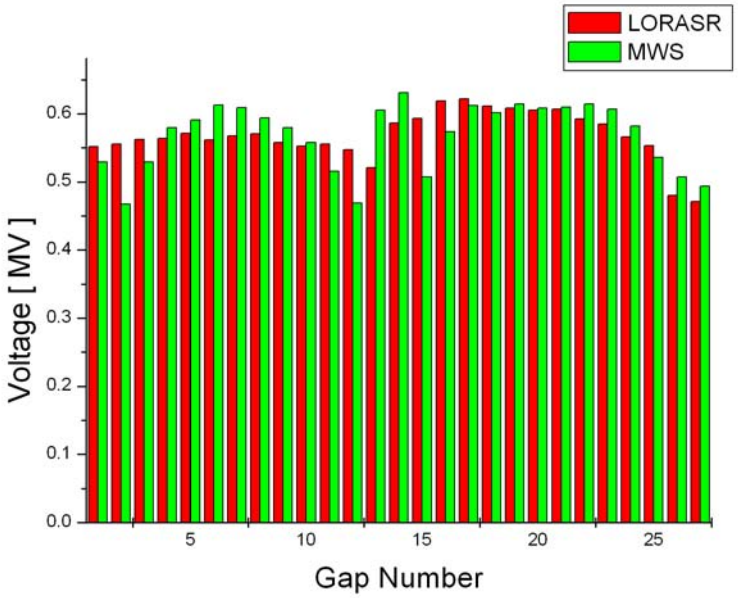

Figure 2.47: A comparison between the voltage distributions as calculated by Microwave Studio and as designed by LORASR.

RF drive of this mode could be souppressed.

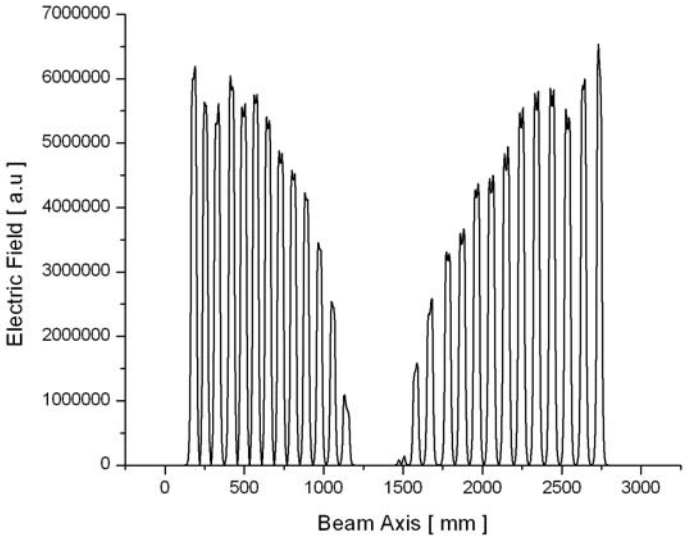

Figure 2.48: The electric field distribution of the first parasite mode.

This concept becomes clear observing the magnetic field distribution in the middle plane of the cavity for the operating and for the parasite mode: as one can see from Fig.2.49 the magnetic field in the intertank section is three orders of magnitude lower than in the operational mode.

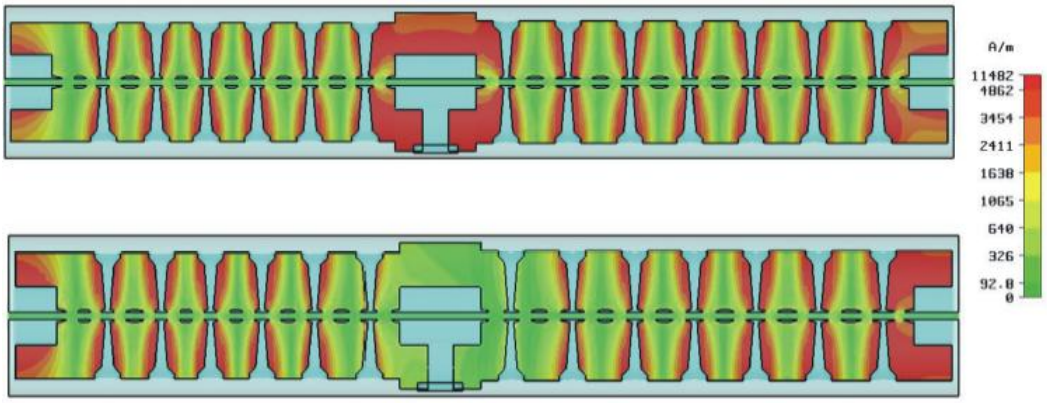

Figure 2.49: The magnetic field on the cavity middle plane for the 0 and for the $\pi/2$ mode.

Finally, the main features of such a long resonator are listed in Tab.2.6 which shows the expected values calulated by MWS and LORASR codes.

No. of gaps	27 (13+14)
Frequency [MHz]	325.2
Energy range [MeV]	11.7-24.3
beam loading [MW]	882.6
Heat Loss [MW]	1.35
Total Power [MW]	2.2
Q_0-Value	15300
Effective Shunt Impedance [MΩ/m]	60
Average E_0T [MV/m]	6.4 - 5.8
Kilpatrick	2.0
Coupling Constant [%]	0.3
No. of Plungers	5 (2+3)
Beam Aperture [mm]	20
Internal Total Length [mm]	2896

Table 2.6: The main parameters of the second resonator of the GSI proton injector.

2.7.1 Scaled 1:2 Model

Even if the simulations performed with MWS result to be really promising, the complexity of such a resonator requires a deeper investigation that only an experimental campain can ensure: for this reason a 1:2 scaled model has been built to test the main RF parameters such as resonance frequency, Q_0-value, shunt impedance and field distribution.

Fig.2.50 shows some details of the cavity: as explained in Sect.2.6.2. the coupling between both resonators is rather sensitive to the radius of each single CH: for this reason it was decided to equip the cavity with mobile plungers (15 mm in radius) which can be used to modify the field distributions and to drive the resonance frequency towards the desidered value. The first section contains 2 couples of plungers which are mounted at $\pm 45°$ whith respect to the stems axis while the second section has been equipped with other three couples. One more plunger is located in the coupling cell at 90° with respect to the lens support.

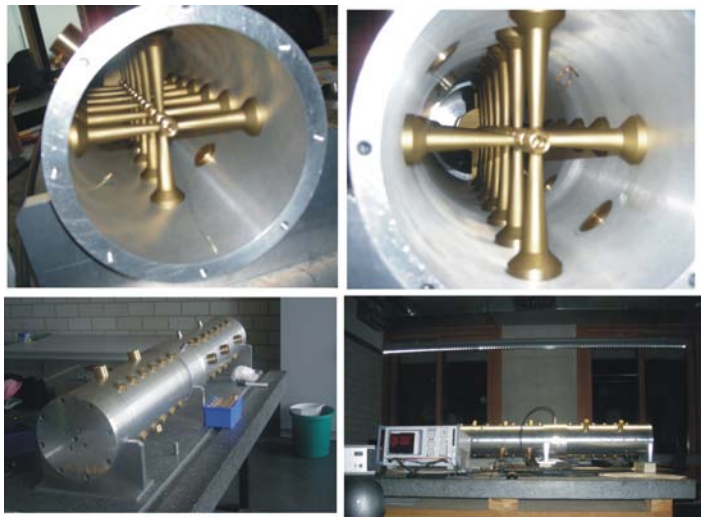

Figure 2.50: On top, two details of the cavity; bottom two photos of the closed cavity on the test bench.

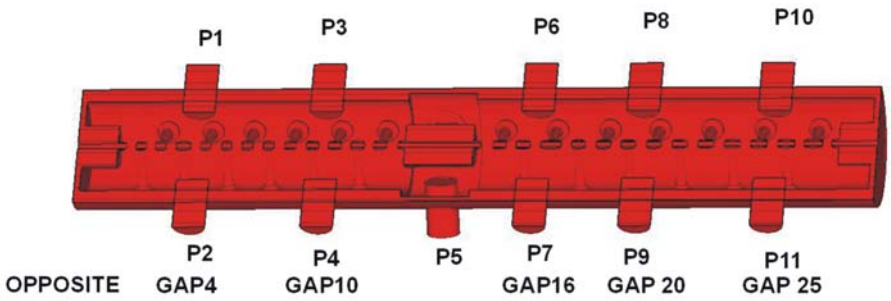

Figure 2.51: A longitudinal cut of the cavity showing the plunger positions.

With respect to the original design the tube lengths were slithly modified: Tab.2.7 shows difference between the original design and the mounted drift tubes inside the cavity

No. of tube	Length (designed) [mm]	Length (modified) [mm]
5	20	19.75
6	20.4	19.25
7	21.25	20.2
8	21.5	20.7
9	22.4	21.5
10	22.0	20.82
11	23.35	23.675

Table 2.7: The changes in the drift tube lenght between the simulated model and the real one.

The result of the first measurement is illustrated in Fig.2.52 and 2.53: the first cavity presents an overvoltage in the low energy end with a lack of voltage from gap 8 to 10; on the other side, the second resonator presents a lack of voltage at the high energy end. The resonance frequency spectrum is in good agreement with the silulations: the 0 mode resonates at 652.64 MHz, the $\pi/2$ mode occurs at 653.98 MHz, while the H_{212} mode resonates at 658 MHz. The Q_0-value for the 0 mode results to be around 3500 and doesn't depend on the plungers position.

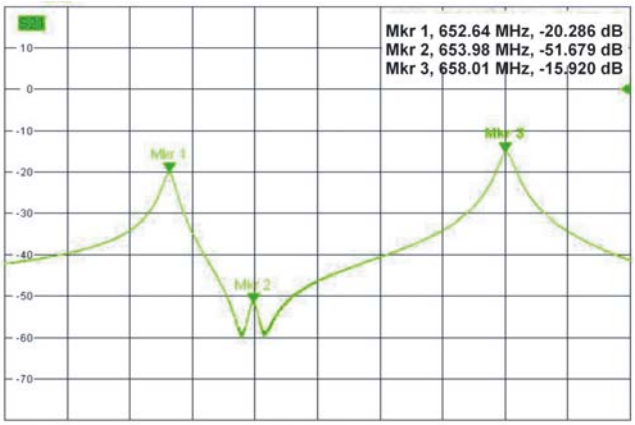

Figure 2.52: The frequency spectrum of the first distribution.

These results show a good agreement with the simulated value: the error in the resonance frequency of the 0 mode is 0.3 % while the $\pi/2$ is weakly exited as expected: to improve the field distribution, in a first step the gap length has been again modified and finally several plunger position were investigated to study the effect on the frequency spectrum and on the field distribution.

After the modification of the drift tubes in the first CH resonators, several configurations for the plunger positions were analized. Finally, the first couple of plunger were set 15 mm inside the cavity, the third plunger 8 mm leaving out its opposite, and, in the second resonator, only plungers number 6 and 7 were set 5 mm inside the cavity. With this configuration the effect of the plunger located in the coupling cell was investigated.

Tab.2.9 shows the effect of the plunger located in the coupling cell with respect to resonance frequency: as one can see it acts inductevily increasing the resonance

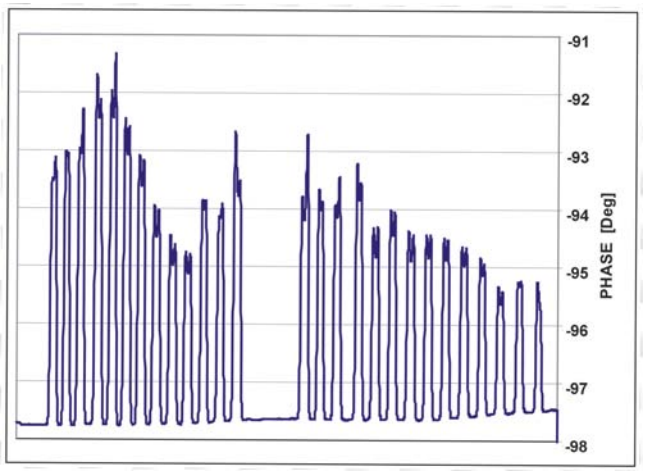

Figure 2.53: The phase distribution of the first measurements.

No. of tube	Length (designed) [mm]	Length (modified) [mm]
8	21.5	21.12
9	22.4	22.4
10	22.0	21.75
11	23.35	23.925

Table 2.8: The changes in the drift tube lenght after the first measurement.

frequency of the 0 mode while it doesn' effect the resonance frequency of the $\pi/2$ mode but it reduces more and more its amplitude. When the plunger is completely inside the cavity the parasite mode vanishes: this is an extremely important effect which can be used to get rid of this mode during operation.

This result is of PARAMOUNTAL importance: the main problem of all coupled cavities is the distance between the desidered operating mode and the parasites one as described in Sect.2.6.1: in our design this problem can be solved looking for a plunger configuration which results is a good field distribution and kills the closest parasite mode as well.

P5 [mm]	Freq. 0 Mode [MHz]	Frequ. $\pi/2$ Mode [MHz]
0	653.0	654.5
10	653.03	654.5
20	653.206	654.5
30	653.28	654.5
40	653.31	654.5
50	653.41	654.5
60	653.51	vanished

Table 2.9: The effect of the plunger located in the coupling cell.

The opposite effect was observed inserting all the other plungers inside the CH resonators: when those plungers are inside the cavity the strength of the $\pi/2$mode tends to encrease while the resonance frequency of the 0 mode increases. This means that the plungers can only act inductively.

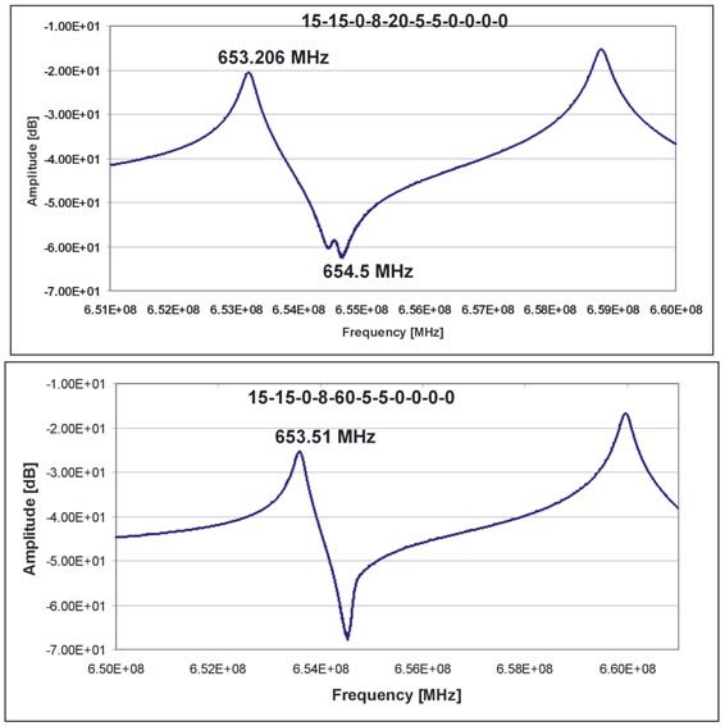

Figure 2.54: The The effect of the plunger located in the coupling cell. The $\pi/2$ mode decrease increasing the depth of the plunger inside the cavity until it vanishes completely.

Concerning the field distribution the central plunger modifies the strength of the coupling gaps: this is well explained in the following examples which shows the field and voltage distributions for two positions of the central plungers, 20 and 40 mm respectively. As one can see both from the electric field and voltage distribution (Fig.2.55 and 2.56), the main effect of the central plunger is to reduce the voltage inside the coupling gaps. From this plots we can observe another interesting effect: the field distribution in both resonators presents a light undervoltage in the gaps close to the coupling cells which, instead, are strongly resonating. This can be explained considering the typical cosinus profile of the field for an H-mode cavity which results in a lower voltage at the cavity end: in our structure, the 'zero mode' is then obtained on one side by use of the large half end drift tube and, on the other, by the coupling cell which oscillates in the classical E_{010} mode.

This latter case represents a promising results and, for this reason, a detail summary is presented in Tab.2.10

Finally, from Eq.2.23 it is possible to evaluate the shunt impedance Z as

$$Z = \left[[\int_0^l \sqrt{\frac{-\Delta\phi}{2\pi\omega r^3 \epsilon_0}}] \right]^2 \cdot \frac{1}{l}. \tag{2.33}$$

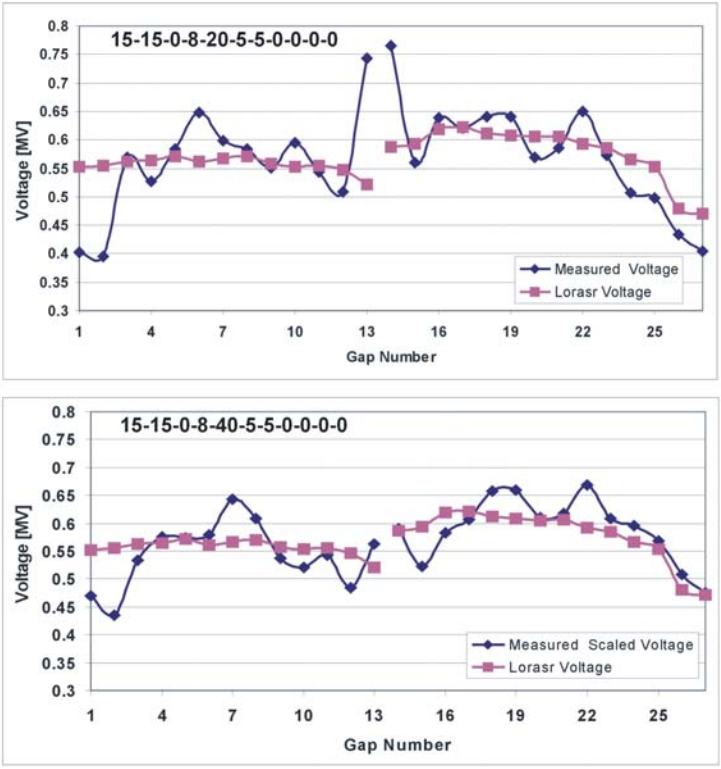

Figure 2.55: A comparison between the measured voltage distribution and the expectation values for two different positions of the plunger in the coupling cell, 20 and 40 mm, respectively.

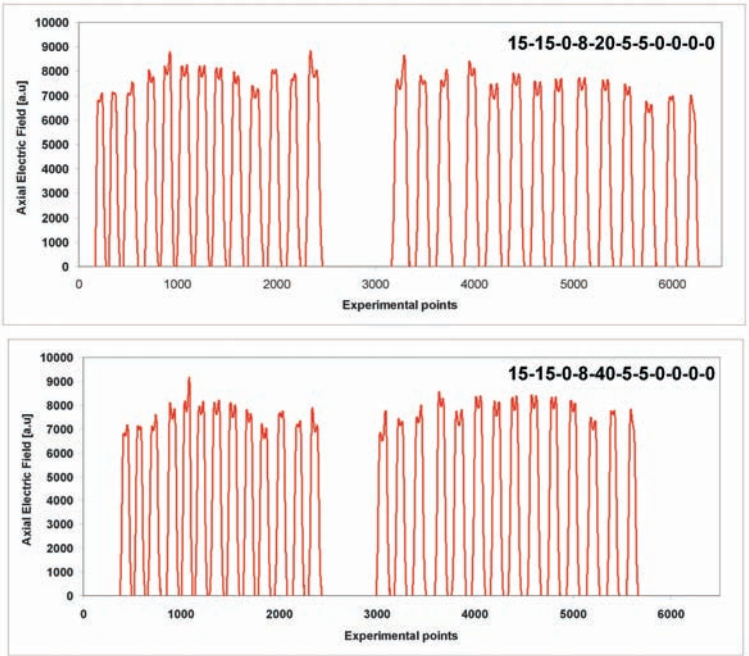

Figure 2.56: A comparison between the measured voltage distribution and the expected values for two different positions of the plunger in the coupling cell, 20 and 40 mm, respectively.

Gap No.	LORASR VOLTAGE [MV]	Measured Voltage [kV]	Relative Error [%]
TANK 3			
1	552	470	-14.82
2	555	434	-21.71
3	563	533	-5.10
4	564	575	1.99
5	571	573	0.45
6	562	579	3.17
7	567	642	13.34
8	571	608	6.61
9	558	537	-3.71
10	553	521	-5.70
11	555	542	-2.25
12	547	484	-11.43
13	521	562	8.02
TANK 4			
14	587	589	0.44
15	594	521	-12.08
16	619	583	-5.66
17	622	606	2.52
18	614	657	7.44
19	608	660	8.53
20	605	610	0.80
21	607	618	1.91
22	592	669	12.94
23	585	608	4.09
24	565	595	5.16
25	555	568	2.78
26	480	508	5.93
27	471	474	0.79

Table 2.10: The experimental result for the voltage distribution with the central plunger 40 mm down in the cavity

which for this case results to be 107.85 $M\Omega/m$. Since the shunt impedace scales as the square root of the resonance frequency this value would correspond to 75.62 $M\Omega/m$ for a 325 MHz module, in good agreement with the simulated value 80.1 $M\Omega/m$ ($\sim 5\%$ error).

2.8 The superconducting CH

Several future projects like EUROTRANS, IFMIF, and RIA require high duty cycles or even cw operation. Superconducting solutions seem to be favourable above a certain duty cycle because of higher reliability and lower operational costs when compared to

room temperature linacs. If energy variability is not an issue as in driver accelerators with a fixed velocity profile it is advantageous to use multi-cell cavities which can increase the real estate gradient significantly while the total number of cavities with their support systems is reduced significantly. Although many types of superconducting cavities have been developed in the past there was still a lack of efficient cavities in the low energy regime whereas efficient means a large energy gain per cavity. The development of efficient superconducting DTL front ends with high real estate gradients have motivated the design, construction and test of the superconducting CH-structure [46]

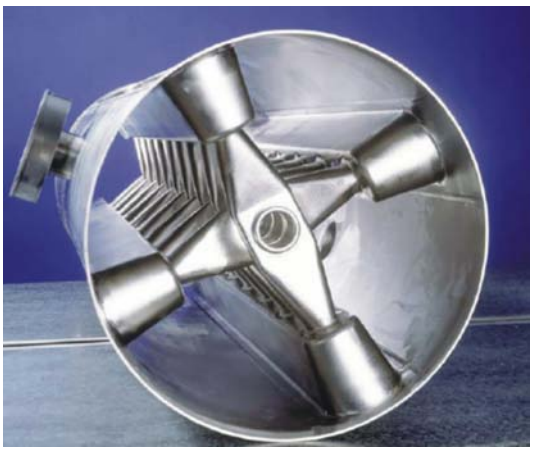

Figure 2.57: The superconducting CH.

Fig.2.49 shows the first superconducting CH-DTL. The geometry of such a cavity is quite different from the room temperature version due to the different properties of the cavities: while room temperature design aims to increase the shunt impedance, in superconducting structure the design is optimized to reduce the peack surface fields. High electric fields can in fact produce field emission with the production of electrons which absorb additional RF power while a transition to normal conducting state can happen if a critical magnetic field is reached (quanching).

For those reason the superconducting CH presents a girder to reduce the surface magnetic field and thus the surface currents which can create resistive heating; additionally, the stems and the drift tubes are larger when compared to the room temperature design in order to reduce the electric peack fields.

A 19-cell, $\beta = 0.1$ CH-prototype cavity has been built at ACCEL Company and cold tests at IAP have started in July 2005. The cavity has a length of 105 cm and a diameter of 28 cm. The cavity has been fabricated from 2 mm thick bulk niobium sheets (RRR=250). After fabrication and surface treatment several tests have been performed in the new cryogenic rf laboratory in Frankfurt [47]. Figure 2.50 shows the measured unloaded Q versus the effective accelerating gradient Ea. The gradient is based on the $\beta\lambda$-definition.

The maximum gradient which has been achieved so far was 4.6 MV/m. This corresponds to an effective accelerating voltage (including T=0.8) of 3.8 MV. The electric peak field was 25 MV/m and the magnetic peak field was 26 mT, respectively. The Q-value at low field level was $5.7 \cdot 10^8$ which gives a total surface resistance of 96 $n\Omega$. The residual resistance is 43 $n\Omega$. The development of a mechanical tuner has started.

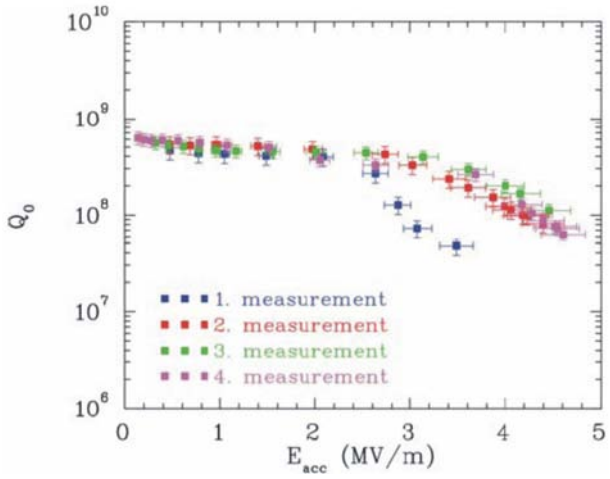

Figure 2.58: The Measured unloaded Q-value versus the effective accelerating gradient.

Presently the cavity is being prepared for cryogenic tests in a horizontal cryostat.

Chapter 3

The GSI Proton Injector

3.1 Motivation for the FAIR Proton Injector

As explained in Sect.1.4.1 one of the main feature of FAIR is the parallel operation which allows to accelerate different ions species. In this way up to four scientific programs can be run at the same time. In Fig.3.1 the scheme of parallel operation at FAIR is illustrated. A primary proton beam is injected into the SIS100 and used to produce an intense $\bar{p}$ beam which is then collected, accumulated and cooled in the CR/NESR storage ring-combination before the transfer to the NESR or HESR for the experiments. In parallel, i.e. during the fraction of the SIS100 super-cycle not needed for the protons, a primary ion beam is accelerated in SIS100 and slowly extracted to the Super-FRS to produce radioactive secondary beams for fixed target experiments (violet-dashed) or for storage in the CR and NESR instead of antiprotons (blue-dashed). In addition, every 10-100 seconds a high-energy heavy-ion beam (red) is accelerated in SIS100/300 and slowly extracted for nuclear collision experiments. Moreover, intense compressed beam pulses (green) are provided every few minutes for plasma physics experiments that require very low repetition rates. Alternatively, atomic physics experiments (light blue) may be served by SIS100 in the pauses of the antiproton production.

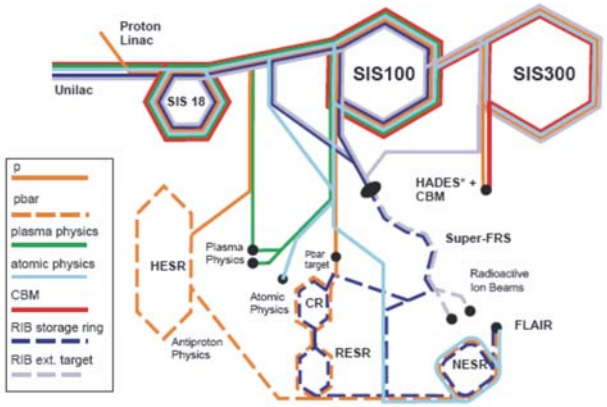

Figure 3.1: Illustration of the parallel operation at FAIR.

The antiproton physics program at FAIR requires an intensity up to $7 \cdot 10^{10}$ $\bar{p}/h$

which, taking into account the $\bar{p}$ production and cooling rate, implies a primary proton beam of $2 \cdot 10^{16}\ p/h$. This intensity is much beyond the capabilities of the existing UNILAC, and for this reason, a dedicated proton linac has to be used as injector into the SIS 18/100 synchrotrons.

The primary proton beam intensity is limited by the Space Charge Limit of the SIS18, which can be expressed as [49],

$$N_{SIS} = 4.305 \cdot 10^{13} \cdot \beta^2\gamma^3 \tag{3.1}$$

while the $\bar{p}$ rate is dominated by the stochastic cooling time which is proportional to the particle number if a sufficiently high signal/noise ratio is assumed. During this time the SIS100 will be used to accelerate ion species different from protons, as explained before. Fig. 3.2 summarizes these dependencies as function of the proton linac energy.

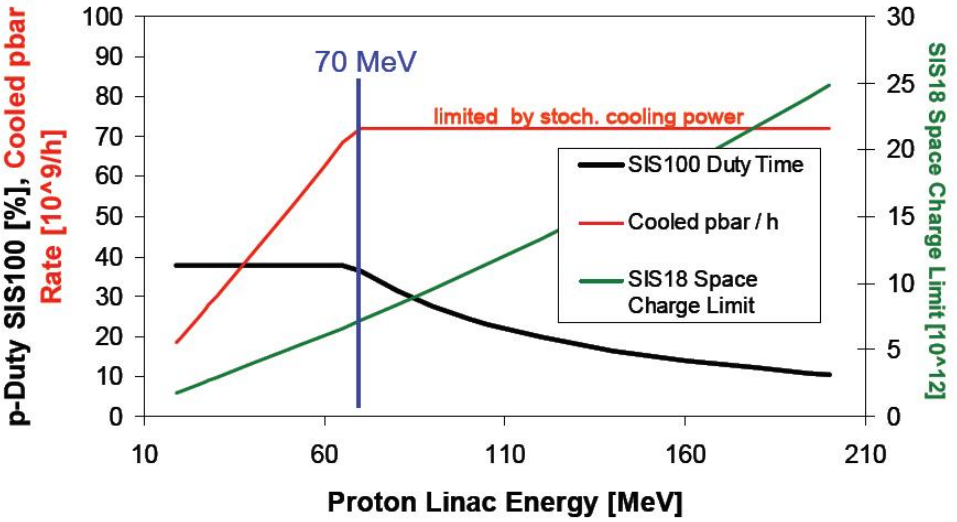

Figure 3.2: Dependence of the space charge limit of proton beams in the SIS18 (green curve) and corresponding relative duty time for primary proton beam delivery by the SIS100 (black) as function of the proton linac energy. The achievable rate of cooled pbars is presented by the blue curve.

An output energy of 70 MeV allows to get close to the saturation of $\bar{p}$ production while a further increase in energy doesn't bring any significant advantage apart from a small decrease of the SIS100 cycle time since the cooling time becomes now longer; moreover, fixing the final energy at 70 MeV avoids any jumps in RF frequency which results in a considerably cost saving.

The choice of frequency for a linac in this energy range results from the compromise between the requirements of minimized radial defocusing at low energy, which is proportional to the frequency itself [cfr. Eq. 1.42], and the RF efficiency which, for room temperature structures, scales as the square root of the frequency [cfr. Eq. 1.13]; for those reasons all linacs in such an energy range are operated at frequencies between 300 and 400 MHz which results to be an adequate compromise. Additionally, the LEDA project in Los Alamos has successfully demonstrated the proton acceleration at beam currents up to 100 mA with a 350 MHz RFQ (see e.g. [50]). The original choice for the GSI proton linac foresaw the use of the 352.2 MHz, 1.1 MW, CERN klystrons recovered from the dismounted LEP; finally, after the development of commercial 324 MHz, 2.5

MW Toshiba klystrons for JPARC [cfr Sect.1.4.4], the linac frequency was set to 325.2 MHz which is also exactly three times the frequency of the existing 108.4 MHz GSI UNILAC. In this way the entire GSI injector system will be based on multiple of the same basic frequency of 36 MHz (the operating frequency of the UNILAC High Current Injector HSI).

Since multiturn injection (MTI) of proton beam into the horizontal x-x' phase space of the SIS18 is foreseen, the requirements for the beam current and the emittances can be calculated by a simple analytical model reported hereafter. The maximum number of turns into the SIS18 by MTI is given by

$$N_{t,max} = \frac{A_{SIS}}{\epsilon} \tag{3.2}$$

where A_{SIS} is the horizontal SIS acceptance, 150 μm, and ϵ is the horizontal emittance of the injected proton beam. To avoid losses this maximum number must be reduced to

$$N_t = N_{t,max} \cdot \eta_{MTI}, \tag{3.3}$$

where η_{MTI} is the filling factor of the SIS, typically 60 %, which results in a filling time

$$\tau_{MTI} = \eta_{MTI} \cdot \frac{A_{SIS}}{\epsilon} \cdot \frac{C_{SIS}}{\beta c} \tag{3.4}$$

where C_{SIS}, is the SIS circumference, 216.72 meters. Since the SIS has to be filled up to its space charge limit within one MTI, the injection current must be

$$I = e \cdot N_{SIS}/\tau_{MTI} \tag{3.5}$$

which, taking into account the expression for the space charge limit N_{SIS}, leads to the following relation

$$\frac{I}{\epsilon} = \frac{e \cdot 4.305 \cdot 10^{13} \cdot (\beta\gamma)^3 \cdot c}{\eta_{MTI} \cdot A_{SIS} \cdot C_{SIS}}. \tag{3.6}$$

From this we can define the normalized brilliance as

$$B_n = \frac{I}{(\beta\gamma)\epsilon} = \frac{e \cdot 4.305 \cdot 10^{13} \cdot (\beta\gamma)^2 \cdot c}{\eta_{MTI} \cdot A_{SIS} \cdot C_{SIS}} \tag{3.7}$$

which, assuming the final energy of 70 MeV and introducing the numerical value, gives the minimum required normalized brilliance

$$B_n = 16.4 mA/\mu m. \tag{3.8}$$

Even if the SIS18 requires an injection current of 35 mA, which would correspond to a transversal emittance of 2.1 μm, the whole linac is based on a 70 mA design requiring an output emittance of 4.27 μm: it is in fact possible to foresee a future upgrade of the cooling capabilities of the *CR* which will require higher proton linac current.

3.2 The P-Injector: Design and Main Parameters

The general layout of the Proton Injector is presented in Fig.3.3: the proton beam is generated in an ECR source and extracted at 95 KeV with a maximum current of 100 mA. The subsequent Low Energy Beam Transport (LEBT) consists of two solenoidal lenses and provides the required separation of protons from any of H_3^+, H_2^+, and H_2 fraction: the proton fraction is expected to be higher than 70 %. At this point the beam is bunched and accelerated by an RFQ up to the energy of 3 MeV, where it enters the main linac based on CH-DTL's.

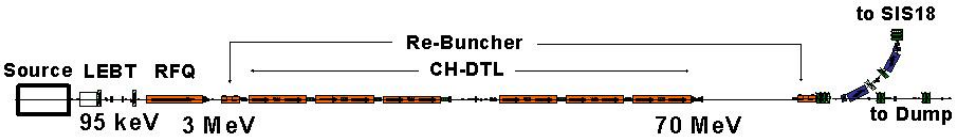

Figure 3.3: The layout of the GSI Proton Injector for FAIR

Proton Source	
Type	ECR
Beam Pulse Length [μs]	≤ 100
Proton Fraction [%]	≥ 70
Extraction Current [mA]	100
Extraction Voltage [keV]	95
LEBT	
Focusing Scheme	2 Solenoids
Output emittance (tot. norm.) [mm mrad]	≤ 1.8
Length [m]	2.5

Table 3.1: The front end parameters of the Proton Injector.

At present two options for the RFQ are under discussion, a 4-rod type, developed by Frankfurt University, and a 4-vane-window structure under investigation at the ITEP in Moscow (see Fig.3.4).

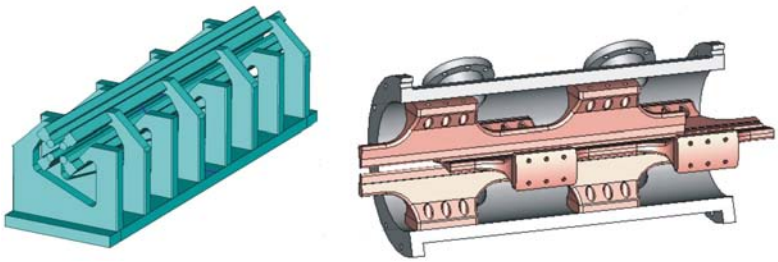

Figure 3.4: The proposed solutions for the RFQ: on the left, the 4-rod option by Frankfurt University, and, on the right, the 4-vane-window structure under investigation at ITEP.

Four-vane RFQ's are the standard solution for such a high frequency but they require

high investment costs due to the high duty cycle which implies an efficient cooling system; on the other hand, 4-rod RFQ's are much simpler and cheaper but there is no previous experience in this frequency range. For this reasons a first model was built in Frankfurt which has demonstrated the feasibility of this kind of RFQ as part of the GSI proton injector [51]. Tab.3.2 summarizes and compares the capabilities of those solutions.

Parameters	**4-rod RFQ**	**4-vane RFQ**
Input Energy (MeV)	0.095	
Input Current (mA)	100	
Input Emittance (transv., norm., tot.) (μm)	1.8	
Output Energy (MeV)	3.00	
Total accelerated output current (mA)	87 (86)	93 (87)
Output Emittance (trans., norm. 95 %) (μm)	2.1-2.0	1.6-1.7
Output Emittance (long., 95 %) keV deg	1220	1200
cavity Q_0-value	2800	6850
distance to closest mode (MHz)	58	3.0
total RF-input power (MW)	0.73	0.79
electrode voltage (kV)	90	100
max. electric field strength (MV/m)	36.3 (1.97 K_l)	37.7 (2.04 K_l)
aperture radius (mm)	2.10 - 3.49	2.16 - 3.28
length (m)	3.2	3.1

Table 3.2: A comparison between the proposed alternatives for the RFQ of the GSI Proton Linac

After the RFQ, the beam enters the MEBT consisting of a single quadruple lens, a rebuncher cavity and, finally, a quadruple triplet which focuses the beam into the main linac based on CH-DTL's operated with the KONUS beam dynamics [37].

In order to match the high power level from the klystrons, 12 CH-DTL's are grouped in 6 pairs of coupled structures [52]: each resonator consists of 2 CH-structures connected by an intertank section which hosts a magnetic lens and which distributes the input power between the accelerating structures.

Three of those coupled resonators accelerate the beam up to 35 MeV where about 60 cm are reserved to a dedicated diagnostics section: after the final acceleration to 70 MeV the energy spread is reduced to less then 1 ‰ by a debunching cavity and the beam is then injected into the SIS18.

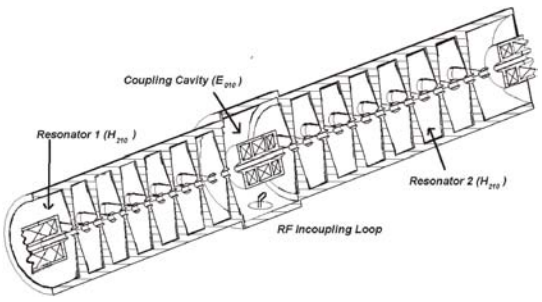

Figure 3.5: An example of coupled CH-structures proposed for the GSI Proton Linac.

3.3 The LORASR Code

The beam dynamics investigations were performed by use of the LORASR Code [53] which is particularly suited for the design of structure based on a KONUS lattice. The code is in use since many years and was successfully benchmarched in many projects, such as the Lead Injector [56] and Rex-Isolde [28] at CERN, the HLI [25] and HSI [26] at GSI, and most recently it was used to design the carbon injectors in the cancer therapy centers HIT (Germany) [29] and CNAO [30](Bella Italia).

LORASR allows beam simulations with space charge along drifts, quadruple and solenoidal lenses, $\beta\lambda$ and $\beta\lambda/2$ accelerating sections, dipole magnets as well as along simple RFQ sections.

Element	Description
Quadrupole Magnetic Lens	Hard Edge Approximation
Dipole Bending Magnet	Multipoles Expansion with Fringe field approximation
$\beta\lambda/2$ **gap**	no focusing elements assumed , 30 steps calculation
$\beta\lambda$ **gap**	Alvarez DTL housing a focusing element
RFQ Section	2-terms potential with fringe fields included
Space Charge Routine	FFT with rectangular boundaries

Table 3.3: The feature of the LORASR code

Recent code developments [54] were focused on the implementation of a new PIC 3D FFT space charge routine which allows time-efficient simulations with up to 10^6 macro particles routinely. This new LORASR Particle-In-Cell (PIC) 3D FFT space charge solver takes advantage of the speed of the FFT algorithm, reducing the number of arithmetic operations from the order of N^2 to the order of $N \log 2N$.

The performance of the new space charge algorithm has been systematically investigated. From theory [55] the following dependence of the processing time T on the particle number N_P and on the grid number N_G is expected:

$$T = T_1 + T_2 = C_1 \cdot N_p + C_2 \cdot N_G \log_2 N_G. \tag{3.9}$$

This dependence has been checked by LORASR runs using $N_P = 10^3$, 10^4, 10^5, $5{\cdot}10^5$ and 10^6 for 3 different grid numbers, N_G = 323, 643 and 1283, respectively. Fig. 3.6 shows how the calculation time is in excellent agreement with Eq.3.9 with the coefficients C1 and C2 determined by fits on the simulation data: in particular C1 has nearly the same value for the 3 different grid point numbers (see Table 3.4). Thus, the processing time is linearly depending on the particle number with an additional constant value T_2 depending on N_G and which scales as follows for different grid numbers:

$$T_{2,32} = T_{2,128} \cdot \frac{32^3 \log_2 32^3}{128^3 \log_2 128^3} \tag{3.10}$$

According to the results shown in Fig.3.6 and Table 3.4, an adaptive fitting of the mesh point number is the right solution as already implemented in LORASR: a 32^3 grid is used for $N_p \leq 104$, 64^3 for $Np \leq 105$ and 128^3 for$Np \leq 106$, respectively. Due to

	32^3	64^3	128^3
C1 [s]	$8.1\ 10^{-6}$	$8.1\ 10^{-6}$	$8.0\ 10^{-6}$
C2 [s]	$5.4\ 10^{-8}$	$8.1\ 10^{-8}$	$10.9\ 10^{-8}$
T2 [s]	$9.0\ 10^{-3}$	$1.3\ 10^{-1}$	1.61

Table 3.4: Resulting parameters of the LORASR Code Performance Test.

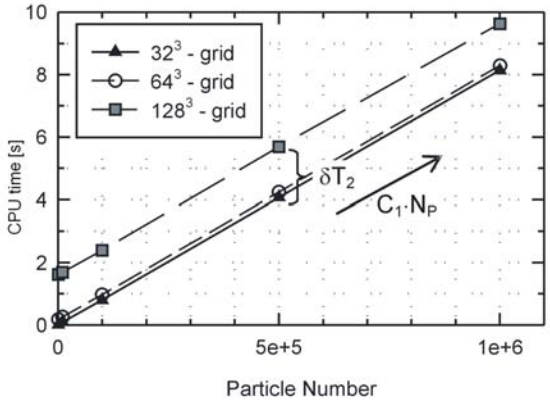

Figure 3.6: Performance test of the new LORASR 3D FFT space charge solver: calculated processing times (in seconds) for single space charge calls on a PC with a 3 GHz CPU.

the efficiency of the new space charge routine, validation runs with 10^6 macro particles are now routinely available in LORASR, resulting in total CPU times below 4 hours on a modern PC with a 3 GHz CPU for the given GSI Proton Linac example (1000 space charge calls in total). The LORASR code was successfully validated within the European 'HIPPI' Project activities [57]: the new space charge routine was tested within the Poisson solver benchmarking program, showing good agreement with the results from other codes like IMPACT [58], HALODYN [59], DYNAMION [60] and TOUTATIS [61].

Additionally a tracking comparison was performed on the 1.4 - 11.4 AMeV GSI UNILAC Alvarez DTL, where, apart from the codes already mentioned also PARMILA [62], PATH [63] and PARTRAN [64] were included. The level of agreement between the results is encouraging. As a consequence, LORASR can be considered as an authorized tool for future DTL beam dynamics designs.

3.4 The Design of the FAIR P-Injector

3.4.1 The Input Distribution

The starting point for the design of the Proton Linac is the output distribution of the RFQ. In order to get the most realistic results it was decided to base the linac design on a 4-rod RFQ output distribution generated with the PARMTEQ code [65], avoiding any ideal self-generated distribution such as a Gaussian or a K-V beam. Such a distribution is illustrated in Fig.3.7, while Tab.3.5 shows its main parameters.

The distribution is characterized by a filamentation in the longitudinal phase space with a large phase spread, $\sim 50°$, while the beam is divergent in the X-X' plane and converges in the Y-Y' plane. The filamentation is due to the fact that the RFQ is

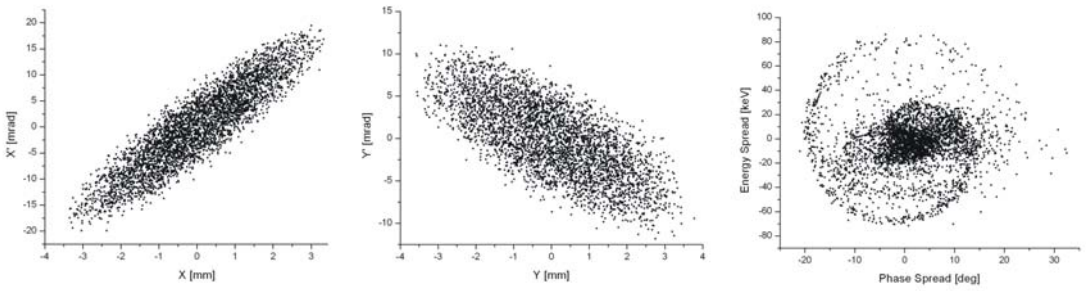

Figure 3.7: The RFQ-output distribution used for the design of the proton injector.

Input Current (mA)	70
Input Energy [MeV]	3
Input Emittance (long., 95 %) [keV ns]	12.07
Input Emittance (X-X', 95 %) [mm mrad]	1.788
Input Emittance (X-X', 95 %) [mm mrad]	1.726
RMS Input Emittance [keV ns]	1.57
RMS Input Emittance [mm mrad]	0.361
RMS Input Emittance [mm mrad]	0.356
Number of particles	3950

Table 3.5: The main beam parameters of the RFQ-output distribution which is used as input distribution for the MEBT and DTL simulations. The emittance values refer to the area of space subspace which includes 95 % of the particles while for the RMS emittence all particles are included in the calculation.

optimized to transport the full current coming from the source (100 mA), assuming then a stronger action of the space charge forces on the beam; another reason for such an effect is that the RFQ proposed for the Proton Injector is extremely short and then characterized by a strong acceleration gradient with a relative low number of bunching cells.

On the other side, the opposite behavior of the beam in the transversal planes suggests the idea to place in front of the main linac a single quadrupole in combination with a short buncher cavity: in this way a transversally convergent beam with a reduced phase spread can be easily matched to the first CH module and then be accelerated with a reduced emittance growth resulting in a higher beam quality.

3.4.2 The MEBT

For a 70 mA proton beam the medium energy matching section, MEBT (Medium Energy Beam Transport), should be carefully designed to avoid large emittance growth and to avoid any source of beam losses, as qualitatly described in [68]. The design must provide the optimal matching between the RFQ and the first CH tank and, at the same time, should also take into account the necessary space for beam diagnostics.

To ensure an efficient linac operation at different beam currents an independently phased resonator must be used to bunch the beam while an XY steerer and a quadruple

singlet will be used to ensure a correct transversal positioning of the beam coming from the RFQ. Finally, as illustrated in Fig.3.8 a pick up and a current transformator will monitor the beam properties while a final triplet will refocus the beam before the injection into the main linac.

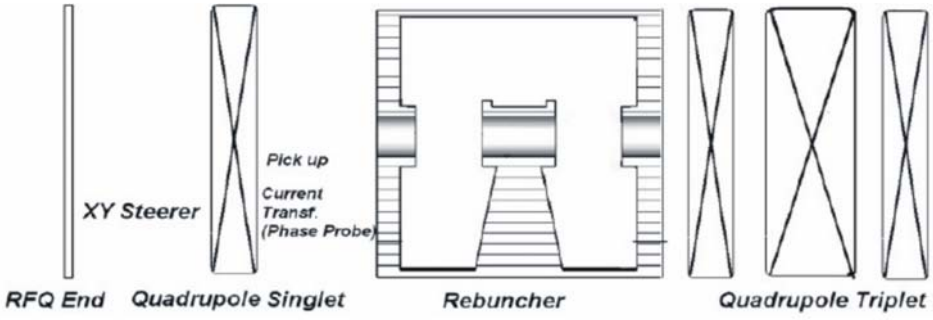

Figure 3.8: The matching section between the RFQ and the first CH module.

Several choices are possible concerning the type of cavity to be used to bunch the beam, 2 or 4 gaps resonator, second harmonic buncher, etc etc, but in order to leave sufficient space for diagnostics and to be more robust against beam parameter fluctuations a short quarter wave resonator made of 2 gaps seems to be the preferable solution: the lower cavity impedance will provide in fact a more robust buncher operation. This solution is also preferable in terms of power consumption, which can be easily estimated by a simple model based on the power needs of the 4 gaps, 108 MHz quarter wave rebuncher installed at the UNILAC.

The UNILAC rebuncher presents an effective shunt impedance Z_{eff} of 70 MΩ/m which is independent on the particle velocity [67]: one can write

$$P = \frac{U^2}{Z_{eff} \cdot l} \tag{3.11}$$

where P is the needed power, and Z_{eff} the effective shunt impedance and l the length of the cavity

Since the shunt impedance scales as the square root of the frequency, one has

$$Z_{eff} = 70 \cdot \left(\frac{325}{108}\right)^{1/2} = 121 M\Omega/m \tag{3.12}$$

Assuming an effective voltage of 0.1450 MV per gap, a total length of $\sim$ 7.6 cm and by reducing for safety margin the shunt impedance to the value of 100 $M\Omega/m$ we have

$$P = \frac{(0.29 \cdot 10^6)^2}{0.76 \cdot 10^8} \cong 11 kW \tag{3.13}$$

which can be safely supplied by a solid state amplifier.

Fig.3.9 shows the particles distribution at the exit of the MEBT: the beam is transversally focused while the longitudinal phase is reduced to $\sim 40^\circ$ with a small increase of the emittance as shown in Tab.3.6.

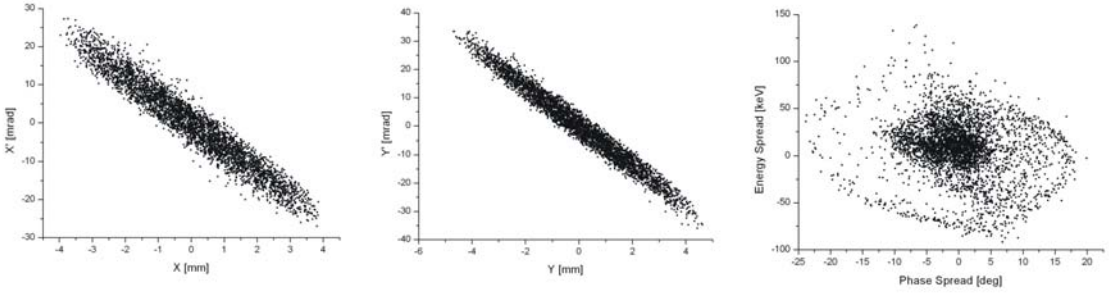

Figure 3.9: The particle distribution at the exit of the MEBT.

Output Emittance (long., 95 %) [keV ns]	12.22
Output Emittance (X-X', 95 %) [mm mrad]	2.03
Output Emittance (X-X', 95 %) [mm mrad]	1.89
RMS Output Emittance [keV ns]	1.57
RMS Output Emittance [mm mrad]	0.39
RMS Output Emittance [mm mrad]	0.38
Number of gaps	2
gap length [mm]	20.6
Tube length [mm]	16
Total length [mm]	~ 76
Eff. Voltage per gap [MV]	0.1450
Heat Power [kV]	37

Table 3.6: The main features of beam at the MEBT exit.

3.4.3 The DTL Entrance

After the MEBT the beam is ready to be accelerated into the main linac : as already explained the project assumes the use of 2.5 MW klystrons which suggests the idea to use coupled structures. This, of course, influences the beam dynamics as well since the large avaibility of power allows a design characterized by a higher acceleration gradient, especially at the low energy side where the CH-DTL presents an extremely high RF efficiency.

On the other side, at 3 MeV, the space charge strongly influences the beam behavior and, for this reason, the design should carefully take this effect into account in order to reduce the emittance growth and to avoid particles losses. The search of a high acceleration gradient which could ensure a high beam quality without beam losses has been the main goal in the design of the first module which brings the beam from 3 to 11.6 MeV, corresponding to $\beta_{in} = 0.0798$ and $\beta_{out} = 0.156$, respectively.

The first tank must be short enough in order to avoid particle losses and for this reason a 10 gap structure was chosen: following the KONUS scheme, the first 3 gaps operate at $-30°$ to bunch the beam while the following 7 gaps operate at $0°$ and perform the main acceleration increasing the beam energy to 6 MeV. At this point, a magnetic quadrupole triplet is used to focus the beam which enters the second section.

The second section, in order to provide the same axial electric field of the first section, around 16 MV/m, is operated with a higher voltage, as shown in Fig.3.10; the buncher section consists of 3 gaps operated at $-35°$ with a longer $0°$ section made now by 9 gaps. Fig.3.12 shows the 100 % envelope for the transversal plane: the aperture of the drift tubes is 20 mm in diameter against 30 mm for thee magnetic lenses and, in order to ensure a safety margin against misalignments and gradient errors, the maximum transversal dimensions of the beam are always less than 13 mm. It is important to note that at this energy it would be preferable to use all the aperture of the linac to reduce the phase space density and thus, to reduce the space charge forces driving the emittance growth; of course, this would lead to a design which could easily cause beam losses due to mechanical misalignments of the accelerator components and, for such a reason, an adequate compromise on the beam aperture must be found.

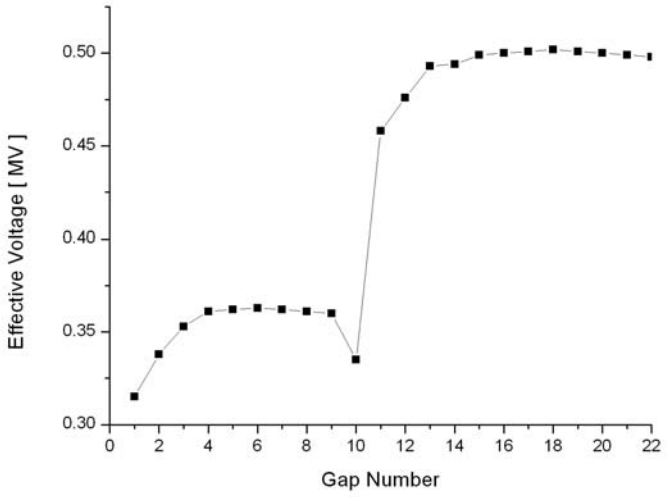

Figure 3.10: The Effective Voltage distribution for the first module, section 1 and 2, of the P-Injector.

3.4.4 General Linac Design

After the first module the linac continues with two coupled modules up to the energy of 36 MeV where a dedicated section for diagnostics is foreseen: this section will include the most common diagnostics devices to control the beam quality such us a Faraday cup, a slot grid array for emittance measurements, a phase probe, a current transformator and a beam profile monitor for a total length of ~ 60 cm. After this section other three modules bring the beam to the final energy of 70 MeV where it is debunched and finally transferred to the SIS 18. The length of the linac is around 23 meters: just to give an idea of the capabilities of this new kind of injector we can just observe that the new LINAC4 at CERN needs around 36 meters to reach the same energy.

Table 3.7 describes the main features of each single section: each structure has a classical KONUS scheme with a rebunching phase of $-30°, -35°$ with the exception of the seventh tank which presents a buncher phase of $-45°$. This tank in fact follows the long drift section used for the diagnostics which, of course, leads to an increase of the

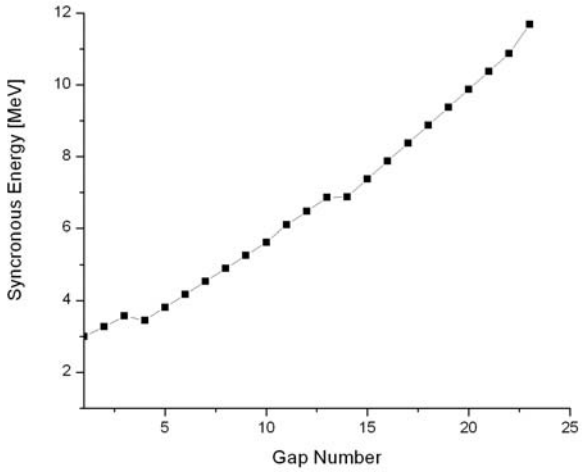

Figure 3.11: The Energy Profile for the first module, section 1 and 2, of the P-Injector.

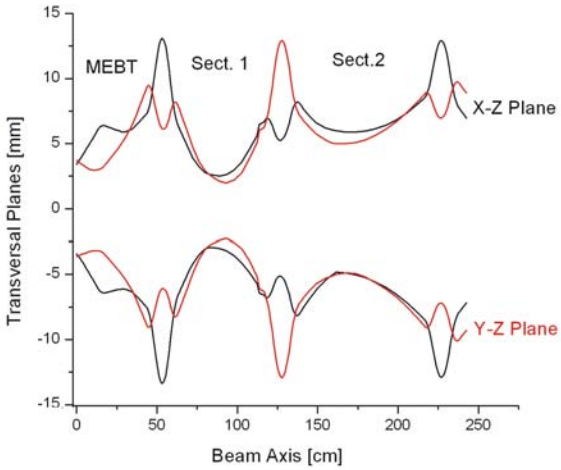

Figure 3.12: The transversal envelope for the first module, section 1 and 2, of the P-Injector.

phase spread of the bunch: for this reason a lower phase of the rebunching section has to be used before the main acceleration.

In order to keep some safety margin against excessive RF consumption the energy gain grows up to 6 MeV per tank corresponding to a beam loading in the order of 400 kW. Only the fourth section presents a higher value in order to optimize the RF efficiency since in this range of energy the effective shunt impedance of the CH is still quite high allowing a more ambitious design. This is reflected as well in the applied voltage along the whole linac which only in this module presents a quite high value, 8 MV, while it is kept stable in the other modules, $\sim$ 7 MV, and finally decreases in the last three tanks where the RF efficiency of the structure begins to sink down.

The transverse focusing is ensured by electromagnetic quadrupole triplets (EMQ) placed between each section. Four different types of quadrupole lenses are used along the linac and the beam transport sections: the amount of types results from the variation

Sec.	Konus Scheme	Energy [MeV]	Total Length [cm]	Beam Load [kW]	X-Y-Z RMS emitt. at the exit
1	$3 \cdot -30^\circ + 7 \cdot 0^\circ$	3-6.09	112	216.6	0.39-0.40-1.72
2	$3 \cdot -35^\circ + 9 \cdot 0^\circ$	6.09-11.69	212	391.8	0.53-0.48-1.80
3	$3 \cdot -35^\circ + 10 \cdot 0^\circ$	11.69-17.46	339	403.8	0.55-0.56-1.81
4	$3 \cdot -35^\circ + 11 \cdot 0^\circ$	17.46-24.30	498	478.8	0.56-0.52-2.38
5	$4 \cdot -35^\circ + 11 \cdot 0^\circ$	24.30-30.25	682	416.5	0.56-0.59-2.49
6	$4 \cdot -35^\circ + 11 \cdot 0^\circ$	30.25-36.43	884	432.6	0.59-0.60-2.38
7	$4 \cdot -45^\circ + 11 \cdot 0^\circ$	36.43-42.36	1163	415.0	0.59-0.63- 2.10
8	$4 \cdot -35^\circ + 11 \cdot 0^\circ$	42.36-48.35	1397	419.4	0.59-0.63-2.27
9	$4 \cdot -35^\circ + 11 \cdot 0^\circ$	48.35-54.51	1634	432.2	0.59-0.64-2.24
10	$3 \cdot -35^\circ + 10 \cdot 0^\circ$	54.51-60.40	1893	412.3	0.61-0.63-2.37
11	$3 \cdot -30^\circ + 11 \cdot 0^\circ$	60.40-66.33	2105	415.6	0.61-0.59-2.48
12	$3 \cdot -35^\circ + 10 \cdot 0^\circ$	66.43-70.50	2371	397.6	0.61-0.61-2.56

Table 3.7: Main Parameters of the DTL sections

of the beam focusing with the beam energy and due to the enhanced space charge defocusing for energies below 20 MeV. The low energy end is more sensitive to emittance growth and to preserve a high beam quality in this section the section should be designed as compact as possible, i.e. using short quadrupoles. However, all quadrupoles used along the DTL have the same aperture with gradients resulting in pole tip fields below 1 T.

Different from other recent projects, such as CERN Linac4 or SNS, the GSI Proton Injector will not use permanent magnets as focusing elements: one reason for this choice is imposed by the fact that the initial current value of 35 mA will be upgraded up to 70 mA requiring some flexibility in the settings of the machine; moreover, EMQ's are much more robust during the years and they are less sensitive to beam losses when compared to PMQ's. Finally, this new machine could be occasionally operated at significantly lower intensity beam for physics programs different from the $\bar{p}$ programof FAIR, for example for π-meson production.

3.4.5 Results and Comments

The main features of the beam at the final energy of 70 MeV are summarized from Figg.3.14-19 and in table 3.9. The beam is transported at a transmission of 100 % through the linac within the requirements for the injection into the SIS18. The relative rms emittance growth is around 70 % in both transversal planes and 60% in the longitudinal plane: it is interesting to note how the transversal emittance grows inside the first two coupled modules and then it becomes quite stable throughout the remaining cavities. The reason of this beam behaviour is a combination of the large effect of the space charge forces at lower energies together with the necessity of keeping the dimension of the beam as smalle as possible in order to reduce the probability of losses (see Fig.3.15). On the other side, due to the large input emittance in the longitudinal plane, the design was intented to minimize the emittance growth in this plane which corresponds to an increase in the transversal planes.

Element	Lenses	Effective Length [cm]	Gradient [kG/cm]
1	1	4.50	2.3
2	3	4.5 - 8.0 - 4.5	5.7 - 5.15 - 5.7
3	3	5.0 - 9.0 - 5.0	6.3 - 5.95 - 6.3
4	3	4.5 - 9.0 - 4.5	6.6 - 6.35- 6.6
5	3	5.0 - 9.0 - 5.0	6.35 - 6.4 - 6.35
6	3	5.0 - 9.0 - 5.0	5.5 - 5.9 - 5.8
7	3	5.0 - 9.0 - 5.0	5.7 - 5.95 - 5.7
8	3	4.5 - 9.0 - 4.5	6.23 - 6.18 - 6.23
9	3	4.5 - 8.0 - 4.5	5.9 - 6.35 - 5.9
10	3	5.0 - 9.0 - 5.0	5.38 - 5.6 - 5.38
11	3	4.5 - 8.0 - 4.5	5.9 - 6.55 - 5.9
12	3	4.5 - 8.0 - 4.5	5.7 - 6.35 - 5.7
13	3	4.5 - 8.0 - 4.5	5.87 - 6.15 - 5.87
14	3	4.5 - 8.0 - 4.5	5.95 - 6.45 - 5.95

Table 3.8: The EMQ settings for the P-Injector

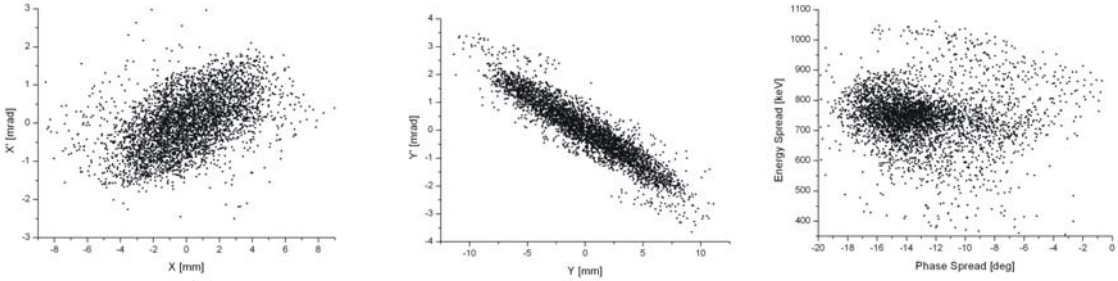

Figure 3.13: The output phase space at 70 MeV for the Proton Injector.

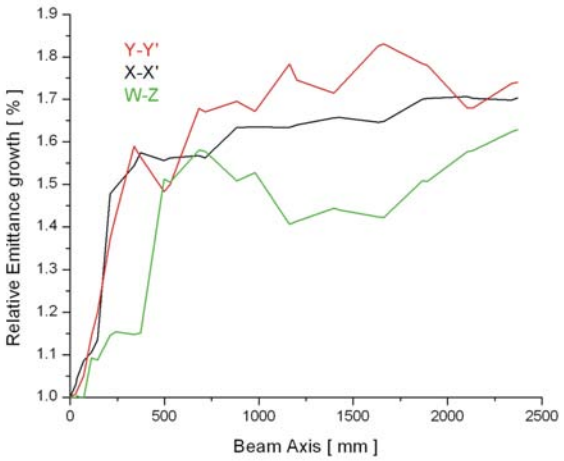

Figure 3.14: The relative RMS emittance growth in the space space.

Output Energy [MeV]	70
Output Emittance (Long., 95 %) [keV ns]	21.8
Ouput Emittance (X-X', 95 %) [mm mrad]	3.71
Output Emittance (X-X', 95 %) [mm mrad]	4.00
RMS Output Emittance [keV ns]	2.56
RMS Output Emittance [mm mrad]	0.61
RMS Output Emittance [mm mrad]	0.61
Transmission [%]	100

Table 3.9: The main beam parameters at the exit of the proton Injector

The envelopes presented in Fig.3.15-19 show the behavior of the beam in the complete 6D space space; transversally the beam is kept narrow and its dimensions decrease significantly in the high energy side where, due to the higher energy, the risk of activation because of potential losses becomes stronger. It is important to notice from Figg.3.15-16 how 95 % of the beam needs a quadrupole aperture smaller than 15 mm, while, apart from the first lens, 99% of the beam requires around 20 mm to be transported. This information is useful in order to understand the behaviour of the outer particles and to define the critical points where a potential beam loss could happen.

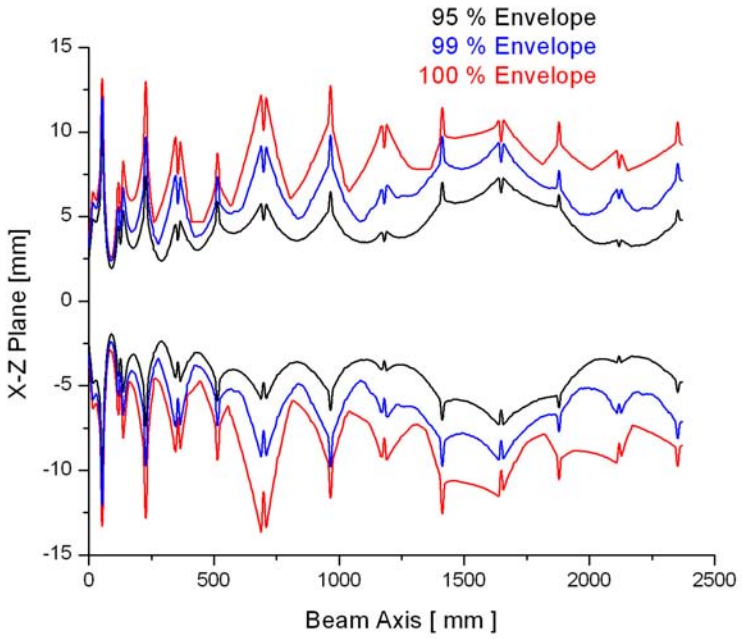

Figure 3.15: A comparison between the 95, 99 and 100 % transversal envelope in XZ plane.

Observing the phase envelope, a typical example of a KONUS scheme, we observe how the first 0° section pushes the beam towards a large negative value of phase avoiding an excessive spread of the beam. After the first module the center of the beam performs small oscillation with a larger phase spread at the exit of the linac.

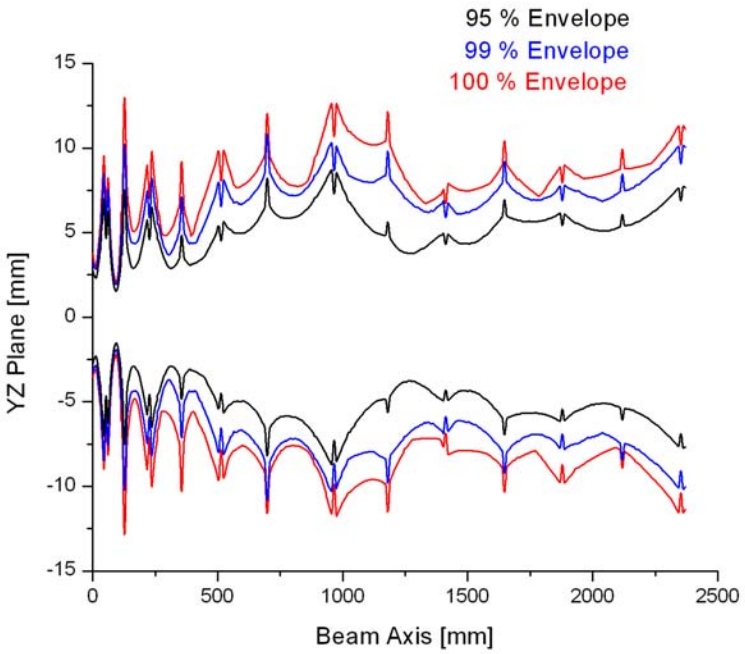

Figure 3.16: A comparison between the 95, 99 and 100 % transversal envelope in YZ plane.

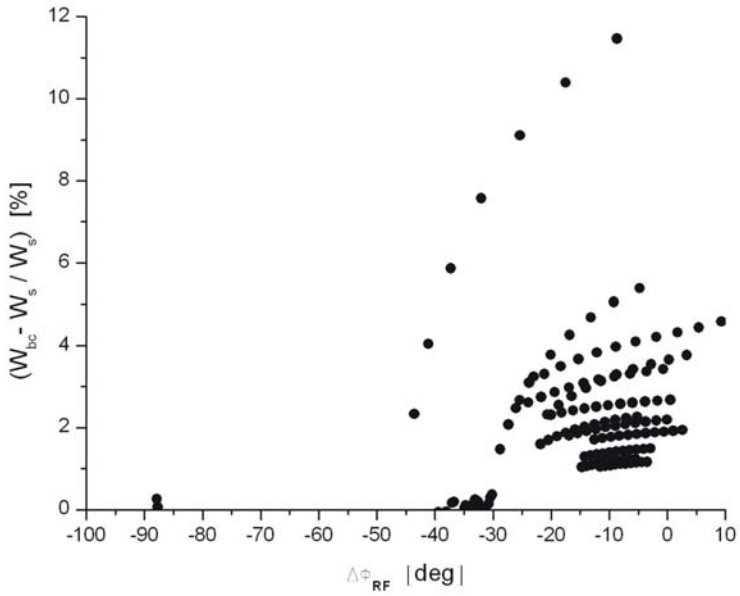

Figure 3.17: The bunch center motion in the longitudinal pahse space with respect to the synchronous phase.

The reason for such a large phase spread is not casual: the exit energy spread is around 1 %, much larger than requested by the injection into the SIS. To overcome this problem, a large drift section is foreseen after the main linac which will increase the phase spread over the linear range of the sinus function in order to apply a debunching

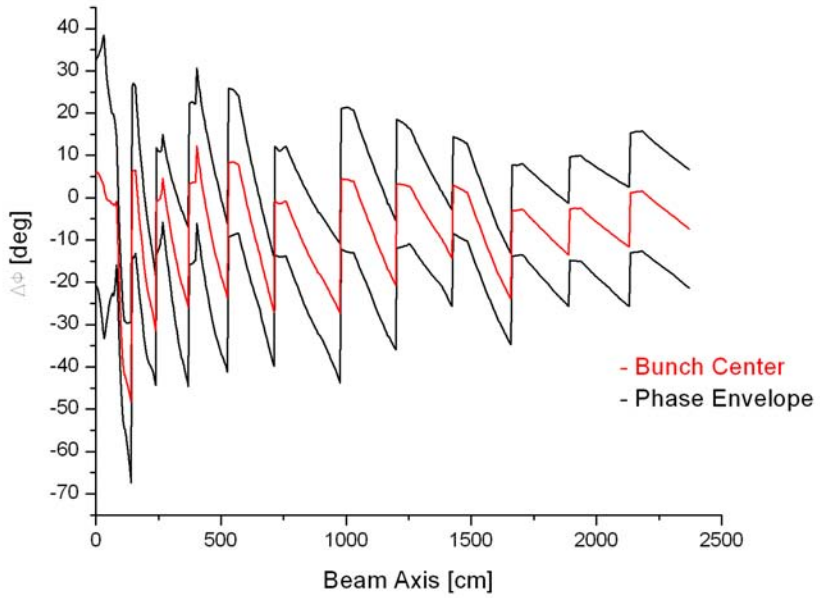

Figure 3.18: The phase envelope with respect to the bunch center. The large width at the exit will be used to reduce the length of the drift section before the debunching cavity.

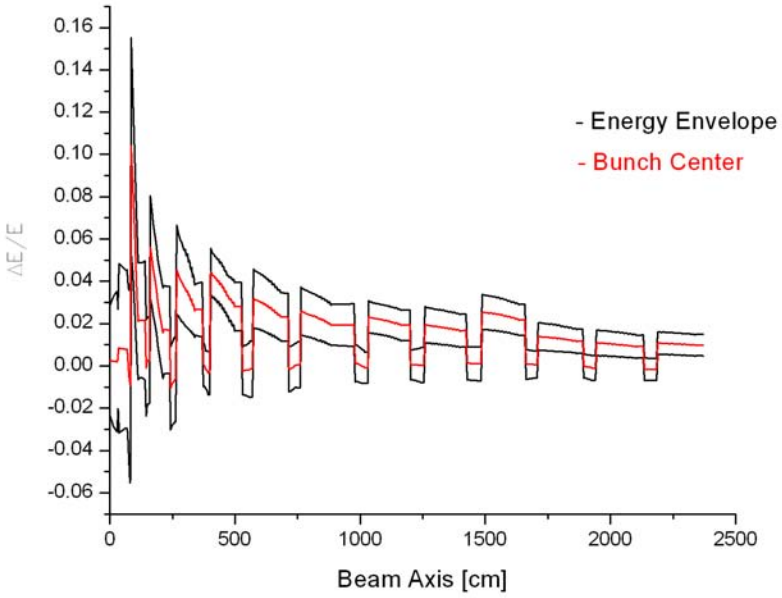

Figure 3.19: The energy envelope with respect to the bunch center. The energy spread of $\sim 1\%$ will be reduced by a dedicated rebuncher cavity after a long drift space.

voltage which will reduce the energy spread to the requested range of ±1‰. Thus, delivering a beam with a larger phase spread would help to reduce the length of this drift section reducing the building investments.

3.4.6 The diagnostics section

In order to keep under control all the beam parameters during operation, the proton linac will be equipped with a diagnostics set which will monitor the beam all along the linac: the position of each device is illustrated by Fig.3.20. After the third module of the proton injector around 60 cm are left to install the illustrated devices; a triplet will then refocus the beam and, it is very important to note that even after such a long drift no rebuncher cavity is needed before the further acceleration in the second part of the linac.

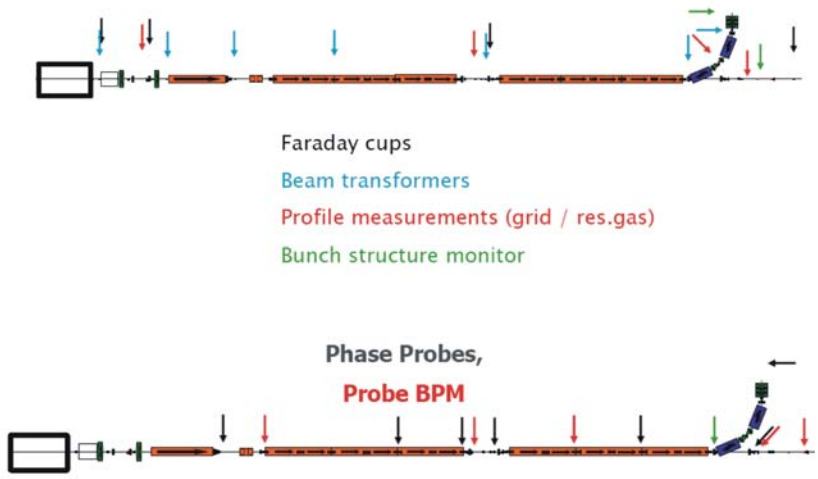

Figure 3.20: The scheme for the diagnostics along the proton linac.

This long drift will include

- a Faraday cup which, beside the current measurement, willl also serve as a beam dump for the full beam power;
- a current transformer of the type that are in operation at the UNILAC [72] since several years. They are well suited for beam pulse lengths from a few μs up to the maximum design length of 36 μs offering high sensitivity and large dynamic range. For readout and presentation a versatile data acquisition system is in preparation for the UNILAC. This system can be duplicated for the proton linac.
- a capacitive beam position monitor (BMP), forming a compact mechanical unit with a current transformer. This devices allows to control the matching between the bunches and cavities very precisely. Due to the higher accelerating frequency of the proton linac compared to the UNILAC (108 MHz), the front-end electronics have to be modified to provide large enough bandwidth.
- two phase probes, one at the beginning and one at the end to control the width of the beam and to measure the energy by a flight of time method.

The solution to set this large section in the middle of the accelerator has the main advantage to reduce the number of diagnostics elements which has to be integrated after each acceleration module: this reduces the number of mechanical constraints in the design of the cavity reducing the longitudinal dimension of each single intertank section. This will be helpful in terms of longitudinal beam dynamics as well since the beam profits a lot of short intertank sections.

On the other side, it is very important to investigate the effect of this large section on the beam transmission rate, especially because misalignemnt errors of the triplet could lead to substantial beam losses: for this reason, a complete error study was performed and it is presented at the next section of this chapter.

3.4.7 The Transfer Line

After the last triplet of the Proton Injector the beam will be transferred to the SIS according to the scheme illustrated in Fig.3.21; two bending magnets inflect the beam in the long drift needed to enlarge the phase spread; a horizontal scraper (8 mm aperture) is placed between those bending magnets in order to clean the beam from outer particles. The transmission rate after those scrapers is 97 %. After 7.5 meters of drift the beam phase spread reaches the non linear range of the sinus function and a debunching voltage can be applied: at the moment it is foreseen to use a 6 gaps CH cavity operated with an amplitude voltage of 110 kV per gap. As shown in Fig.3.22 in this way the energy spread is reduced to the level of ±1‰ which is the requirement for the injection into the SIS 18 via multiturn injection.

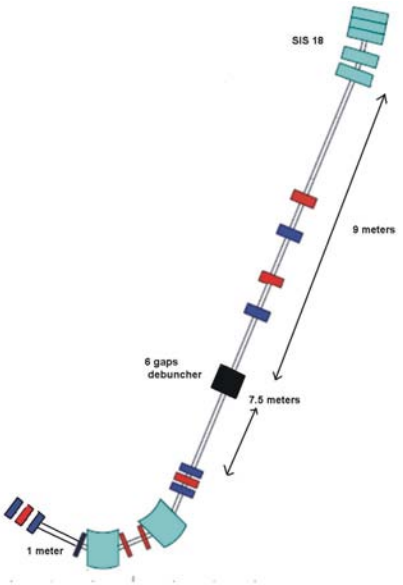

Figure 3.21: The transfer line from the proton injector to the SIS18:in light blue the bending magnets and in red and blue the quadrupoles magnets.

This results demonstrate the capabilities of the CH-mode structure in combination with the KONUS beam dynamics to accelerate an ion beam in a very efficient way without loosing in beam quality. In particular the controlled growth of the rms emittance obtained with a realistic output distribution from the RFQ are a strong hint of the

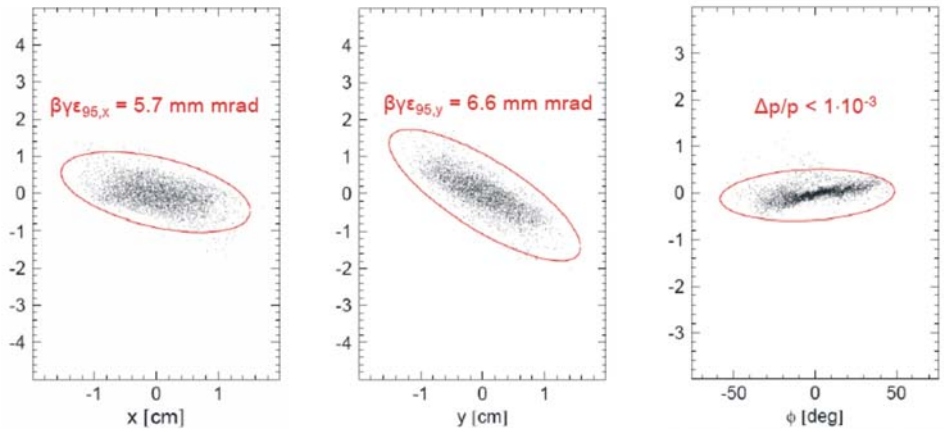

Figure 3.22: The 100 % emittances at the injection into the SIS 18: the energy spread is reduced to the level of ±1‰.

capabilities of such a combination to accelerate beams up to several tenth of AMeV as will be done for the first time with the GSI proton injector.

3.4.8 Influence of particles number

The input distribution used to design the lattice of the Proton Injector consists of 3950 macro particles: an important point to investigate is whether a higher number of particles could lead to substantial different results in terms of transmission rate and beam quality. For this reason the same RFQ settings were used to generate a second output distribution characterized by a higher number of macroparticles, 19816. In order to obtain consistent and comparable results, this new output distribution should not differ from the original one in terms of RMS emittance so that a comparable effect of the space charge can be assumed in both cases.

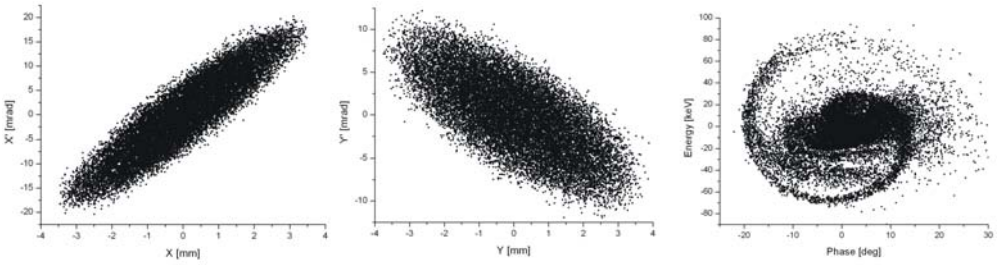

Figure 3.23: The 19816 macroparticles RFQ-Output distribution.

By comparing the results shown in Tab.3.10 with the ones shown in Tab.3.5 we can get the following conclusions: running through the same lattice with the same magnet gradients two distributions characterized by the same RMS emittance and differing only in the number of particles the results are comparable. The differences in the final RMS emittance can be understood observing that, in order to get the initial RMS unchanged, the distribution with the higher number of particles must occupy a larger portion of the phase space. This increases the beam halo and leads to an increase of the emittance

Input Emittance (long., 95 %) [keV ns]	11.90
Input Emittance (X-X', 95 %) [mm mrad]	1.83
Input Emittance (X-X', 95 %) [mm mrad]	1.77
RMS Input Emittance [keV ns]	1.55
RMS Input Emittance [mm mrad]	0.37
RMS Input Emittance [mm mrad]	0.36
Number of particles	19816

Table 3.10: The main beam parameters of the RFQ-output distribution generated with 19816 macroparticles.

Output Energy [MeV]	70
Output Emittance (long., 95 %) [keV ns]	23.1
Ouput Emittance (X-X', 95 %) [mm mrad]	4.0
Output Emittance (X-X', 95 %) [mm mrad]	4.70
RMS Output Emittance [keV ns]	3.11
RMS Output Emittance [mm mrad]	0.64
RMS Output Emittance [mm mrad]	0.72
Transmission [%]	99.998

Table 3.11: The main beam parameters at the exit of the proton Injector using the 19816 macroparticles RFQ output distribution.

growth since those external particles are not correctly focused and can also be lost during the acceleration. This explains also why the transmission rate is lower with respect to the original design.

This is the major reason why loss and halo studies need a very high number of particles, especially for those projects which require extremely low loss levels, since it is necessary to investigate in detail the behavior of particles which occupy the outer positions in the phase space.

The same strategy has been used to investigate the robustness of the proton linac design against misalignement errors and voltage fluctuations as explained in the next section.

3.5 Error Studies

For a high current machine particles loss represents a major risk which can cause serious problems in terms of structure activation, component damages and deterioration of the beam quality. For these reasons the design must be very robust against the combination of possible sources of beam losses.

The sources of particles losses can be divided into two major categories:

- static errors, like quadrupole, cavity and drift tube misalignment, manufacturing mistakes, field-flatness or quadrupole gradient errors which can be detected and corrected before the running in of the machine up to some technical limits;

- random errors, like rf source instabilities (amplitude, phase), mechanical vibrations or transient beam loading and RF control errors which mostly appears during operation and very often cannot be predicted or corrected.

In order to investigate the effects of those errors on the beam behavior, beam dynamic codes should provide tools for machine error settings as well as error analysis and loss profile calculation routines. An important outcome of these error studies is the definition of tolerance limits for the manufacturers, of the required cavity RF tuning accuracy, as well as stability limits of the rf sources.

In order to perform such a study on the Proton Linac design, the LORASR code had to be updated with a new error routine which includes

- Quadrupole lens translations in both transversal directions ΔX, ΔY (each singlet separately);
- Gap voltage amplitude errors, $\Delta U_{i,j}$ (each gap j of tank i separately);
- Tank voltage amplitude errors, U_i , equal for all gaps belonging to the same tank i;
- Tank phase errors, $\Delta\phi_i$, applied at the entrance (first gap) of tank i.

These error settings can be defined explicitly , i.e. manually, as well as statistically distributed.

Manual input is adequate when data from measurements is available (e.g. quadrupole alignment listings or measured gap voltages) in which cases a single run is necessary to investigate the effects of a particular set of error parameters.

Statistically generated errors shall simulate all possible combinations of potential errors: this implies that many runs (500 to 1000 typically) are needed to improve the statistical analysis; in LORASR the errors are generated according to a gaussian distribution truncated at 2σ-width.

3.5.1 The Breeding Routine

Thanks to the new FFT space charge routine [54] LORASR allows to simulate up to 10^6 macroparticles within reasonable calculation time; unfortunately output distributions available from RFQ simulations codes have usually much less macroparticles which would make it impossible to perform a loss study starting from an RFQ output distribution directly.

This situation can be overtaken by a method which artificially, starting from a reference distribution, generates a new realistic one with a higher number of particles. The method must take into account three major constraints:

- the reference distribution should already contain a large number of particles in order to improve the statistics;
- the coupling between sub-phase spaces must be kept;
- the RMS emittance should be fixed and kept.

In order to solve these problems, a 'Breeding routine' was developed at IAP by R.Tiede [54, 66] which is based on a 'cloning' type method of the reference distribution; the main steps of this routine can be summarized as follows:

- The original distribution is cloned: all the new particles have the same coordinates in all 6 dimensions: this preserves the coupling between the 2-dim subspaces;
- 'Children' particles are randomly (Gaussian) shifted in each 2-dim subspace, within circles with radii corresponding to the local particle density. To avoid local clustering around the initial 'halo' particles, in a final step an additional particle scattering procedure is applied;
- By an iterative process the coordinates of all new particles are moved in each 2-dim subspace in radial direction; the procedure is repeated until the resulting rms emittance differs by less than 1 % from the initial distribution rms value.

Fig.3.24 shows a comparison between the reference distribution generated with PARMTEQ including 19816 particles and a 'breeded one' which contains 99080 particles: as one can see the new distribution represents quite well the original one with the main difference that now, a bigger portion of the phase space is occupied. This comes from the constraint to keep the RMS unchanged

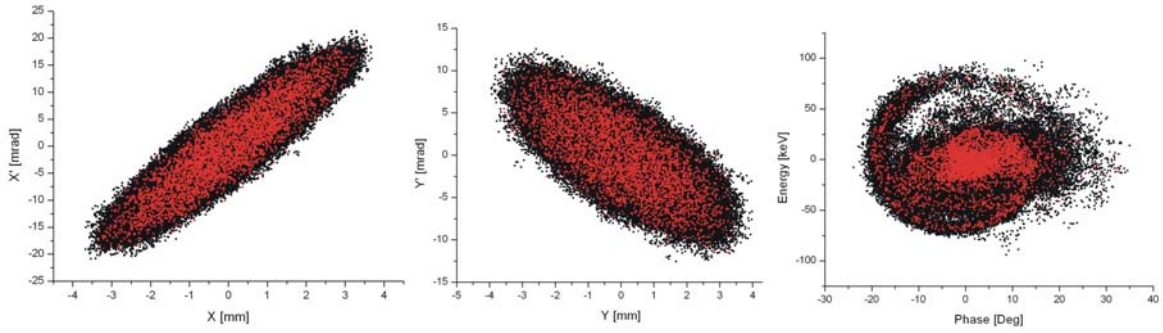

Figure 3.24: The breeding method to increase the number of pacroparticles from an RFQ output distribution: in red the reference distribution and in black the 'breeded' one.

It is of particular interest to compare the results of the PARMTEQ distributions, 3950 and 19186 particles, with the breeded one composed of 99080 particles: Figg.3.24-3.25 show the relative emittance growth in both transversal planes along the 70 MeV GSI proton injector: we can observe how the results are consistent with each other without any significant difference coming from the increasing number of particles.

This authorizes the user to consider the 'breeding routine' as a valid method to generate realistic RFQ output distributions characterized by a very high number of particles and, for this reason ,we decided to use the breeded distribution to check the robustness of the proton injector design against misalignments and other random errors which can occur during the running in of the machine.

As a final remark we can also observe how this result confirms that, in order to design a linac lattice, the number of particles of the input distribution needs not to be very high (a few thousand are normally enough) but it is necessary that the used distribution reflects what realistically is expected at the input of the linac.

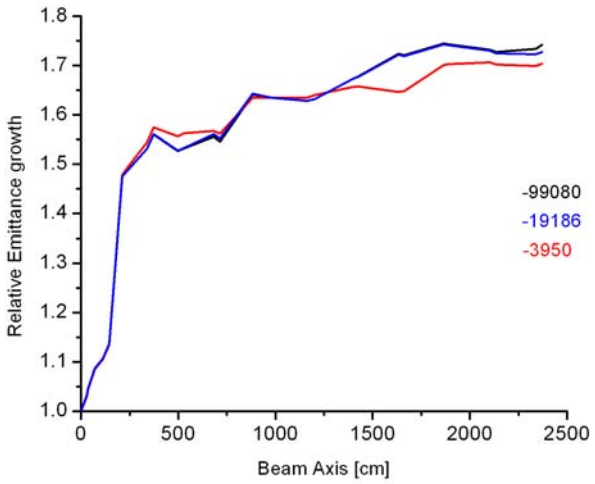

Figure 3.25: The relative emittance growth in the X-X' plane according to the particle number.

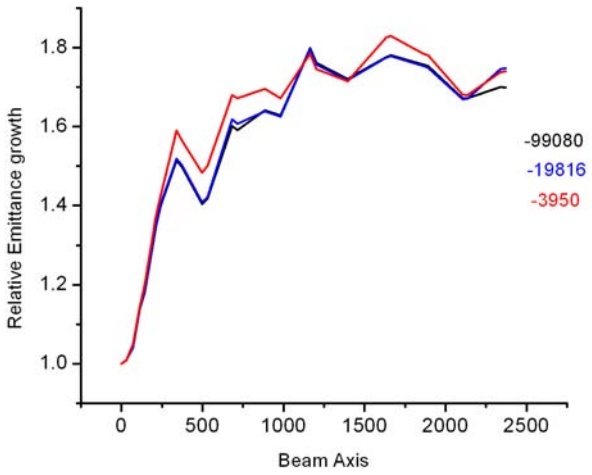

Figure 3.26: The relative emittance growth in the Y-Y' plane according to the particle number.

3.5.2 Quadrupole Misalignment

The most serious source of error which can lead to considerable beam losses is the misalignment of focusing elements: the wrong position of a quadrupole magnet not only results in a different transversal focusing effect, but can also influence the longitudinal behaviur of the particles since the particles will follow now a different trajectory encountering the electric field at a different position and at a different time than designed: the overall effect creates a distortion on the beam dynamics which can result in high loss rates if the design is not robust enough against such an effects.

For this reason particular attention was put on the effect of random misalignement errors on the beam behavior. Three different cases were checked, each generated by a

Gaussian distribution of the misalignment cut at the 2σ value of 0.05, 0.1 and 0.2 mm respectively; in order to have a highly reliable statistics, the 99080 particles distribution was used and 1100 runs were performed for each misalignments σ parameter set.

If the transmission rate is the major parameter to be investigated, it is also important to detect the hot spots of the machine, i.e. the regions which have a high probability to be hit by the beam: this information can be further used, not only to improve the structure, but as well to design the concrete shielding needed for radiation protection safety. For this reason one can define the probability to loose particles per meter by computing the parameter λ, defined as

$$\lambda = \left[\frac{\sum_{i=1}^{runs} N_i}{N_{runs} \cdot N_0} \right] \cdot \frac{1}{dz} \tag{3.14}$$

where N_i is the number of particles lost in each single run within lenght element dz, N_0 is is the initial particles number and N_{runs} is the total number of runs.

Fig.3.27 shows this parameters in combination with the corresponding transmission rate for the mentioned cases.

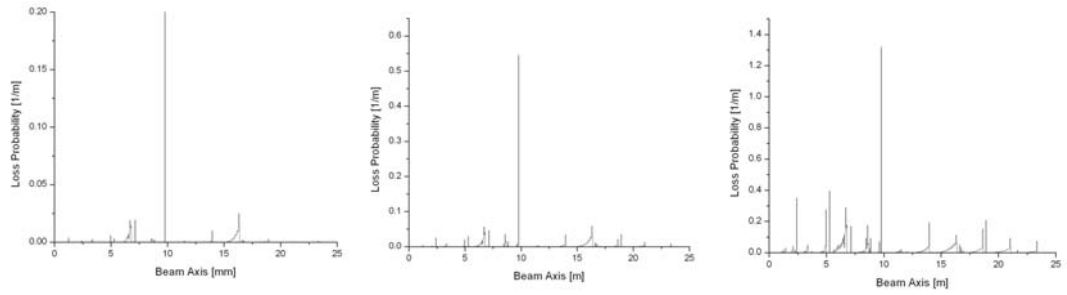

Figure 3.27: The loss profile due to a random average quadrupole misalignments of $\pm 0.05, 0.1, 0.2$mm..

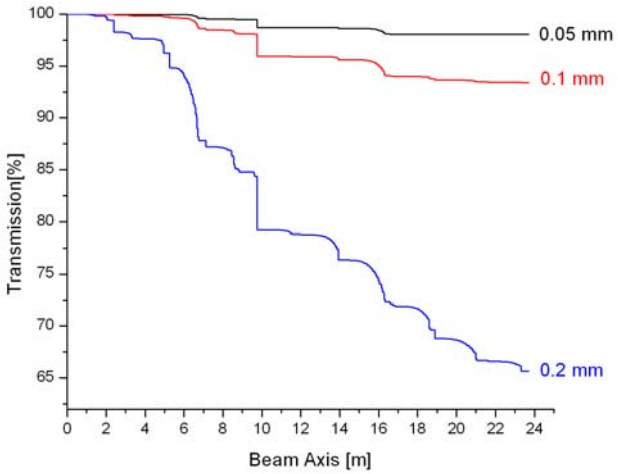

Figure 3.28: A comparison of the average transmission rate for 2σ quadrupole misalignments of $\pm 0.05, 0.1, 0.2$ mm for each singlet.

Misalignements [mm]	Average Transmission [%]
0.05	97.1
0.1	93.37
0.2	65.6

Table 3.12: The transmission rate for quadrupoles misalignments of $\pm 0.05, 0.1, 0.2$.

From this analysis it emerges clearly that the misalignmnts should be kept less than 0.1 mm to keep the transmission rate rather high, while for higher misalignments the transmission drops strastically down. In fact, in this case the cumulative effects of misalignments becomes strong already after the first three quadrupoles leading to considerable losses already after the fist coupled structure.

In all cases the critical point is represented by the long section reserved for diagnostics with other losses occurring in the two following triplets: the long drift destroys in fact the periodicity of the focusing lattice creating a distortion on the transversal dynamics which causes losses not only along the drift but in the following modules as well.

Nevertheless it is very important to observe that the high experience in mounting quadrupole lenses inside H cavities can ensure a rather high precision in the installation of the quadrupole elements: moreover, only the six focusing elements which are mounted inside the acceleration structures could create some problem during the mounting, while an optimal adjustment of the external lenses can be provided with an adequate accuracy.

This is a major advantage of KONUS with respect to classical FODO or FOFODOD lattices used in classical DTL structures: the reduced number of focusing elements results in a compact structure less sensitive to such a kind of mistakes. This becomes particularly important in terms of long operation since the accumulated effect of particles losses can lead to serious damages of the structure components.

3.5.3 Voltage and Phase Errors

Fluctuations from the power supplies lead to variations of the voltage amplitude; another possibility of error from those fluctuations is the phase of the signal which can be shifted with respect the designed value. Those effects can be nowadays kept quite well under control and typical values of random variations are in the range of $\pm 1\%$ for the voltage amplitude and $\pm 1^\circ$ in phase.

As for the quadrupole misalignments, also in these cases 1100 random runs were performed.

As shown from Fig.3.29 to Fig.3.31 those effects, taken individually, don't play a significant role in the beam loss process: in both case the beam is almost fully transmitted and, as for the quadrupole misalignments, the hot spot is represented by the large section needed for diagnostics.

3.5.4 Combining Effects

The analysis of single error effects has shown how the quadrupole misalignments play a major role in the beam loss process since the losses due to the phase and voltage fluctuations can be almost neglected.

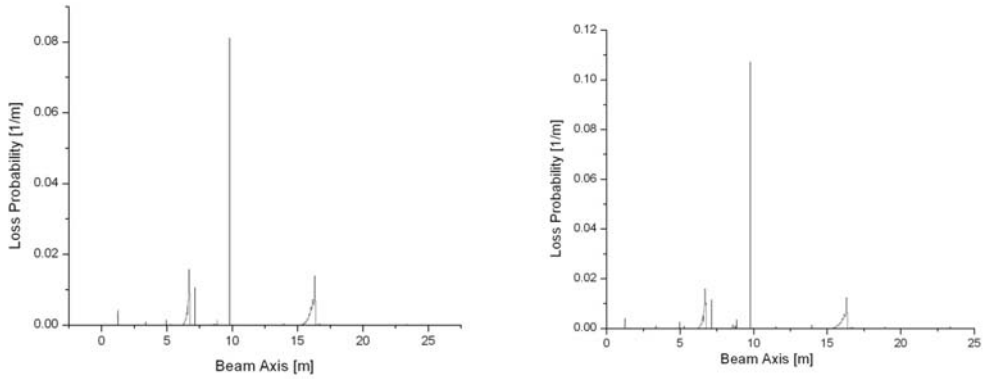

Figure 3.29: On the left the loss profile due to a gaussian phase variation cut at $2\sigma \pm 1^\circ$, on the right the loss profile for the voltage when the random generator is cut at $\pm 1\%$.

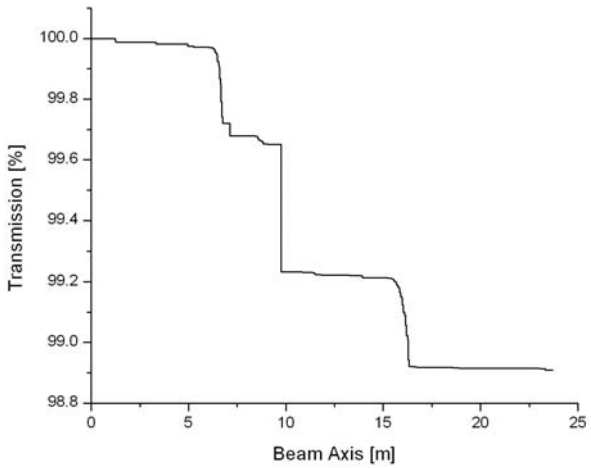

Figure 3.30: The beam transmission when a random error voltage of $\pm 1\%$ is applied to each tank separately.

As last step it is important to investigate the beam behavior when all those sources of error combine together: in fact, if on one side it is possible to foresee that only a small fraction of particles which are transmitted with quadrupole misalignments will be lost due to the voltage and phase misettings, on the other hand it is very important to quantify this effect in order to exclude a potential destructive combination of all sources of mistake.

Again, the 2σ value of the errors on the random generator was set to 1% for the voltage error, 1° for the phase and 0.05, 0.1 and 0.2 mm for the quadrupole misalignements; in order to perform the most realistic simulations, a single gap error with a 2σ width of 1% was added: this kind of mistake is generally due to a wrong distribution of the electric field along the cavity axis and can be kept within few per mill after the

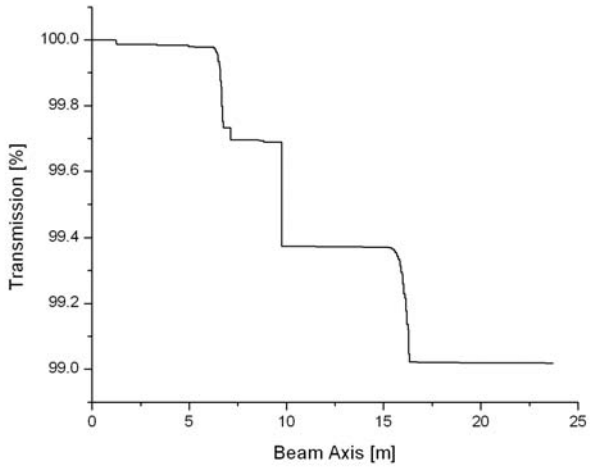

Figure 3.31: The beam transmission when a random phase of $\pm 1^{\circ}$ is applied to each tank separately.

tuning procedure.

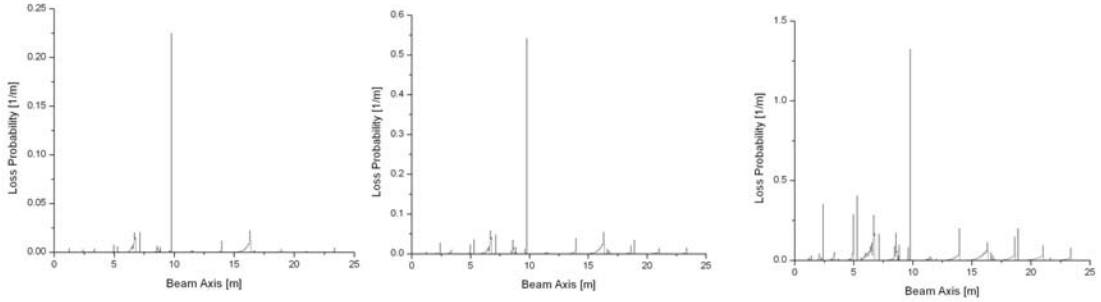

Figure 3.32: The loss profile including all possible sources of errors for three different quadrupoles misalignments.

The results from Fig.3.32 and 3.33 confirm that the combination of all sources of errors does not deeply differ from the results of single quadrupole misalignments: this can be explained by the fact that the particles which would be lost due to phase and voltage errors would be lost preferably as well due to the quadrupoles misalignment. The transmission rate is more than 93 % if the misalignment is kept less than 0.1 mm and then drops exponentially with higher misalignments. Also in this case the major losses occur in the diagnostics section.

From these results we can conclude that the Proton Injector design is very robust against possible random errors due to fabrication and installation mistakes and against random fluctuations from the power supplies. The analysis of the transmission profiles points out how the critical region is the long drift section needed for diagnostics. For this reason the design of this section shoud be carefully investigated: a possible solution could be the use of a focusing triplet just behing the third coupled module of the proton injector. In this way the transversal dimension of the beam can be kept narrower

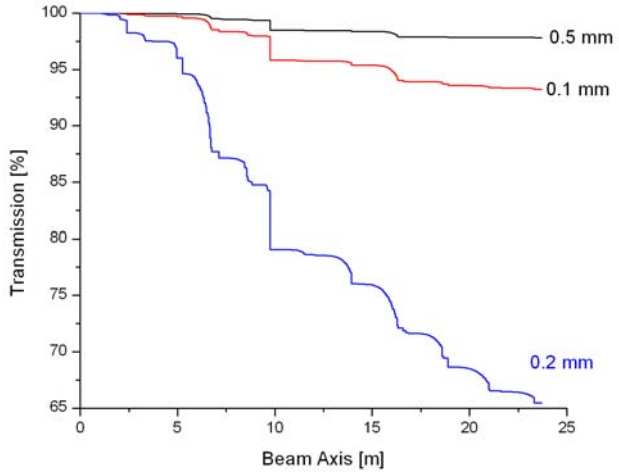

Figure 3.33: The beam transmission all error.

reducing considerably the probability of particles losses.

3.6 RF Parameters of the Proton Injector

The main feature of the new Proton Injector of FAIR is its high efficiency when compared to other convential RF structures. Fig.3.34 show the expected effective shunt impedance of the FAIR proton injector together with the one of existing IH cavities, and compares those value with the RF efficiency of conventional structure like the $\beta\lambda$ DTL, and the $\beta\lambda/2$ CCL. From this picture it emerges clearly how, in the range from 3 to 70 MeV the CH is the best performing structure in terms of RF consumption . This justifies the choice to base the entire proton injector on this structure and to avoid any jump in RF frequency as foreseen for many other projects. [cfr. Section 1.3]

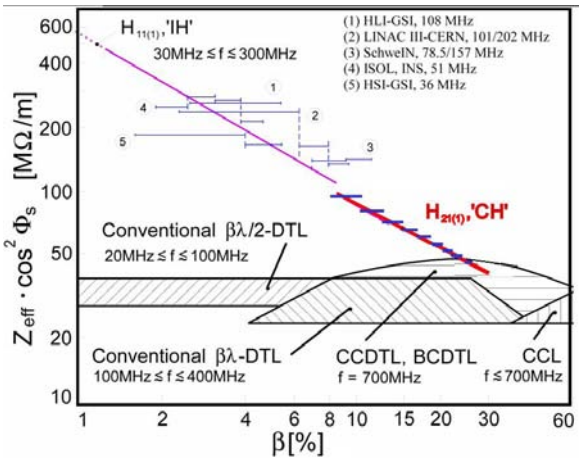

Figure 3.34: The shunt impedance of H-mode DTL's when compared with conventional RF structure.

The CH-DTL part of proton injector will consist of twelve tanks grouped in six pairs

of coupled modules each powered by a single klystron: the maximum power consumption, including the beam loading, should be kept below2.2 MW in order to have a safety margin with respect to stable operation. The proposed klystron can infact deliver up to a maximum power of 2.5 MW under long terms stable conditions. The RF-pulse to be provided by the power sources for each pair of cavities is shown in Fig. 3.35: during the beam pulse the total forward RF-power will be 2.2 MW at maximum with about half of this value to power the unloaded cavities. A survey on the market with respect to available power sources indicated that the adoption of the Toshiba klystron 3740A would minimize the respective investment cost: this 324 MHz, 2.5 MW klystron was developed for the JPARC linac and can be easily update to operate at 325 MHz with a repetiotion rate of 4 Hz. The resulting duty cycle is then 0.028 %.

Seven klystrons will be used in total, six to power the DTL cavities and one for the RFQ. The two bunchers RF-power needs are expected to be below 50 kW and solutions based on conventional tubes or solide state amplifiers are foreseen. However, klystron manufacturers were contacted as well in order to receive alternative proposals.

It is important to note that the avaibility of this kind of power supply, reliable, efficient and relatively cheap, has been one of the major reasons to switch the operating frequency from 352 to 325 MHz.

The RF-power sources together with their power converters represents a considerable part of the overall project budget. In order to obtain an optimized concept, several scenario of the RF power alimentation for the given number of RF cavities were analyzed with respect to the investment cost. The chosen solution consists in a single power converter driving one klystron which feeds a coupled CH cavity as shown in Fig.3.36. The power converters for pulsed klystrons at 325 MHz need special efforts for the design, specification, and production. Converters for cw-klystrons were operated at LEP. However, for a pulsed machine at this frequency converters are not available yet. For the FAIR proton linac the development aims for devices that can be operated without crow bars in order to be efficient in cost and spacing.

The power converter has to deliver the klystron electron beam current pulse of 45 A with a cathode-to-ground voltage of 110 kV. It delivers pulses of 80 μs at 4 Hz. Assuming an electron current of 45 A, a total charge of about 3.6 mC is required per RF-pulse. This charge is stored in a capacitor of 1 μF such that the total amount of energy that might be released in case of a voltage break down (arc voltage of 100 V) will not exceed 11 J (100 V $\cdot$ 110 kV $\cdot$ 1 μF), which is not critical for the klystron. The main part of the energy released in case of a break down, i.e. the equivalent to the total charge in the 1 μF capacitor, will be dissipated in a resistor of about 30 Ω being in series with the klystron cathode. In the time between the pulses the capacitor is re-charged by a 110 kV / 20 mA high voltage source.

A second converter provides the voltage of the modulation anode to control the electron beam current. Additionally, a cathode heater power converter as well as converters for the solenoid circuits is required.

The heat losses can be derived by the effective shunt impedance by the following relation

$$P = \frac{(\Delta W)^2}{Z_{eff} \cdot \cos^2(\bar{\phi}) \cdot l} \tag{3.15}$$

where ΔW is the energy gain, l the length of the cavity and the term $\cos^2(\bar{\phi})$ takes into account the different synchronous phases of the accelerating gaps.

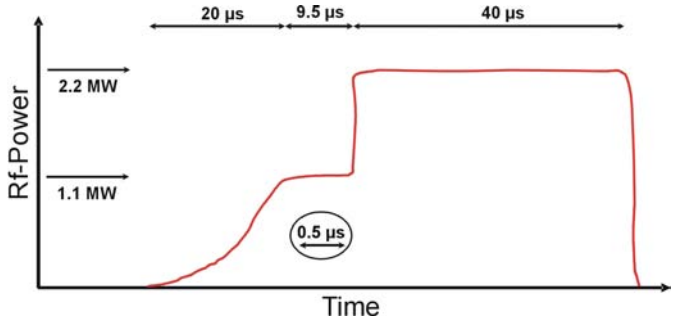

Figure 3.35: Shape of the RF-pulse to be provided by the RF-power sources for the accelerating cavities of the proton linac. The RF-power is initially switched on and regulated to the unloaded cavity level. The input power is increased within less then one microsecond after the beam entered into a pair of two RF-coupled cavities.

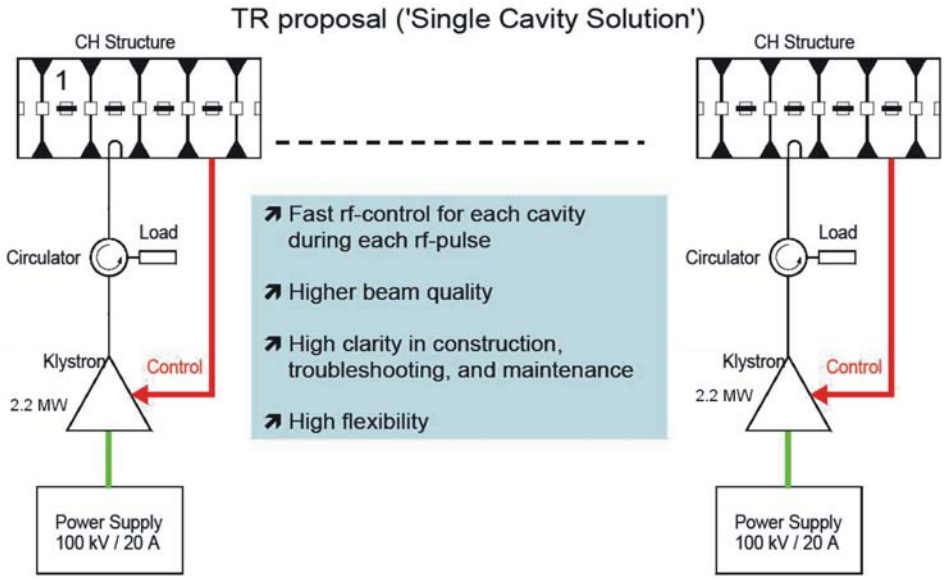

Figure 3.36: The RF system proposed for the proton injector: a single klystron driven by a single power converter feeds a coupled CH-DTL.

As one can see from Tab.3.13 the ohmic losses are kept quite low in the first two tanks which, for beam dynamics constraints, must be quite short, and then are stabilized around 400 kW along the whole structure. The maximum power consumption, ~ 2 MW, is assumed to be in the second coupled module, tank 3 and 4, where beam dynamics allows longer tanks and the shunt impedance in the corresponding energy range is still adeguate to push towards a more ambitious design. On the other side, the higher shunt impedance at the low energy side characterises the fist module in terms of high acceleration gradient as shown in fig.3.36. It is also important to observe the choice to divide almost equally the power consumption between the beam loading and the ohmic losses: in this way the risk of strong interection between the beam and the cavity is reduced increasing the stability of the machine during the operation.

The lenght of the cavityes goes to half a meter of the first one up to 2.1 meters in the high energy section; corresponding, the radius of each tank encreas from 160 mm

Tank	ΔW [MeV]	Length [m]	P_{heat} [MW]	P_{beam} [MW]	P_{tot} [MW]	ZT^2 MΩ/m
1	3.094	0.4	0.262	0.216	0.478	95
2	5.597	0.68	0.59	0.391	0.941	75
3	5.579	0.96	0.51	0.403	0.913	68
4	6.84	1.24	0.65	0.471	1.121	60
5	5.95	1.52	0.43	0.416	0.846	55
6	6.18	1.68	0.45	0.432	0.882	52
7	5.93	1.82	0.40	0.414	0.814	50
8	5.90	1.94	0.41	0.419	0.829	48
9	6.16	2.06	0.42	0.432	0.852	45
10	5.89	2.02	0.40	0.412	0.812	43
11	5.93	2.11	0.40	0.415	0.815	42
12	5.60	2.03	0.40	0.397	0.797	40

Table 3.13: Parameters of the 325 MHz RF-cavities of the proton linac, mechanical length, average effective shunt impedance, energy gain, peak beam power at 70 mA, peak heat loss power and total peak power, average effective shunt impedance.

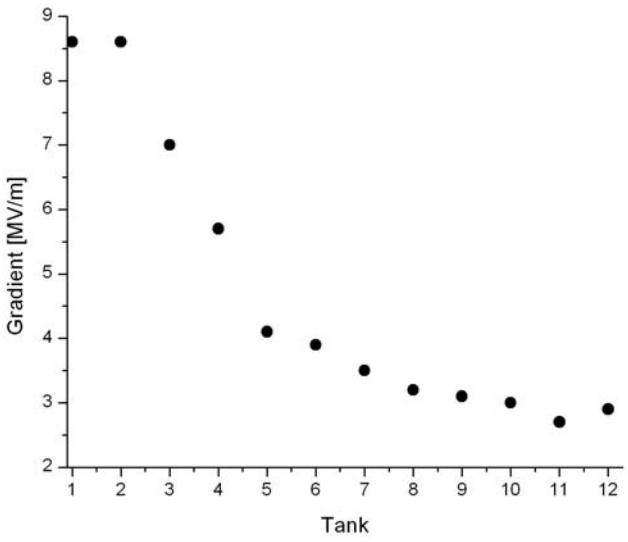

Figure 3.37: The accelerating gradient of the Proton Injector.

up to 220 mm: in this way the dimension and weigth of each cavity are compatible with manuteance requirements and building constraints

Finally, the maximum electric field distribution all along the linac is shown in Fig.3.39: as one can see, the field is rather constant inside each coupled structure-ans decreases from the level of 17 MV/m of the first two sections down to 6 MV/m in the last coupled module.

According to the large experience with high gradient in existing H-type linac these

value are safe enough against discharge phenomena

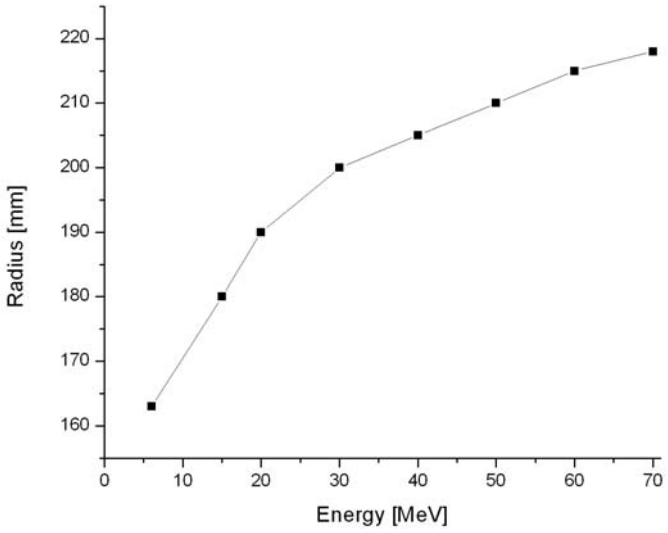

Figure 3.38: The expected radius of the CH-DTL according to the energy.

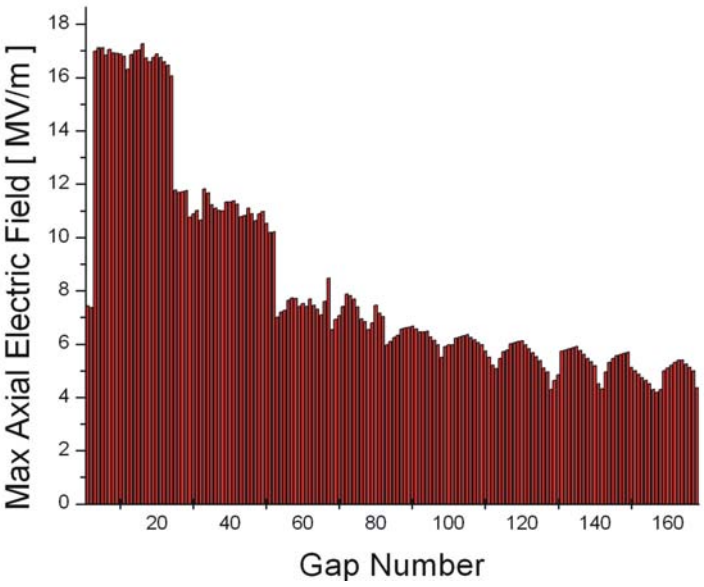

Figure 3.39: The maximum on axis electric field all along the proton injector as computed by LORASR.

Acknowledgments

First of all I want to thank my father and my mother for the efforts they did in their life to educate me and my brother.

My truly gratitude goes to Uli Ratzinger, who represents for me much more than a thesis supervisor. His encourgments, politness, the joy and enthusiasm he puts in his everyday job have represented for me the strongest motivation in doing this work.

I'm extremely thankful to all the people and friends who worked with me during this great period, I would really like to thank all of them, especially Martin, for his endless patience, Holger for the nice discussions and for his sky lessons in Austria, Oliver for his kindness, Daniel for his help in the workshop and Rudolf for his deep effots in the development of the Lorasr Code.

I want to thank the secretary of IAP, Mrs. Harji for her kind help in solving every burocratic problem I encounterd arriving in Germany.

A particular acknowledge goes to Dr. S. Minaev, who has given me extremely important suggestions and advices during his gast visits at the Frankfurt University.

I appreciated as well the help I received from my collegues of GSI, in particular from my friends Lars Groening, Andrea Franchi, Giancarlo Maero and Martino Trassinelli.

My truliest gratitude goes to Barbara: without her love, help and support this thesis would not exist...

Thanks is only a short world, but sometimes its meaning its enourmous: to all of you guys, I can just say Thanks!

Finally, I acknowledge the support of the European Community-Research Infrastructure Activity (CARE, contract number RII3-CT-2003-506395) which has partially funded my research activities.

Curriculum Vitae of the Author

Family name:	Clemente
Name:	Gianluigi
Marital Status:	Single
Nationality:	Italian
Place of birth:	Benevento (Italy)
Date of birth:	7 / 7 / 1977

Education

- March 2003: Master degree (Laurea) in physics, University of Pavia: thesis on environmental pollution of Radon gas at the Gran Sasso Laboratory. Co-supervisors Profs. M.Fraternaly (University of Pavia) and Dr. G. Cecchet (INFN). Grade:107/110
- March 2004 Internation Master (Graduate School) on ' Nuclear Technologies and Application of Ion Beams', Universitary Institute Of Higher Studies, Pavia. Title of the Thesis:' Development of a self-shielded 10 MeV cyclotron. Supervisor Dr. F. Stichelbaut (IBA, Belgium).
- July 1996: High school (Scientific Lyceum) in Cologno Monzere (Milano): Grade 44/60 .

Present Professional Status

- Institute: IAP, J.W. Goethe University, Frankfurt am Main.
- Address: Max von-Laue str. 1 -60438, Frankfurt am Main, Germany
- Telephon: +49 69 798 47454
- E-mail: clemente@iap.uni-frankfurt.de
- Position: wissenschaftliche Mitarbeiter

Professional Experience

- Place: IAP, Frankfurt, Germany.

  period: from March 1 2004

  Subjects: PhD thesis on the development of high efficient proton linear accelerators;

- Place: Louvain La Neuve, Belgium.

  period: August 2003 February 2004

  Subjects: Development of a self-shielded cycltron.

- Place: LNGS-INFN, Assergy (L' Aquila), Italy.

  period: Technical student from March 2002 to March 2004

  Subjects: Collaborator of the BOREXINO experiment.

Awards

- 2005: Student Travel Awards of the 2005 PAC Conference, Knoxville, TN, USA.

Languages

- Italian: mother language
- French: fluent
- English: fluent
- German : mittlestufe

Computing

- Windows and Linus as operating systems
- Programming languages: fortran (advanced), C (basic)
- Experience in running numerical code for particle tracking and RF Structure simulation, LORASR, Microwave Studio.

Publications

- 'Development of a Coupled CH Structure for the GSI Proton Injector', *Proceedings of the PAC 2007, Albuquerque, NM, USA.*
- 'Development of a Room Temperature CH-DTL', G. Clemente, H. Podlech, U. Ratzinger, R. Tiede *Proceedings of the EPAC 2006, Edinburgh, UK.*
- 'Commissioning of the 7-MeV/u, 217-MHz Injector Linac for the Heavy Ion Cancer Therapy Facility at Heidelberg' B. Schlitt, R. Baer, W. Barth, T. Fleck, M. Hoerr, G. Hutter, C. Kleffner, M. Maier, A. Peters, M. Schwickert, K. Tinschert, W. Vinzenz, H. Vormann, D. Wilms, G. Clemente, Y. Lu, S. Minaev, U. Ratzinger, A. Schempp. *Proceedings of the EPAC 2006, Edinburgh, UK.*
- 'A 70-MEV PROTON LINAC FOR THE FAIR FACILITY BASED ON CH CAVITIES', U. Ratzinger, G. Clemente, C. Commenda, H. Liebermann, H. Podlech, R. Tiede, *Proceedings of the LINAC2006, Knoxville, TN, USA.*

- 'The 70-MeV Proton Linac for the Facility for Antiproton and Ion Research FAIR', L. Groening, W. Barth, L. Dahl, W. Vinzenz, S. Yaramyshev, G. Clemente, U. Ratzinger, A. Schempp, R Tiede, *Proceedings of the LINAC2006, Knoxville, TN, USA.*

- 'LORASR Code Development', R. Tiede, G.Clemente, H.Podlech, U.Ratzinger, Z.Li, *Prooceedings of the EPAC 04 Conference, Luebeck, Germany.*

- 'Development of Normal Conducting CH-DTL' G. Clemente, H. Podlech, U. Ratzinger, R. Tiede, *Proceedings of the PAC2005, Knoxville, TN, USA.*

- 'KONUS Beam Dynamics Design of a 70 mA, 70 MeV Proton CH-DTL for GSI-SIS12' R. Tiede, G. Clemente, H. Podlech, U. Ratzinger, W. Barth, L. Groening, Z. Li, S. Minaev, *Prooceed of the EPAC 04 Conference, Luebeck, Germany.*

- 'Design of the R.T. CH-Cavity and Perspectives for a New GSI Proton Linac'. Zhihui Li, R. Tiede, U. Ratzinger, H. Podlech, G.Clemente, K.Dermati, W. Barth, L. Groening, *Prooceed of the EPAC 04 Conference, Luebeck, Germany.*

- 'The 70 MeV p-Injector Design for Fair', U. Ratzinger, H. Podlech,, R. Tiede, B. Hoffmann, G. Clemente, A. Schempp, *Proceedings of the ICFA-HB04, Bensheim, Germany, 2004.*

- 'Linac Code Benchmarking for the UNILAC Experiment', A. Franchi, W. Bayer, G. Franchetti, L. Groening, I. Hofmann, A. Orzhekhovskaya, S. Yaramyshev, X. Yin, A. Sauer, R. Tiede, G. Clemente, R. Duperrier, D. Uriot, G. Bellodi, F. Gerigk, A. Lombardi, *Proceedings of the LINAC2006, Knoxville, TN, USA.*

- 'Development, Construction and Testing of a room temperature CH-DTL', G.Clemente, H. Podlech, U. Ratzinger, R. Tiede, S.Minaev, *CARE Note 2007-001-HIPPI.*

- 'Beam Dynamics of the first tank of the GSI Proton Injector', G.Clemente, H. Podlech, U. Ratzinger, R. Tiede, S.Minaev, *CARE Note 2006-015-HIPPI.*

Bibliography

[1] G.Gamow, Zeit f. Phys. 51, 204 (1928)

[2] J.D. Cockcroft and E.T.S. Walton, ' Experiments with high velocity ions', Procced. of Royal Society, Series A 136, 1932, 619-20.

[3] R.J. Van der Graff, ' A 1.5 MV electrostatic generator', Phys. Rev., 387, 1931, 1919-20.

[4] G. Ising, Arkiv fr Matematik, Astronomi och Fysik, 18 (1924), 1-4.

[5] R. Wideroee, Arch.fr Elektrotechnik, 21 (1928), 387-406 .

[6] E.O. Lawrence and N.E. Edlefsen, Science, 72, 1930, 376-7.

[7] E.M. McMillan, 'The synchrotron - a proposed high-energy particle accelerator', Phys. Rev., Letter to the editor, 68 (Sept. 1945), 1434.

[8] V. Veksler, J. of Phys, USSR, 9 (1945), 153-8.

[9] G.S. James, R.H. Levy, H.A. Bethe and B.T. Fields, 'On a new type of accelerator for heavy ions', Phys. Rev., 145, 925 (1966).

[10] F.K. Goward and D.E. Barnes, Nature, 158 (1946), 413.

[11] S. van der Meer, 'Stochastic damping of betatron oscillations in the ISR', CERN/ISRPO/ 31-72 (August, 1972).

[12] L.W.Alvarez, Phys.Rew 70, 799 (1946).

[13] L.W.Alvrez et Al, Rew.Sci.Instr. 26, 111 (1955).

[14] I.M. Kapachinsky and V.A. Tepliakov, Prib. Tekh. Eksp, 4, 17,19 (1970).

[15] M.L. Good, Phys. Rev. 92, 538 (1953).

[16] W. Henning et Al.,'An International Accelerator Facility for Beams of Ions and Antiprotons', GSI Darmstadt, 2001, www.gsi.de/GSI-Future/cdr/.

[17] National Spallation Neutron Source Conceptual Design Report, Oak Ridge National Laboratory, NSNS/CDR-2/VI (1997)

[18] R.Garoby et Al, 'LINAC4, a new injector for the CERN PS Booster', Proceed. of the 2006 EPAC Conference, Edimburgh, UK.

[19] Ravn, Helge L. et Al, 'Advanced target concepts for production of radioactive ions and neutrino beams', Nucl. Instrum. Methods Phys. Res., B 204 suppl. (2003) 197-204.

[20] P.N. Ostrumov et Al, 'Front End Design of a Multi-GeV H-Minus Linac', Prooc. of the PAC 95 Conference, Knoxville, TN, USA.

[21] F. Naito, 'Thr JAERI/KEK joint project and its Performance', Proceedings of LINAC2002, Gyeongju, Korea, 564-568.

[22] C.Plostinar, M.Clarke-Goyther 'Rebunching cavities for the RAL front-end test (FETS)',Proceed. of the 2006 EPAC Conference, Edimburgh, UK, 306-308.

[23] J. Broere et Al, proc. Of the LINAC 98 Conference, Chicago, USA, pp. 771-773

[24] E.Nolte et al., Nucl. Instr. and Meth., vol. 158, p. 311.

[25] U.Ratzinger, 'High Current IH Structure', Proc. Of the EPAC 1994 Conference, London, vol.1,P.264

[26] U. Ratzinger, RNB-specific linac development, Nuclear Physics A 701 (2002) 641c/646c

[27] H.D. Haseroth, in: Proc. LILNAC 96, Geneva, CERN 96-07, p. 283.

[28] O. Kester, et al, STATUS OF THE REX-ISOLDE LINAC, Proc. Of LINAC98, Japan, 812-814

[29] H.Eickoff et Al, 'The Proposed Dedicated Ion Beam Facility for Cancer Therapy at the Clinic in Heidelberg', Prooc.of the 1998 EPAC Conference, Stockolm, Sweden

[30] www.cnao.it

[31] A.Schempp and U.Ratzinger, 'RFQ and IH Accelerators for the new EBIS Injector at BNL', Prooc. of the PAC07 Conference, ALbuquerque, NM, USA.

[32] L.P Chao et Al, 'The Frankfurt Neutron Source at the Stern-Gerlach-Zentrum (FRANZ)' Prooc. of the EPAC06 Conference, Edimburg, UK.

[33] T. E. Shannon et Al, 'IFMIF International Fusion Materials Irradiation Facility: A High Intensity Deuteron Beam' Prooc.of the 1998 EPAC Conference, Stockolm, Sweden

[34] www.fzk.de/eurotrans/

[35] 'Linear accelerator injection for proton synchrotrons', Proc. CERN Symposium in high energy accelerators and pions physics, Geneva, 1956.

[36] V.A.Bomko, E.I.Revutskii, Soviet Physics Techn. Physics, vol. 9, no. 7(1965), p. 973.

[37] U. Ratzinger and R. Tiede, 'Status of the HIIF RF Linac Study Based on H-Mode Cavities', NIM A 415, (1998).

[38] G.Clemente et Al, 'The tuning of the HIT-IH', 2007 GSI Internal Report.

[39] U.Amaldi et Al 'CLUSTER: a high frequency H-mode coupled cavity linac for low and medium energies', for submission to Nucl. Instr. Meth. A

[40] H.Podlech et Al, 'The Superconducting Linac Approach for IFMIF', Prooc. of the PAC07 Conference, ALbuquerque, NM, USA.

[41] C. Zhang et Al, 'Conceptual Studies of the EUROTRANS Front-End', Prooc. of the PAC07 Conference, ALbuquerque, NM, USA.

[42] G.Clemente, et Al 'Development, Construction and Testing of a room temperature CH-DTL', CARE Note 2007-001-HIPPI.

[43] CH Techncal Design Report, 2004.

[44] 'RF Linear Accelerator', Wiley Interscience Edition, 1998

[45] U.Ratzinger , 'A low Beta RF Linac Structure of the IH-Type with improved Radial Acceptance' Prooc. of the 1988 Linac Conference, Newport, USA, pp 185/187

[46] H. Podlech et Al 'Superconducting CH structure' Physical Review S.T. - Accelerators and beams 10, 080101 (2007).

[47] H. Podlech, H. Liebermann, A. Sauer, U. Ratzinger, 'Development of Superconducting CH-Structures for Low and Medium Beta Beams'. Proceed. of the ICFA-HB04, Bensheim, Germany, September 18-22 2004

[48] L.Groening 'Beam current and emittances of the front-end of the GSI proton linac and other facilities'. UNILAC-Arbeitsnotiz 22.09.2003

[49] 'An International Facility for Beams of Ions and Antiprotons', Conceptual Design Report, GSI, 2001

[50] L.J Rybarcyk et Al. 'LEDA Beam Operations Milestone and Observed Beam Transmission Characteristics'. Proceed of the 2000 LINAC Conference, Stanford, USA.

[51] A. Schempp, B. Hofmann, L. Brendel, *CDR for a 352 MHz Proton RFQ for the new GSI Proton Linac* Int. Rep. S-05-4, Frankfurt University, (2005).

[52] U.Ratzinger et Al 'A 70-MeV Proton Linac based on CH-Cavities'. Proceed. of the 2006 LINAC Conference, Knoxille, USA.

[53] U.Ratzinger and R.Tiede, ' Teilchendynamische Untersuchungen an einer Kombinierte Null Grad Strukture KONUS mit Quadrupoltriplett-Fokussierung', GSI-ALG 10077 SI.

[54] R. Tiede, G. Clemente, H. Podlech, U. Ratzinger, A.Sauer, S. Minaev, 'LORASR Code Development', Proc. of the 2006 EPAC, Edinburgh, pp 2194-2196.

[55] J. Cooley and J. Tukey, 'An Algorithm for the Machine Calculation of Complex Fourier Series', Math. Comput. 19 (1965), pp 297-301.

[56] CERN Internal Report 93/01.

[57] A.Franchi et Al, 'Linac Code Benchmarking in Preparation of the UNILAC experiment',CARE Note 2006-011-HIPPI.

[58] J. Qiang et al., 'An Object Oriented Parallel Particle-In-Cell Code for Beam Dynamics Simulation in Linear Accelerator', Journal of Computational Physics, 163, pp 434-45, 2000.

[59] A. Franchi et Al, 'HALODYN: a 3D Poisson-Vlasov Code to Simulate the Space Charge Effects in the High Iintensity Ttasco Linac', Prooced. of the 2002 Linac Conference, Seul, South Korea.

[60] S. Yaramishev et al. 'Development of the versatile multi-particle code DYNAMION' , NIM A, Vol 558/1 pp 90-94 (2005).

[61] R. Duperrier et Al, 'TOUTATIS, THE CEA-SACLAY RFQ CODE' Prooced. of the XX Linac Conference, Monterey, Ca, USA

[62] D. A. Swenson, and J. E. Stovall, 'PARMILA'", Los Alamos National Laboratory Internal Memorandum, MP-3-19, January 1968.

[63] http://tmuetze.home.cern.ch/tmuetze/

[64] N. Pichoff, D. Uriot, "PARTRAN," Internal Memorandum, CEA, Saclay.

[65] K.R.Krandall, R.Wagner 'PARMTEQ-a beam-dynamics code fo the RFQ linear accelerator',Proceed. of the AIP Conference,, 1988, Vol. 177, Issue 1, pp. 22-28.

[66] R. Tiede, PhD Dissertation, J.W.Goethe University, Frankfurt am Main, to be published.

[67] U.Ratzinger 'Habilitationsschrift', 1998, Frankfurt am Main, Germany.

[68] G.Clemente et Al., ", Proc. Of the PAC 2005 Conference, Knoxville, TN, USA.

[69] U.Ratzinger, 'H-Type Linac structures, CAS (2000), Seeiheim, Germany

[70] U. Ratzinger 'H-Mode Linacs', CERN Accelerator School, May, 2000, Lufthansa Training Center, Germany.

[71] T.Wangler, 'RF Linear Accelerator', ed. Wiley Interscience, 1998

[72] P. Forck et Al, 'Beam Diagnostics for the upgraded UNILAC at GSI', Proode. of the EPAC98, Stockolm, Sweden, 1500-1502.

List of Figures